University of Alberta

Instrumentation for Interstitial Photodynamic Therapy of Prostatic Carcinoma

by

Weiyang Liu

A thesis submitted to the Faculty of Graduate Studies and Research
in partial fulfillment of the requirement for the degree of

Master of Science
in
Photonics and Plasmas

Department of Electrical and Computer Engineering

Spring 2010
Edmonton, Alberta

Examining Committee

Dr. John Tulip, Electrical and Computer Engineering

Dr. Ronald B. Moore, Surgery

Dr. Ying Tsui, Electrical and Computer Engineering

Abstract

This thesis encompasses the development and testing of an interstitial photodynamic therapy (iPDT) system for the treatment of prostate cancer. It begins with the optical characterization of a novel photosensitizer (SL-052) followed by a study of tissue optics as it applies to iPDT. The design and integration of a time-fractionated light delivery system with real-time spectral detection is then examined. An optical phantom test medium is formulated and *in vitro* system operation and testing is performed. Finally, *in vivo* experiments are performed on animal models with a focus on canine prostate iPDT. Unique optical results with dosimetric relevance are discovered and investigated. This includes metrics for optically measuring local *in vivo* SL-052 concentrations in real-time as well as novel oscillatory drug photobleaching and recovery behavior during time-fractionated light delivery.

Contents

List of Tables

List of Figures

Chapter 1

Introduction

The purpose of this study is to design, construct, and test an interstitial photodynamic therapy system for the treatment of prostate cancer. The system should be able to accommodate the use of various photosensitizers with minor adjustments, but is customized to take advantage of unique photophysical properties of our primary test drug: SL-052. The scope of this study encompasses optical characterization of SL-052, tissue optics as it applies to iPDT, construction of light delivery and detection system, and system operation and testing including iPDT of canine prostate.

1.1 Prostate Cancer and Prostate Anatomy

Prostatic carcinoma is the most commonly diagnosed noncutaneous malignancy for men in North America with mortality second only to lung cancer and an estimated 192,280 newly diagnosed cases for 2009 in the United States alone[1, 2]. With increasing awareness and the introduction of prostate specific antigen (PSA) testing, the disease is being frequently diagnosed at earlier

stages (stage migration) when the malignancy is still confined to the prostatic capsule and procedures can be applied with curative intent. Currently, only 1 in 7 will die from the disease[1]. However, current treatment modalities are often associated with significant complications such as urinary incontinence, impotence and collateral tissue damage, causing great inconvenience and degradation to the quality of life for patients, even if complete cure to the cancer is attained. As such, the aim for alternative treatments is not only to prolong patient life span, but also to improve the post treatment patient quality of life.

Anatomically, the prostate is a walnut-shaped gland which surrounds the urethra just below the urinary bladder, anterior to the rectum, and in close proximity to the urinary sphincter. A pair of neurovascular bundles containing cavernous nerves, which control erectile function, run along the prostate. Due to this anatomy, cancer of the prostate put at risk urinary, sexual and bowel function[3]. The key to improving treatment outcome is to accomplish complete removal of cancerous tissue while minimizing damage to these critical surrounding structures.

1.2 Current Treatments for Prostate Cancer

Prostatectomy, radiotherapy (external beam or brachytherapy), hormone therapy, and chemotherapy are the four most common modes of treatment available for the management of the disease[1]. Prostatectomy involves surgically removing the prostate, usually in its entirety and frequently requiring expansive resectioning of the region to ensure a negative surgical margin. This

[1]Here, I am not considering treatments without curative intent such as transurethral resection of the prostate (TURP) which reduces symptoms but not intended to control the cancer itself.

often affects surrounding tissues and results in sacrifice of cavernous nerves. When possible, nerve-sparing surgery will be performed to limit damage to the cavernous nerves; however, even with preservation of both neurovascular bundles, potency rates have been found to be significantly reduced[4]. In external beam radiotherapy, radiation is applied externally and aimed to concentrate on the prostate. Both healthy and cancerous cells along the beam path will be damaged. In brachytherapy, small radioactive sources are inserted inside the prostate, but again, along with cancerous cells, healthy cells in this critical region are also damaged. Hormone therapy involves lowering or blocking certain hormones, primarily testosterone, to slow the growth of the tumor or even shrink it. The therapy causes various side effects in men related to reduced testosterone levels such as impotence, loss of sexual desire, breast tenderness and hot flashes. Chemotherapy is an anti-cancer treatment common for many types of cancers. Drugs are used to constrain cancerous growth but will also affect healthy cells.

Although current treatment modalities of prostate cancer are effective in prolonging the life of patients, they lack the specificity to combat cancer with minimal collateral damage. Rados[5] showed that "about 15 percent to 50 percent of men treated for prostate cancer by surgery, radiation therapy, or hormonal therapy will have urinary incontinence and sexual impotence, and in extremely rare cases, scarring of the intestine." Because the prostate is in close proximity to so many physiologically important structures, these treatments often cause significant complications. In addition to the stage migration there has been an age migration, with the disease being discovered at younger ages, making these mutilating therapies less desirable. The disease is slow progressing and non-life threatening in a significant portion of early diagnosed patients, making less invasive alternatives highly desirable. The purpose of

this thesis it to present research on instrumentation and implementation of an alternative treatment for prostate cancer.

1.2.1 Alternative Treatments for Prostate Cancer

Current alternatives to the four modes of treatment include cryotheraphy and thermal therapy. Cryotherapy[6] involves locally cooling the target tissue to cause disruption of cellular membranes with delayed vascular occlusion. This is typically achieved using cryoprobes often administered via the perineum under transrectal ultrasound guidance. There are several forms of thermal therapy that exploits coagulation necrosis at temperatures greater than 55-60 ^{o}C. One type is high intensity focused ultrasound (HIFU)[7] which heats tissue from absorption of highly focused ultrasound energy. Microwave thermal therapy[8] is similar to HIFU except that heating is achieved via microwave emitting antennas administered into the prostate. Although these procedures have demonstrated a reduction in PSA, they lack a high degree of specificity and are also associated with the same complications as standard modalities[9, 10, 11].

1.3 Diagnosis Ahead of Treatment

The circumstance surrounding the treatment of early stage prostate cancer is one of mixed views. While the current capability to diagnostic prostate cancer at early stages from PSA testing is a diagnosis milestone for the disease, the time gained from this early detection does not significantly benefit the patient. The disease can now be caught at such an early stage such that it is unknown if each particular case of the disease will ever become life threatening

or even show bothersome symptoms[9], and thus prompting studies in active surveillance or deferred treatment. "Many affected men might not experience adverse impact to survival or quality of life were treatment deferred"[12]. PSA can correctly identify if the prostate is in distress and biopsies can positively identify the presence of neoplastic tissue, but there is a lack of a metric for determining if immediate treatments are necessary. While current treatments to the early disease yield excellent long-term survivability, and has been shown to reduce prostate cancer metastasis and cause-specific mortality[12], the therapies are so mutilating that the treatment induced loss in quality of life could be more than what the disease compromises. Therefore, watchful waiting is often prescribed, and to only initiate treatment when the disease advances to stages with higher threat to patient life. However, the lack of means to correctly identify candidates for delayed therapy without implicating chances of cure results in apprehension against watchful waiting and a large percentage of men being over treated[13].

In a 10 year study comparing radical prostatectomy with watchful waiting in early stage prostate cancer, Bill-Axelson[14] concludes that the advantage in reduction in the risk of death from undergoing treatment versus simply watchful waiting is small. Vicini[15] reviewed PSA stratified early stage prostate cancer treatment and found that "no consistently superior treatment option in the radiotherapy or surgical literature emerged." He also advises that "despite significant advances in the diagnosis, staging and treatment of localized prostate cancer, the optimal management of this disease remains undefined." More research is needed to determine the best option of therapy because no procedure stands out as the best treatment for slow growing, low grade prostate cancer, leaving watchful waiting as a frequently prescribed disease management protocol and nullifying the advantage of early detection.

Thus, we are in a situation where diagnostic technologies and practices allow for early detection of prostatic carcinoma, but the procedure for appropriate interventional treatment of the early stage disease is not available. An alternative modality for locally confined prostate cancer is needed that can provide excellent long-term survivability while maintaining high specificity and therapeutic ratio resulting in milder side effects.

1.4 Photodynamic Therapy

Dougherty[16] and Moan[17] have written excellent reviews of the field of PDT. A brief overview will be given here. Photodynamic therapy (PDT) is an evolving, minimally invasive, two-step experimental modality that has shown promising results in various oncological and non-oncological applications including: cancers of the prostate, bladder, lung, digestive tract, skin, head and neck, as well as age related macular degeneration, cardiovascular disease, psoriasis, rheumatoid arthritis, menorrhagia and benign prostatic hyperplasia. The therapy involves the administration of a photosensitive agent followed by subsequent local illumination of light to locally excite the photosensitizer in target tissue. In the presence of oxygen, the excited photosensitizer undergoes photochemical reactions generating singlet oxygen and other reactive oxygen species or radicals which cause therapeutic effect by direct cellular destruction, vasculature stasis, or other pathways.

PDT does not incur the cumulative dose toxicity associated with radiotherapy allowing patients to be subject to repeat treatments, as well as treatments following radiotherapy[18]. The first official approval of PDT came on April 19, 1993 as the Canadian Health Protection Branch approved Photofrin for PDT

of recurrent superficial papillary bladder cancer. The following decade and a half has been regarded as the Golden Age of PDT as various different drugs have approved for PDT around the world in several developed nations[17]. PDT offers potentially higher specificity and less side effects compared to other treatments in that other focal therapies only offer one level of cancer targeting agent. Similar to Chemotherapy, PDT has a chemical agent with a higher affinity for neoplastic tissue in the form of a photosensitizer, and in common with radiotherapy, PDT has a guided electromagnetic radiation component targeting the treatment region. However, the difference is that in PDT, the two components alone are non-toxic and non-destructive. In the presence of oxygen, photodynamic action will only occur at the intersection of these two components. Therefore, PDT possess a two-level targeting scheme offering the possibility of much higher specificity than other treatments.

1.4.1 Photodynamic Therapy of the Prostate

Studies of PDT of the prostate began in the 1980's with our research group being one of the early pioneers to propose the idea[19, 20]. Due to the anatomical location of the prostate gland, PDT must be performed interstitially for sufficient illumination of the entire gland. For minimal invasiveness, light delivery is commonly achieved by narrow fiber optic insertion into the prostate. Interstitial PDT (iPDT) of prostatic carcinoma is feasible because the prostate gland has favorable optical properties for iPDT[21] and is an easily accessible organ for interstitial fiber placement via the perineum based on well established brachytherapy techniques. As well, Chen[22] reported similar optical properties between normal and carcinoma tissue in the human prostate, making the prostate an ideal candidate for iPDT. Various photosensitizers with

different light delivery techniques have shown encouraging *in vivo* results, including clinical trials with meso-tetrahydroxyphenyl chlorin (FOSCAN)[23], ALA induced PpIX[24], Motexafin Lutetium[25] and Pd-Bacteriopheophorbide (TOOKAD)[26]. As such, PDT is emerging as a promising alternative treatment for prostate cancer that warrants further research and innovation.

1.5 Thesis Overview

This thesis is split into three sections and encapsulates the formulation and testing of our novel iPDT system including *in vivo* and *in vitro* experimentation. The first section primarily discusses the photophysical properties of the photosensitizer SL-052 and how that applies to PDT and dosimetric considerations. The second section describes in detail the hardware and software design and integration of the iPDT system. The third involves *in vivo* experimentation using the novel iPDT system with special attention to spectral characteristics and unique spectral changes during PDT as it applies to dosimetry.

Chapter 2

Photosensitizer and Tissue Optics

2.1 Background and History

Evidence shows that the concept of photosensitization have been known for over a century[17, 27, 28] but the photochemical interactions were not well understood until more recently. First, a basic description of the photochemical interaction is discussed, followed by a brief history of a relatively recent development of a first-generation photosensitizer that accelerated the growth in this field. Then a discussion will be made regarding the desired characteristics for future second-generation drugs, and finally, information regarding hemoglobin transmissivity and other tissue optics will be presented and its significance to photosensitizer dosimetry will be discussed.

2.1.1 Photochemical Interaction

In general, a compound classified as a useful photosensitizer for PDT differs from other organic dyes in that the time frame in which the photo-

sensitizer stays in the electronic excited state following an absorption event is significantly longer (μs) than ordinary dyes[28]. Where as excited non-photosensitizing agents decay rapidly and dissipate their energy internally, the longer lifetime of the photosensitizer excited state results in a higher probability for further photochemical interactions or for electron spin change from the excited singlet state to an excited triplet state due to intersystem crossing conversion. The excited triplet state of photosensitizers is where the two types of photosensitization pathways (Type I and Type II) emanate in the presence of molecular oxygen to create singlet oxygen or other reactive oxygen species. Type I reaction pathway is a radical or redox reaction while type II reaction is an energy transfer process usually via singlet oxygen formation. Most PDT photosensitizers show type II interaction[17]. The result of both types of reaction pathways is the oxidation of biomolecules causing therapeutic effect by direct cellular destruction, vasculature stasis, or other pathways. Upon returning to ground state, the photosensitizer is recycled and may participate in further photochemical interactions.

2.1.2 Hematoporphyrin Derivative

A major contribution to the field of modern photodynamic therapy was the study and development of hematoporphyrin and hematoporphyrin derivative (HPD) in the 1980's. The various review articles cited in this thesis covers this topic quite well; thus, I will only give a brief overview here. Many early studies of photosensitization involved hematoporphyrin and HPD. HPD was a much better photosensitizer than pure hematoporphyrin but was difficult to produce consistently as there are so many different isomers in the mixture. Quadra Logic Technologies Inc. (commonly known as QLT) found a

systematic method and patented a formulation of HPD calling it PHOTOFRIN. PHOTOFRIN has various absorption peaks with the most useful one for PDT being 630 *nm*. Other shorter wavelength absorption peaks existed but were not applicable for *in vivo* photoactivation due to shorter effective tissue penetration from scattering and hemoglobin absorption. PHOTOFRIN also showed florescence with ultraviolet excitation which has been utilized as a metric for dosimetry. This has been achieved using a second, ultraviolet excitation source to induce the fluorescence. HPD was found to exhibit preferential uptake by malignant tissue and clinical trials with HPD for photodynamic therapy in various oncological applications arose across North America and Europe. PHOTOFRIN became the *de facto* standard for PDT studies with HPD. Many other photosensitizers emerged around the same time for anti-cancer applications as drug companies raced to create the next best photosensitizer and gain market share in the field. On April 19, 1993, PHOTOFRIN was approved by the Canadian Health Protection Branch for treatment of superficial papillary bladder cancer. This was a milestone in PDT as this was the first drug to officially gain government approval.

2.1.3 Second-Generation Photosensitizers

From work on early "first-generation" photosensitizers, such as HPD and other early photosensitizer, researches recognized various important properties to be had for future photosensitizers and have coined the term "second-generation" photosensitizers. These properties are outlined in Kessel's[27] review:

1. Longer photoactivation wavelength than 630 *nm*. Preferably 650 *nm* or longer.

2. Strong absorption at the photoactivation wavelength.

3. High quantum yield for singlet oxygen.

4. Minimal dark toxicity.

5. Short skin photosensitization.

6. Relatively stable against photobleaching.

7. Preferential uptake in malignant tissue.

Some of these properties as they apply to SL-052 will be discussed in more detail in section 2.2.

2.1.4 Hemoglobin Absorption

The penetration depth of visible light in tissue is highly dependent on wavelength and hemoglobin concentration. In the visible light range, oxy-hemoglobin (HbO_2) and deoxy-hemoglobin (Hb) have exceedingly high absorption coefficients compared to other prostate constituents; however, their absorption properties decrease with increasing wavelength. Therefore, it is beneficial to have a longer wavelength photosensitizer excitation light if one desires for longer penetration depth and larger treatment volumes with less losses from hemoglobin absorption. Figure 2.1 shows the absorption spectrum for HbO_2 and Hb from red to near infrared, the typical range for photosensitizer therapeutic light excitation. Note that HbO_2 absorption rises rapidly as wavelength decreases from about 650 nm; hence, having longer photosensitizer excitation wavelengths in the range between 600 nm and 650 nm may contribute to significantly less hemoglobin absorption losses. This is a significant absorption

effect that photosensitizer developers must take into account if the drug is meant to treat non-superficial lesions using minimal number of light delivery sites.

2.2 Photosensitizer SL-052

2.2.1 Overview

SL-052 is a drug developed by Dr. William Lowen and our PDT group at the University of Alberta (Edmonton, Canada) for use as a photosensitizing agent for PDT. The technology was transferred to Alta Rex, then AltaChem Pharma, and finally to our current supplier Quest Pharmatech Inc. (Edmonton, Canada). It is a hypocrellin derivative and like many other photosensitizers, it is lipophilic. One of the most unique properties of SL-052 compared to other photosensitizers is that it displays near infrared fluorescence when excited for photo induced toxicity at the therapeutic wavelength. Unlike drugs that are photosensitive at a therapeutic wavelength and require a second, shorter, diagnostic wavelength to induce fluorescence, this distinctive property of SL-052 allows for simpler fluorescence detection hardware for dosimetric purposes as well as allow for real-time simultaneous monitoring of drug fluorescence and tissue transmissivity at the therapeutic wavelength.

2.2.2 Absorption

The absorbance of SL-052 was captured using a spectrophotometer (DU 640B, Beckman Coulter) and prepared in DMSO (Dimethyl Sulfoxide 99.9%, Fisher Scientific) solution at 40 $\mu g/mL$. The absorbance is converted to

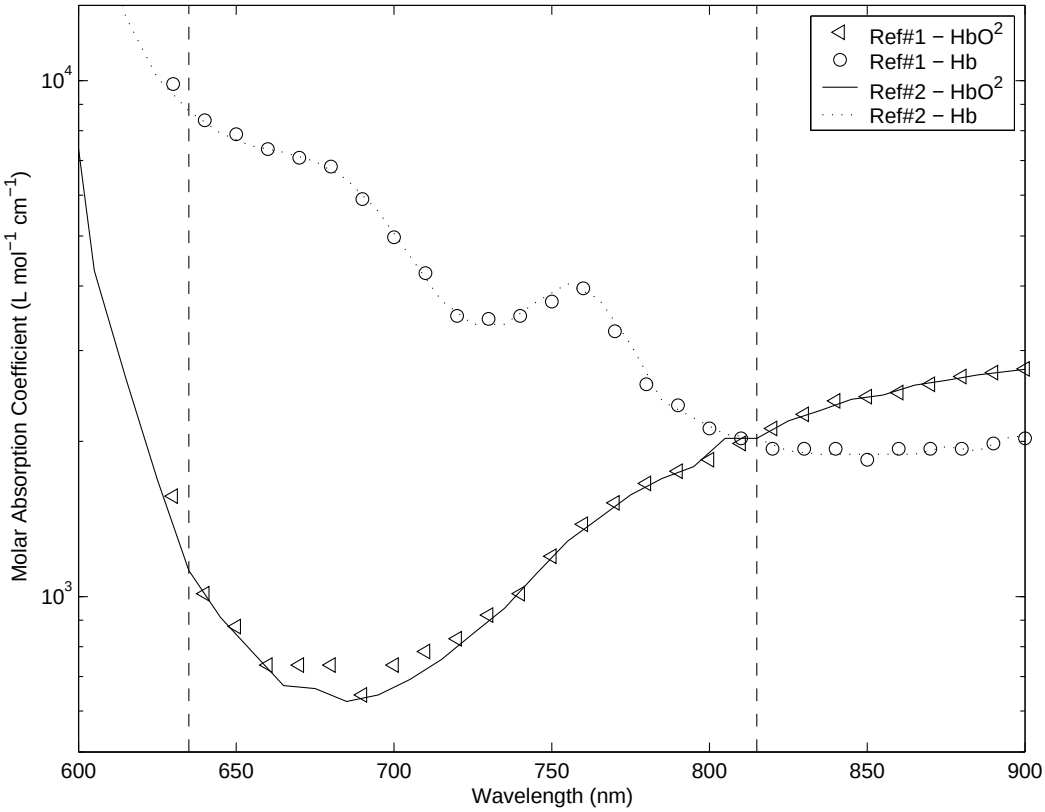

Figure 2.1: Oxy- and deoxy-hemoglobin (HbO_2 and Hb respectively) absorption spectrum. Data compiled from Schmitt[29] and Moaveni[30] for Ref#1 and Takatani[31] for Ref#2. The two vertical lines are at 635 nm and 815 nm representing respectively SL-052 excitation and fluorescence wavelengths chosen for investigation.

the more useful in optics molar absorption coefficient using equation 2.1 and is shown in figure 2.2.

$$\mu_a = \frac{-\ln\left(10^{-A}\right)}{lC} \tag{2.1}$$

where μ_a is the molar absorption coefficient, A is the absorbance, l is the path length (1 cm in this case for a standard cuvette), and C is the molar concentration of the sample, which can be calculated given the molar mass of SL-052 is 592 g/mol. The absorption profile of the photosensitizer is quite wide with a full width half maximum (FWHM) of 146 nm between 548 and 694 nm. Absorption peaks at 657 nm; however, the peak is rather flat, holding 90% of maximum value within the range between 618 and 673 nm. Consequently, the drug's absorption profile allows excitation within a wavelength range that is commercially available with robust, high powered, solid state diode lasers suitable for clinical settings for iPDT.

Referring back to section 2.1.3 on second-generation photosensitizers, SL-052 certainly meets criteria 1 with peak absorption higher than 650 nm. Ideally, the absorption wavelength should be longer to reduce tissue absorption from oxy- and deoxy-hemoglobin. However, due to certain conditions imposed by the drug supplier (see section 3.3.1) the chosen wavelength for SL-052 excitation was 635 nm. All subsequent analysis involving excitation of SL-052 will be at this wavelength unless otherwise stated.

2.2.3 Fluorescence

SL-052 fluorescence under 635 nm excitation was captured using a fiber coupled spectrometer (USB2000, Ocean Optics Inc.). A fiber coupled diode laser (7404, High Power Devices – Intense Co.) with laser line clean-

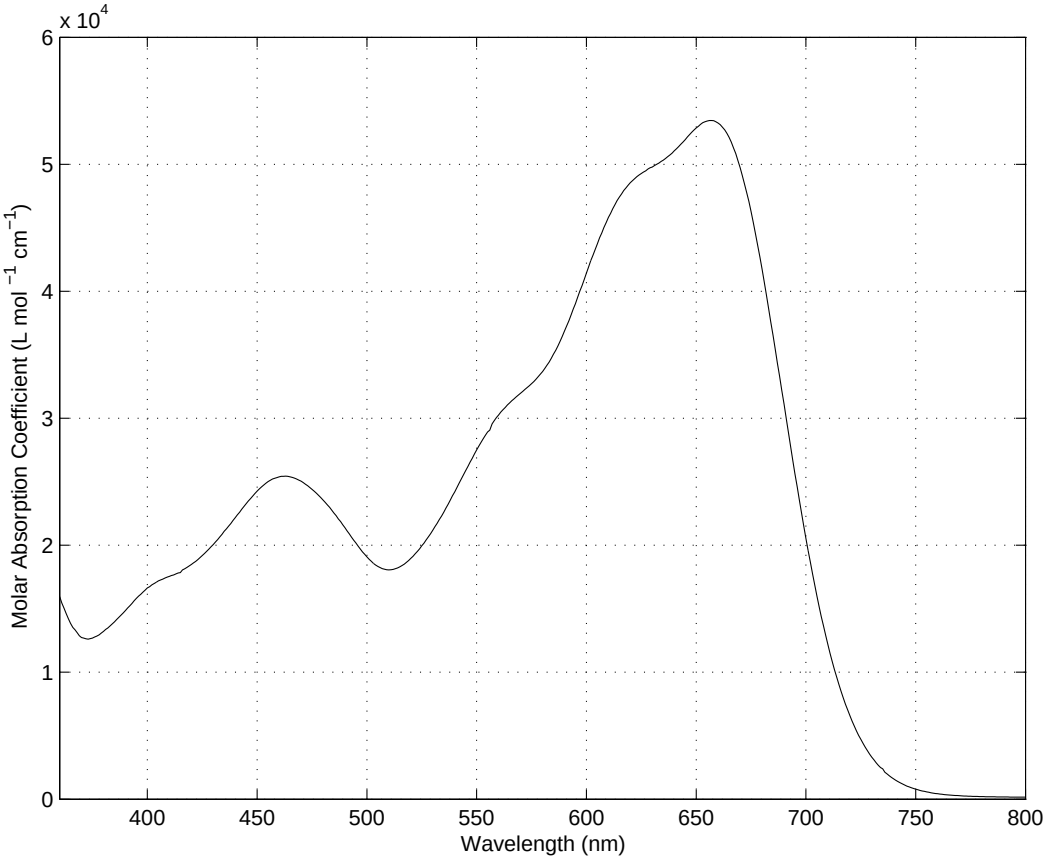

Figure 2.2: Molar absorption coefficient for SL-052

up filter (z635/10x, CHROMA) acted as the source to excite SL-052 through a standard cuvette. A high-pass filter (2mm RG665, CHROMA) was used in front of the spectrometer to prevent 635 nm excitation light from saturating the spectrometer CCD array. Figure 2.3 depicts the profile. The fluorescence profile of the hypocrellin derivative SL-052 is similar to the fluorescence profile of hypocrellin-B derivative examined by Xu[32]. The fluorescence feature has a FWHM of 63 nm and peaks at 775 nm.

Although the fluorescence peak is at 775 nm, the intensity of fluorescence used for dosimetric calculations is measured at 815 nm. More precisely, the fluorescence intensity is determined by integrating the spectrometer counts over a 10 nm range centered about 815 nm. There are several reasons for this choice. Firstly, the integration about a 10 nm range is simply to reduce noise. The reasons for choosing 815 nm are as follows:

1. Note that the fluorescence profile at 635 nm excitation falls within the tail end of the photosensitizer's absorption profile. This signifies that self-shielding of the fluorescence light can occur. Therefore, the higher the concentration of SL-052, the more the fluorescence peak will red shift due to SL-052 reabsorption, reducing the measured intensity. The main purpose of measuring fluorescence signal is to use it as one of the metrics for determining drug concentration. When self-shielding does not occur, and assuming the number of photons is much greater than the number of SL-052 absorption events, then there is a linear relationship between the detected fluorescence signal and the photosensitizer concentration. When the concentration doubles, one would expect a doubling of the fluorescence counts. However, when self-shielding exists, then there is a reabsorption probability of the fluorescence signal that is a function of

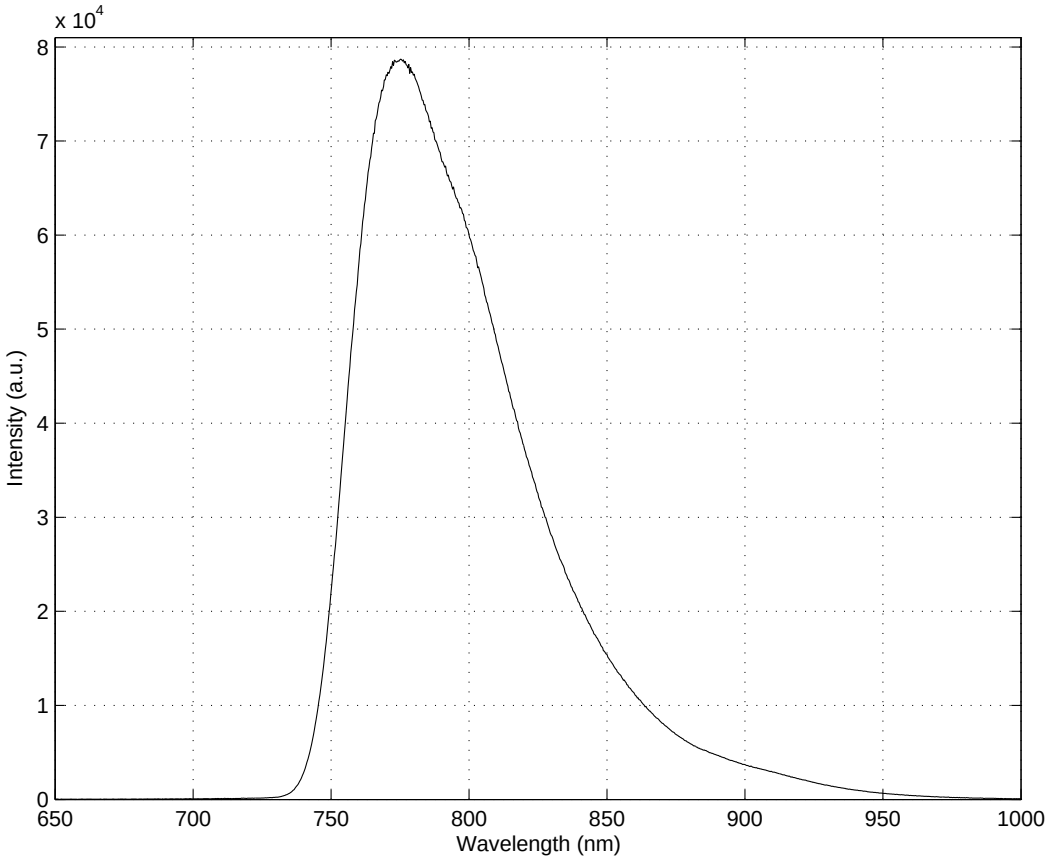

Figure 2.3: Fluorescence spectrum of SL-052 under 635 nm excitation

photosensitizer concentration. In this case, the linear relationships is lost and greatly complicates the use of fluorescence signal to determine drug concentration. Therefore, it is more reliable to base fluorescence intensity off of longer wavelengths for dosimetric calculations. For wavelengths longer than 800 nm, this self-shielding effect becomes negligible for SL-052.

2. During the photochemical reactions of PDT, oxygen is consumed and HbO_2 is converted into Hb. Because the absorption coefficient for HbO_2 is different than that of Hb, the absorption of fluorescence signal through tissue is a function of oxygen concentration. This adds an extra degree of complexity when determining photosensitizer concentration from fluorescence. Fortunately (see sigure 2.1), there is an isosbestic point at 815 nm where the absorption coefficient of HbO_2 and Hb are the same[1]. Choosing to measure fluorescence at 815 nm effectively avoids changes in signal due to oxygen consumption.

3. The third reason for choosing 815 nm is related to autofluorescence and equipment hardware generated spectral noise. This is covered in Section 3.5.2.

2.2.3.1 Implications and Discussion

To the best of this author's knowledge, there are no available photosensitizers that create both photodynamic therapeutic effect and significant photo induced fluorescence at the same excitation wavelength. Laser induced fluorescence has been used to facilitate treatment dosimetry since at least the

[1]Note that this is using data for Ref#2 and #3 in the figure. These two references are more reliable than Ref#1 as they are peer reviewed sources.

first-generation PHOTOFRIN, and has been used in investigations with subsequently discovered photosensitizers. However, to implement fluorescence detection with these photosensitizers places a large burden on the technical aspects of treatment hardware:

1. The hardware must have two laser sources, one therapeutic light source for photochemical reaction and one to induce fluorescence. This immediately places an economic burden on the system as well as increase system size and decrease portability in a hospital environment where space is a premium.

2. With the second source, there is still the problem of how to delivery the light into the tissue. Most existing systems for interstitial treatment use fibers to delivery the excitation light. One could simply chose to insert more fibers into the treatment volume for the fluorescence inducing source but this greatly increases the invasiveness of the treatment. Another method, often used, is to swap the light source of existing fibers from the therapeutic light to the ultraviolet light for a detection phase. This works, but requires breaks in the treatment resulting in longer therapy length as well as only detecting fluorescence information at small fragments of time. This also requires either a computer controlled switch or a human operator to physically switch the sources. The third possibility is to pump both colors down the same fiber at the same time. This would require expensive multiplexer equipment.

3. The fluorescence inducing source is usually of shorter wavelength, often in the ultraviolet range. This range has very little transmission through tissue due to high hemoglobin absorption in the ultraviolet range. The

short transmission results in a fluorescence signal that is only representative of the situation near the excitation source and not throughout the treatment volume.

4. Prolonged exposure at a second wavelength results in possible axillary effect to the photosensitizer (extra photobleaching, or extra photochemical activation) in the small local region within the short penetration depth as well as possible axillary tissue effect depending on the fluence output of the second source.

With an unlimited budget, large research space, and non-human test subjects, most of these problems are easy to over come. However, these obstacles create engineering problems when building a system that is marketable and useful in a clinical setting for human patients.

The ability of SL-052 to displays near infrared fluorescence when excited at the therapeutic wavelength for photo induced toxicity allows the use of just a single excitation wavelength, completely eliminating issues 1 and 2. Since the fluorescence and photochemical activation is via the same wavelength, then the resulting fluorescence signal is representative of the entire region of treatment. Prolonged exposure is not an issue as we do not have secondary effects from a second wavelength, allowing continuous and real-time fluorescence detection to operate simultaneously with therapeutic light delivery. This is a major advantage of SL-052.

2.2.4 Photobleaching

Photobleaching is a typically undesirable effect that happens to the photosensitizer during photochemical reactions. Photobleaching is when reactive

species which are products of photosensitizer, light, and oxygen, end up reacting with the photosensitizer, resulting in irreversible effects that inhibit the photosensitizer from participating in further photochemical reactions. In essence, the photosensitizer is not recycled in this photobleaching pathway and is eliminated from the active photosensitizer pool, thereby reducing the existing drug dose. There may also be instances of reversible photobleaching where the photosensitizer is temporarily taken out of an active form but may become functional again later in time.

According to studies done by the drug supplier, SL-052 exhibits no detectable photobleaching effect. Experiments were performed by measuring the phototoxic effect of SL-052 on two dimensional cell arrays with solution samples of SL-052 that have been pre-exposed to varying amounts of 635 nm excitation. They reported no loss in toxicity. However, as we shall see in section 4.5.2, this photobleaching data may not be applicable for our applications.

2.2.5 Skin Photosensitivity

Skin photosensitivity is an inconvenient side effect of certain photosensitizers. Due to uptake of drug by skin cells, the patient may incur photochemical burns to the skin when exposed to light levels for everyday routines. Depending on the photosensitizer, this may mean the patient must remain in a dark, or at least light reduced room for days to weeks post PDT. This is an expensive (hospital rooms) side effect of certain photosensitizers and causes great inconvenience for the patient. The drug supplier provides that SL-052 induces no significant skin photosensitivity, although precautions are still taken for animal trials.

2.2.6 Other photosensitizers that were trialed

Aside from SL-052, another photosensitizer SL-066 (Quest Pharmatech Inc.) also underwent optical examination to determine suitability for iPDT. While according the supplier, SL-066 showed higher photoactivated toxicity, the drug was abandoned as an iPDT candidate due to inconsistent fluorescence. While SL-052 showed 635 nm excitation light induced fluorescence in both the liposomal formulation and DMSO formulation of the drug (see section 4.2.1 for drug formulations), our testing with SL-066 showed fluorescence only in the DMSO formulation. For this reason, further investigation of SL-066 was dropped from my research.

2.3 Tissue Optics and Foundations for Photosensitizer Dosimetry

Dosimetry is the process or method for measuring the applied treatment dose. As applied to iPDT, the doses involved are: photosensitizer concentration in the local treatment volume, excitation light dose, and local oxygen concentration. In general, accurate dosimetry allows for correlation between delivered dose and therapeutic effect such that correct dosages can be prescribed to future patients.

The local concentration of oxygen is difficult to control and heavily depends on the tissue or cancer type. For iPDT of prostatic carcinoma, we assume the organ is well oxygenated enough such that oxygen will not be the limiting reagent. If there are local hypoxic regions in the treatment volume, either due to aggressive cancer growth or due to PDT itself shutting down tissue

vasculature and consuming the remaining oxygen, then we have a situation where oxygen would be the limiting reagent. However, such regions are of no concern because the region would be failing from hypoxia or ischemia anyways.

This section deals with the methods for facilitating the determination of photosensitizer concentration. The object of photosensitizer dosimetry is to quantitatively determine *in vivo* SL-052 concentration. The foundation for this analysis is based on the high absorption coefficient of the drug. The idea is, the presence of the drug will significantly alter the optical properties of the prostate such that concentration information can be extracted. The assumption is that the absorption coefficient of the section of prostate being sampled increase monotonically with respect to increase in local drug concentration. A reference matrix (calibration table) can be created for varying *in vivo* source and detector separation distance and SL-052 concentration. This allows for detection of photosensitizer concentration in various subsections of the prostate (depending on setup) at the onset of iPDT. The reference matrix must be created in a controlled environment with known optical properties similar to that of the prostate. This section will discuss light penetration through tissue and the diffusion approximation. Using the diffusion approximation, an optical phantom mimicking the optical properties of prostate tissue is created. The creation of the calibration table using this optical phantom can be found in section 3.5.1 after introducing the iPDT system.

2.3.1 Light Propagation in Turbid Media

Treatments of light propagation in biological environments usually disregard the wave nature of light. In most circumstances for PDT, the elements of interest are fluence or radiance (fluence per solid angle); wave properties such as

polarization, diffraction and interference are of no interest. A fundamental rigorous approach would require solving Maxwell equations through spatially and temporally varying dielectric medium. In multi-scattering environments, a statistical ensemble of the solution to field contributions from all particles would be necessary. Although this rudimentary approach maintains wave properties, it does not lead to solvable equations for any problems of practical importance. Instead, treatments of light propagation in biological environment deals with problems of discrete photon transport modeled by the transport equation. It is a specialized form of the Boltzmann equation from statistical mechanics. It describes the transfer of photon energy by modeling the change in radiance and is as follows:

$$\hat{\boldsymbol{s}} \cdot \nabla L(\boldsymbol{r}, \hat{\boldsymbol{s}}) = -\left(\mu_a(\boldsymbol{r}) + \mu_s(\boldsymbol{r})\right) L(\boldsymbol{r}, \hat{\boldsymbol{s}}) + \mu_s \int_{2\pi} p(\hat{\boldsymbol{s}}, \hat{\boldsymbol{s}}') L(\boldsymbol{r}, \hat{\boldsymbol{s}}') d\omega' + S(\boldsymbol{r}, \hat{\boldsymbol{s}}) \quad (2.2)$$

where $\hat{\boldsymbol{s}}$ is a unit vector, $\boldsymbol{r}$ is the position vector, μ_a is the absorption coefficient, μ_s is the scattering coefficient, L is the radiance, p is the normalized scattering phase function, and S is the source term. This integral-differential equation relates the gradient of the radiance at a position $\boldsymbol{r}$ and direction $\hat{\boldsymbol{s}}$ to the changes in radiance due to all losses and gains. The losses at position $\boldsymbol{r}$ are from absorption and scattering away from direction $\hat{\boldsymbol{s}}$ and gains from the sum of scattering back into direction $\hat{\boldsymbol{s}}$ as well as the source term in direction $\hat{\boldsymbol{s}}$.

The transport equation, while intuitive and elegantly formalized for radiative energy transport in turbid media, still only has analytical solutions for a small number of trivial cases. Diffusion theory approximates the transport equation and models light transport in turbid media as a diffusion of energy. The derivation of the diffusion equation is discussed in detail in Star[33]. In spherical geometry, the diffusion equation can be expressed as follows:

$$\left(\frac{1}{r^2}\right)\frac{\partial}{\partial r}\left\{r^2\left[F_{r+}(r)-F_{r-}(r)\right]\right\} = -2\mu_a\left[F_{r+}(r)+F_{r-}(r)\right] + \mu_s\left(\frac{P}{4\pi r^2}\right)exp\left[-\left(\mu_a+\mu_s\right)r\right] \quad (2.3)$$

$$\frac{\partial}{\partial r}\left[F_{r+}(r)+F_{r-}(r)\right] = -\frac{3}{2}\left(\mu_a+\mu_s'\right)\left[F_{r+}(r)-F_{r-}(r)\right] + \frac{3}{2}g\mu_s\left(\frac{P}{4\pi r^2}\right)exp\left[-\left(\mu_a+\mu_s\right)r\right] \quad (2.4)$$

$$\phi(r) = 2\left[F_{r+}(r)+F_{r-}(r)\right] + \left(\frac{P}{4\pi r^2}\right)exp\left[-\left(\mu_a+\mu_s\right)r\right] \quad (2.5)$$

for an isotropic point source in a scattering and absorbing medium where g is the anisotropy factor, $\mu_s' = \mu_s(1-g)$ is the reduced scattering coefficient, P is the source power, $F_{r\pm}$are intermediate variables, and ϕ is the fluence. For an isometric point source in an infinite medium where $\mu_s' >> \mu_a$, the solution to the equation can be simplified (equation 2.6). The difficulty is in obtaining correct values for the optical parameters μ_a and μ_s'.

$$\phi(r) = \frac{3P\left(\mu_a+\mu_s'\right)}{4\pi r}exp\left[-\sqrt{3\mu_a\left(\mu_a+\mu_s'\right)}r\right] \quad (2.6)$$

Diffusion theory of light transport is very popular due to its simplicity and its appeal to the physical intuition of diffusion. The simplified form (equation 2.6) has been utilized to determine optical properties in various biological environments including that for the prostate[34, 21, 35, 36, 37, 38]. With today's computational power, models with less approximations exist[39, 40, 21, 41], yet diffusion theory is still widely used for canine and human prostates because of its simplicity and its ability to yield accurate results if the assumptions are met. That is, if $\mu_s' >> \mu_a$ and $r \gg 1/\mu_{eff}$, where $\mu_{eff} = \sqrt{3\mu_a\left(\mu_a+\mu_s'\right)}$ is the effective attenuation coefficient. This means diffusion approximation applies

in a scattering dominant regime with detector at many skin depths away.

2.3.2 Optical Phantom

The optical properties that describe light propagation in turbid media are the absorption coefficient μ_a, scattering coefficient μ_s, and anisotropy factor g. With equation 2.6, the solution to the diffusion equation for an isometric point source in an infinite medium, μ_s and g are combined into one term: the reduced scattering coefficient $\mu_s' = \mu_s\,(1-g)$. The objective of this section is to create a phantom to mimic μ_a and μ_s' of prostates at our treatment wavelength of 635 nm such that experiments with SL-052 and our light delivery-detection system can be analyzed in a controlled environment. Pantelides[21] reported human prostate at 633 nm had $\mu_a = 0.7\,cm^{-1}$ and $\mu_s' = 8.6\,cm^{-1}$ and Nau[42] reported canine prostate with $\mu_a = 0.73 \pm 0.07\,cm^{-1}$ and $\mu_s' = 22.5 \pm 0.5\,cm^{-1}$ at the same wavelength. In the scope of this thesis, canine trials are to be performed and thus the goal was to create an intralipid phantom with Nau's reported canine prostate optical properties.

Intralipid is a white phospholipid emulsion with high scatting coefficient and low absorption coefficient. Intralipid based optical phantoms have been discussed previously by various research groups[43, 44, 45, 46, 47] with the general result that 10% intralipid (intralipid often comes in 10% by volume concentrations) has an effective scattering coefficient ($\mu_s^{'}$) of 105–185 cm^{-1} at 633 nm. The phantom is composed of a specific dilution of intralipid solution with an added absorbing agent. The absorption of intralipid is negligible at the concentrations necessary to produce tissue like scatting, and for calculation purposes, it can be assumed to be zero. The absorption medium we used is methylene

blue because it has well known absorption coefficients and negligible scatting for our application.

Because the variation between brands of intralipid is quite large[46], we must conduct our own testing to determine scattering coefficients of our 10% intralipid (*Baxter*). This can be achieved using the diffusion approximation of light transport in a turbid (scatting and absorbing) media. As discussed in section 2.3.1, when a radially isometric source and a radially isometric detector are placed at a distance r apart in a medium with reduced scattering coefficient $\mu_s^{'}$ and absorbing coefficient μ_a, the light fluence at the detector can be described as equation 2.6.

The test medium is a solution with varying concentrations of intralipid and 2.245 mg/L of methylene blue. The methylene blue ($M = 319.85\, g/mol$) has molar concentration absorption coefficient of 103986 $L/\left(mol \cdot cm\right)$[48], corresponding to the absorption coefficient for canine prostates of $\mu_a = 0.73\, cm^{-1}$[42] at the given concentration. Using two fiber coupled spherical diffusers, one connected to a 635 nm source and the other connected to the USB2000 spectrometer, light fluence at the detector is measured at varying source-detector distances. MATLAB's unconstrained nonlinear optimization (*fminsearch*) function is utilized to perform curve fitting to equation 2.6.

Results show that at 18.2% of 10% intralipid we obtained a $\mu_s^{'} = 22.7 \pm 0.5\, cm^{-1}$, similar to that of canine prostates[42]. This corresponds to our 10% intralipid batch having a $\mu_s^{'} = 125\, cm^{-1}$ for 635 nm falling well within the range of 105–185 cm^{-1} for 633 nm described earlier.

Figure 2.4 shows the experimental results and corresponding curve fit. The intralipid phantom mixture for simulating canine prostate at 635 nm is 18.2%

of 10% intralipid (% by volume) with 2.245 mg/L of methylene blue. Note that $\mu_s' >> \mu_a$ and $r \gg 1/\mu_{eff}$ and therefore diffusion approximation holds.

In section 3.5.1, this optical phantom is applied to test the *in vitro* optical response from our iPDT system at varying SL-052 concentrations. The detected intensity of excitation light can be formed into a calibration table and be used as a metric for determining *in vivo* SL-052 concentration.

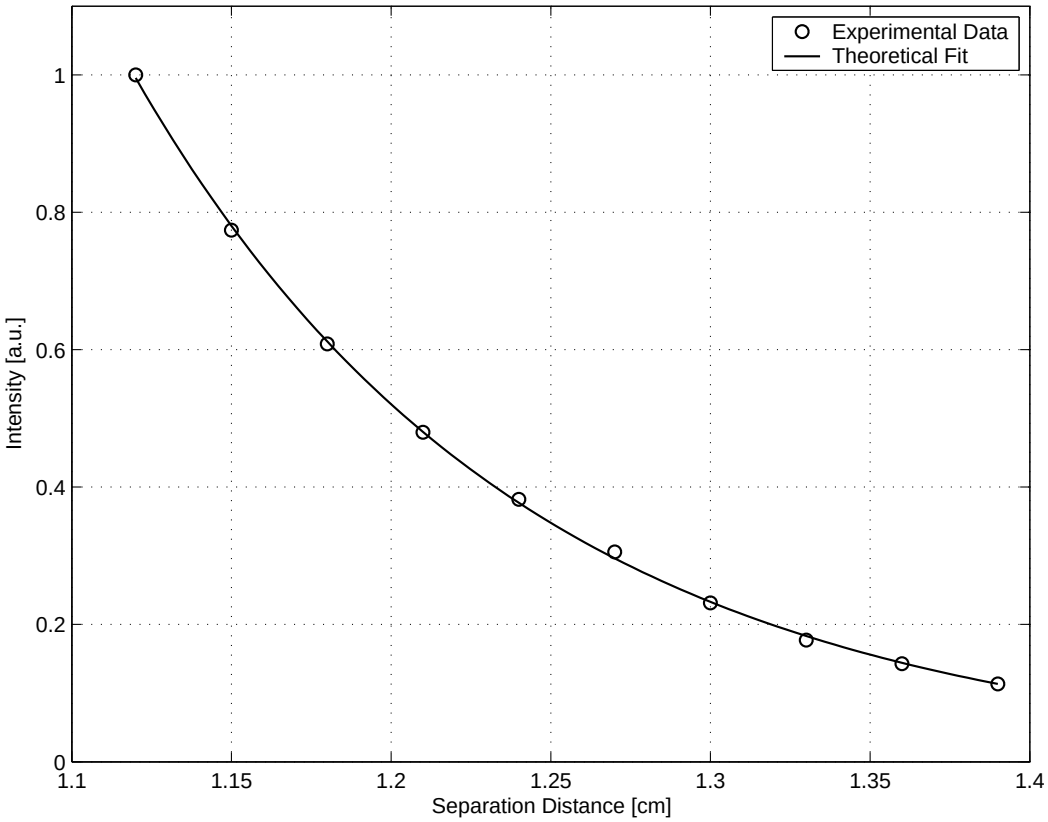

Figure 2.4: Light transmission and theoretical fit for 18.2% of 10% intralipid. Multiple tests showed similar characteristics with result of the effective scattering coefficient of $\mu_s^{'} = 22.7 \pm 0.5\, cm^{-1}$.

Chapter 3

iPDT System

3.1 Overview

A novel system for interstitial photodynamic therapy (iPDT) of prostatic carcinoma has been developed. The system hardware is designed to be robust and portable enough to be easily transportable between different clinical settings. The system is flexible and has a broad scope of capabilities which can be adapted to be used with various available photosensitizers with minimal hardware reconfiguration. Currently, this system is adapted for use with a novel hypocrellin derivative SL-052 (Quest Pharmatech Inc.) photosensitizer taking advantage of the drug's photophysical properties to allow dosimetric detection to occur concurrently with therapeutic light delivery. Both the tissue transmissivity at the excitation wavelength and photosensitizer fluorescence are monitored in real-time. As an corollary, we can show real-time photobleaching-like characteristics *in vivo* as well as provide strong evidence for the benefit of time-fractionated light delivery (see chapter 4).

Fractionated light delivery[49] involves delivering doses of light divided in time by dark or light-off phases as opposed to one continuous dose. Two critical reactants for PDT, oxygen and photosensitizer, may be locally consumed during photophysical reaction. Fractionated light delivery allows for the reaccumulation of exhausted reactants and has proven advantages compared to continuous light delivery in terms of efficacy in iPDT[50].

This chapter examins in detail the construction of the novel light delivery and detection system. It begins with a literary review of PDT systems from other research groups followed by characterization of system components. It then discusses the integration and operation of the system. Finally, this chapter concludes with *in vitro* testing of the system including formulation of the SL-052 concentration calibration table.

3.2 Literary Review

3.2.1 University of Toronto

Photosensitizer: The photosensitizer this research group uses is WST09 (TOOKAD), a palladium-bacteriopheophorbide photosensitizer. The drug is not water soluble and is administered intravenously in Cremophor-based vehicle. Due to the fast clearing of the drug, drug is administered slowly over tens of minutes with light delivery occurring concurrently for a significant portion of the time.

Treatment System: Excitation light sources are multiple 762 nm laser diodes. A beam splitter system is implemented for continuous light deliver

for up to 6 fibers. The delivery fiber coupled diffusers have a linear power density of 50-300 mW/cm and delivers doses between 100-360 J/cm. Several techniques for monitoring the *in vivo* concentration of WST09 have been investigated by the group. 8 photodiode detectors can used for fluence monitoring in real-time during light treatment. The photodiodes are coupled with isotropic probes. The fluence changes with respect to drug concentration. Whole blood can be collected during treatment and absorption spectrum could be used to determine blood concentrations of WST09. Diffuse transmittance of white light could also been measured and small increase in absorption at 760 nm can be observed during drug administration. This can not occur concurrently with therapeutic light delivery due to this light interfering with the white light source.

Reference: Weersink[51]

3.2.2 Lund Institute of Technology

Photosensitizer: This group intratumorally administed δ-aminolevulinic acid-induced protoporphyrin IX (ALA-induced PPIX) photosensitizer 30 minutes prior to treatment.

Treatment System: 6 bare-end optical fibers deliver 635 nm therapeutic light from 6 diode lasers with treatment power between 25-100 mW and light dose between 70-495 J. PPIX presence is confirmed using 405 nm laser induced fluorescence detected by a spectrometer. This was performed prior to therapeutic light delivery using one of the 6 bare-end fibers. A light distribution module is used to rotate a LED with output range of 760-810 nm into the 6 fibers while using another fiber for detection via spectrometer. Blood

oxygenation can be extracted from tissue transmission by assuming changes in transmission is only due to oxy- and deoxy-hemoglobin exchange.

Reference: Johansson[52]

3.2.3 University of Pennsylvania

Photosensitizer: This group uses motexafin lutetium (MLu) photosensitizer for mediating PDT. Prescribed drug doses varied between 0.5-2.0 mg/kg body weight and was administered intravenously with drug-light interval (time between drug administration and light delivery) was tested at 3, 6 and 24 hours.

Treatment System: 732 nm therapeutic excitation light was delivered at 150 mW/cm through 4 cylindrical diffusing fibers with prescribed light fluence varying between 25-200 J/cm^2. Each quadrant of the prostate was treated sequentially. Multiple isotropic detectors were connected to photodiodes for fluence detection and detection of MLu light-induced fluorescence from 460 nm LED source. Fluorescence detection and 460 nm LED source utilized the same fiber via dichroic beam splitter system.

References: Zhu[53], Du[54] and Finlay[55]

3.2.4 University College London

Photosensitizer: The photosensitizer this group investigates is Meso-tetra-hydroxy-phenyl-chlorin (mTHPC, FOSCAN). 0.15 mg/kg of drug was administered intravenously with drug-light intervals of 2-5 days.

Treatment System: The group experimented with bare tip delivery fibers as well as cylindrical diffusing fibers at up to 4 sites per prostate treated sequentially. The therapeutic light source was a 652 nm diode laser delivering 50-100J per site. Power output for bare tip fibers were at 150 mW while cylindrical had output of 100 mW/cm. There were no dosimetric apparatus for any type of detection.

References: Moore[56] and Nathan[23]

3.2.5 University of Toronto, McMaster University

Photosensitizer: Early research from this group investigated the photosensitizer PHOTOFRIN. Drug administration was made intravenously at doses between 1-5 mg/kg.

Treatment System: The therapeutic light source was an argon-dye laser at 630 nm. Total energy delivered was 400J with an output power of 100 mW. The delivery fiber is a spherical diffuser tip fiber. Two more similar fibers are used as fluence probes and connected to power meters for continuous monitoring of light fluence during therapeutic light delivery.

Reference: Chen[57]

3.2.6 University of Toronto, Medical College of Ohio

Photosensitizer: This group studied tin etiopurpurin dichloride (SnET2) mediated PDT. Intravenous drug administration of SnET2 in lipid emulsion vehicle occured at a drug dose of 1.0 mg/kg. Drug-light interval was delivered 24 hours.

Treatment System: 660 nm excitation source was provided by a six-channel laser diode system delivering light through fibers coupled with cylindrical diffuser tips. Light doses prescribed was 200 J/cm at a linear power density of 200 mW/cm. Up to 3 isometric probes were also placed into the prostate for fluence detection during irradiation.

Reference: Lilge[58]

3.3 System Components

A major component to this project is to create a multi-foci light delivery and detection system that is push cart portable and fully computer controlled. The system should be able to deliver light to the prostate using time-fractionated light delivery at 7 different sites and with the capability of expanding up to 13 sites. The system needs to be able to detect changes in tissue transmissivity at the excitation wavelength and monitor changes in photosensitizer fluorescence. While the current setup of the system is customized for use with SL-052, it should be able to be easily adaptable to other photosensitizers.

The current iPDT light delivery and detection apparatus is composed of an integration of many subsystems. This section concentrates on explicating each individual subsystem while section 3.4 illustrates the system integration and operation.

3.3.1 Excitation Source

While the photosensitizer SL-052 has a peak absorption at 650 nm, the drug company insisted on 635 nm lasers despite tissue penetration depth being

greater at 650 nm. Because SL-052 has a board absorption profile that remains relatively flat holding 90% of peak value within 618 and 673 nm, 635 nm is an acceptable excitation wavelength. High precision of laser wavelength output or high beam quality are not necessary as long as absorption occurs and that photodynamic reactions can be induced at that wavelength. This was demonstrated to be the case at 635 nm according to the drug supplier.

It is desirable practically, medically, as well as economically for iPDT to be as quick as possible. Practically, it is simpler for for medical and technical personnel to remain on scene for no more than a few hours. It is also easier to ensure fiber positions do not creep over a shorter light illumination period. Medically speaking, because patients undergoing iPDT will require anesthesia, it is much safer for patients to remain under anesthesia for shorter amounts of time. Economically, the shorter the treatment, the lower the operating costs associated with personnel and surgical facility. Therefore, it is desirable for iPDT laser fluence to be as high as possible without inducing thermal damage in tissue. We chose a target fluence rate between 200–350mW at the diffuser end to ensure relatively fast treatment times while staying below thermal threshold.

Another desirable specification is laser stability over treatment time. This is important for accurate light dosage delivered as well as for accurate monitoring of changes in tissue absorption and photosensitizer fluorescence. While it is possible to have a continuous power monitor at the output of each laser module, the extra costs and complexity added to the entire system is not desirable. Laser light is to be delivered to target tissue via fiber optics. Therefore, the laser sources should be fiber coupled.

The chosen lasers are a pair of 635 nm HIGH POWER DEVICES (North Brunswick,

USA) 7404 fiber coupled diode laser modules. These turn key devices are robust and compact (4" $\times$ 8.5" $\times$ 12") enough for frequent transportation between lab and operating room. They are specified with a minimum of 500 mW continuous wave output and should be sufficient to deliver the target fluence rate allowing for a margin of 4dB power loss through fiber connections. The lasers are multimode and have a board emission profile centered around 635$\pm$2 nm. Experimentally captured emission spectra show good agreement with manufacture provided data sheets for both lasers. The spectral profile of one laser is shown in figure 3.1 captured using the USB2000 spectrometer. The lasers have output FWHM of 8$\pm$1 nm. The width of this emission profile is completely acceptable for our applications. Figure 3.2 depicts the stability of laser #1 over 3 hours. While the laser diodes are TEC (thermoelectric cooler) temperature controlled, the modules require approximately 10 minute warm up time before stabilization. This is might be due to time necessary for other electrical component to reach temperature stability. This initial fast power drop is not present upon subsequent power on cycles as long as the laser module has not had enough time to cool down. The fluctuation over 3 hours is less than 1% and is acceptable for our applications. The laser modules are also equipped with RS-232 interface for computer controlled output. While this was not utilized for the scope of this thesis, it is advantageous for future considerations.

3.3.2 Fiberoptic Electromechanical Switch

There are several ways to delivery light from one source to multiple fibers. Some system employ beam splitters[59] and deliver continuous light to all sites at the same time equally dividing the power between each site. While

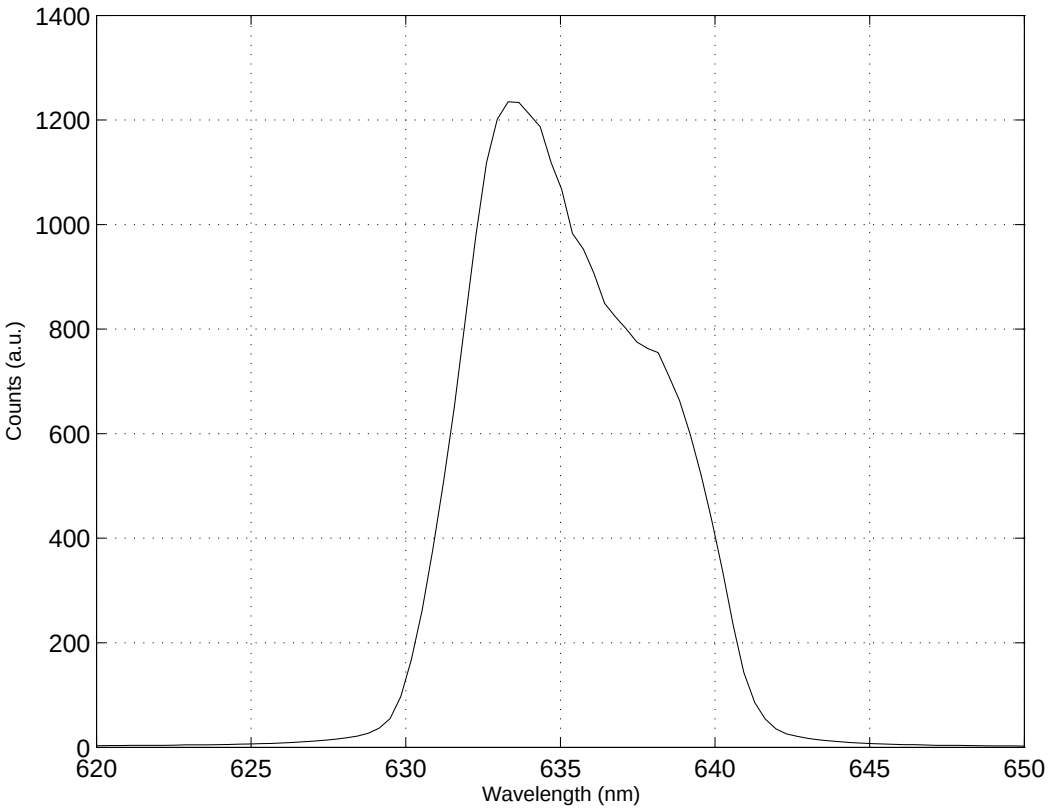

Figure 3.1: Measured HPD 7404 laser line spectrum

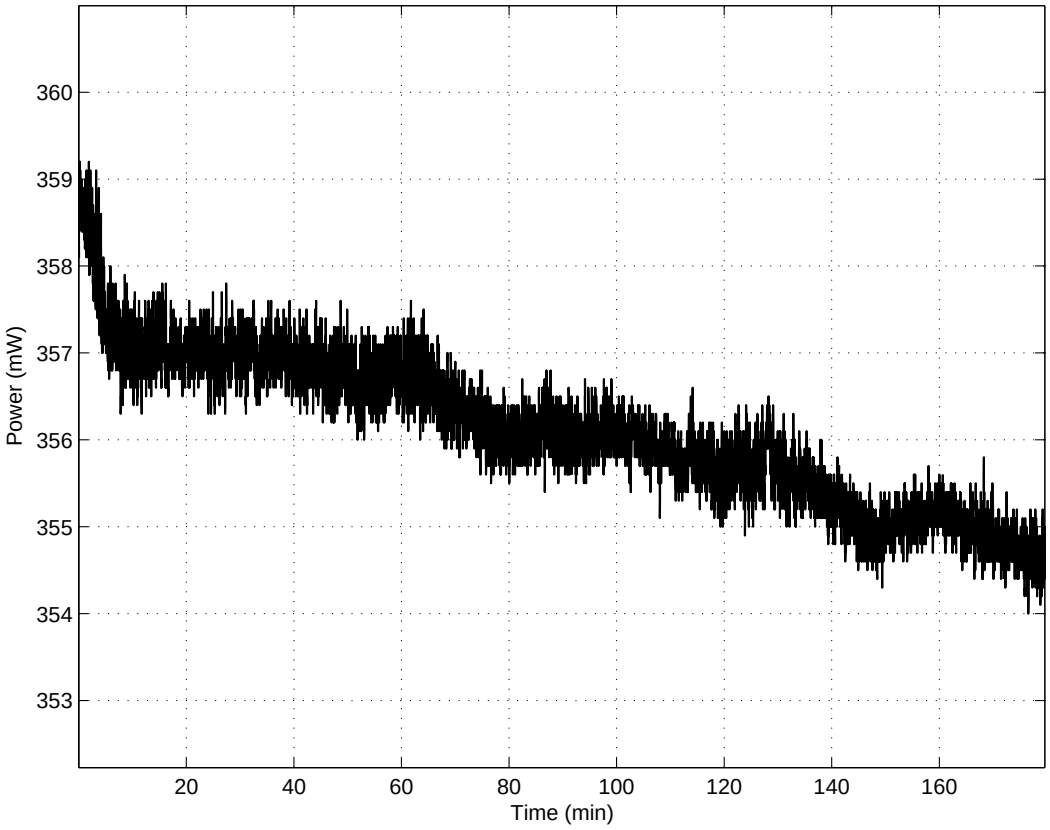

Figure 3.2: Three hour stability of laser #1. After 10 minutes warm up time, the output stabilized to within 1% over 3 hours. Laser #2 showed similar stability.

such a system is may be robust, it does not flexible and does not lend itself well to reconfiguration to different number of fibers, especially odd numbers. Because time-fractionated light delivery has shown higher efficacy[50], we want to avoid the beam splitter method. Instead, each laser will only delivery light to one fiber at a time and switching between the fibers after a given interval. This creates a light-on and light-off cycles at each fiber position giving the time-fractionated delivery.

The fiberoptic switch (LT3000, LIGHTECH, USA) is composed of 2 modules of 3×9 switches. Precision motors physically align internal 200 μm 0.22 NA multimode fibers (THORLABS, Germany) to sets of FC bulkhead connectors. The switch can be controlled via physical control panel or GPIB (IEEE-488) bus. Testing showed excellent internal alignment with losses within 1dB while new. Note, this switch, as well as other fiberoptic devices suffers from losses over time due to repeated reconnections with patchcords. The wear and tear can cause scratches greatly reducing transmissivity. An older model of the switch (SMA connectorized) shows losses between 2–3dB from repeated use. LABVIEW test codes were created for timed repeated switch and switch confirmation cycles and showed that switch times are well below 150 ms which is insignificant compared to treatment time. Switch times for the scope of this thesis can be assumed to be instant.

3.3.3 Light Detectors

The primary light detector for the current system is a compact, fiber coupled, USB spectrometer (USB2000, OCEAN OPTICS, USA). The spectrometer contains a 600 lines per millimeter diffraction grating and a 2048 element linear CCD array with an entrance aperture of 200 μm. An optional collection

lens was fitted to improve sensitivity. The spectrometer is calibrated for the wavelength range 380–1050 nm and has a specified FWHM of 10.0 nm. Wavelength calibration checking was performed by comparing using typical T-11 commercial fluorescent lighting emission spectra from laboratory with a reference (Figure 3.3). Note that each bulb manufacturer uses different ratios of elements and produce different relative magnitudes of peaks. What is important for wavelength calibration is to check that the peaks are at the correct locations. This ensures the diffraction grating and CCD array has not shifted in the spectrometer. Due to FWHM of 10.0 nm, the peaks from USB2000 are more broad than the reference.

An integrating sphere (13PDH003, Melles Griot, USA) coupled universal optical power meter (13PDC001) is a convenient and easy to use device for measuring laser output power from fiber aperture as well as power output at the diffuser. The meter is calibrated to power measurements by inputting the wavelength of the light source and has an automatically adjusting amplifier allowing it to detect power ranges between 1 W to the system's minimum detection resolution of 1 nW. However, the detection limit for the system is on the order of 10 nW due to the system dark current of a few nW.

3.3.4 Fiberoptic Technology

The choice to use fiberoptic technology to delivery the excitation energy is an obvious one. It is the only technology available that is practical for guiding light into the target tissue. For PDT of superficial lesions where only surface illumination is necessary, there may be other available technologies, but not for iPDT. Fiberoptic delivery also has the advantage of leaving a small surgical

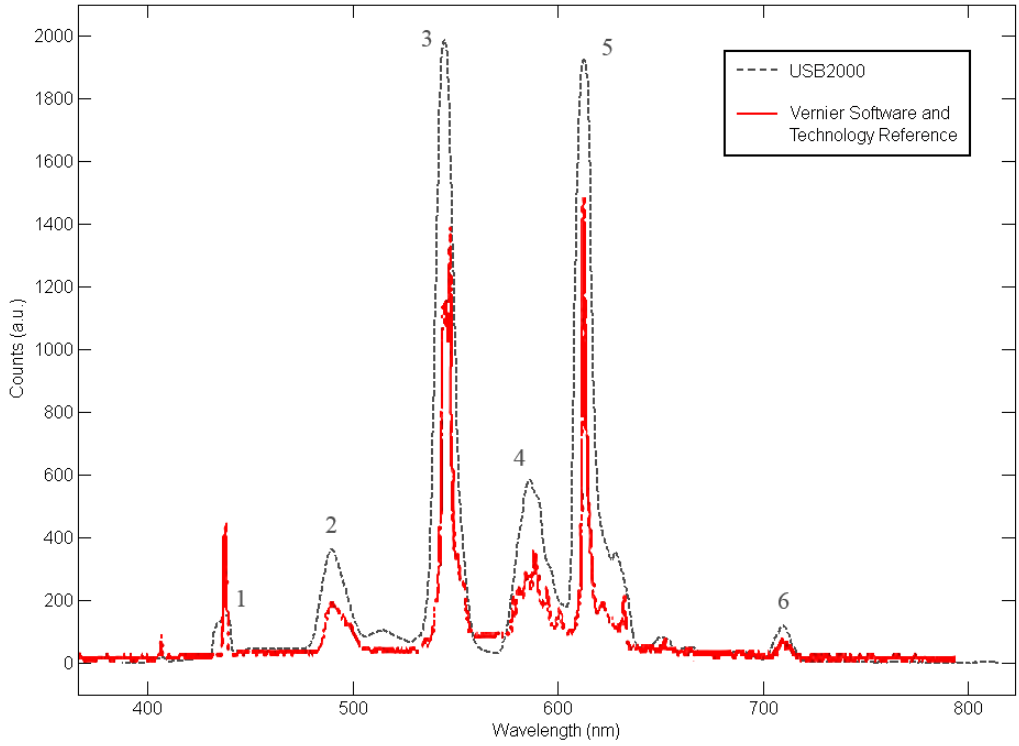

Figure 3.3: USB2000 spectrometer calibration check – USB2000 captured emission spectra of typical T-11 plotted against reference spectra[60]. Each bulb manufacturer uses different concentrations of elements and accounts for the relative magnitude differences among the peaks. Peaks 1, 2, 3, 4, 5 and 6 corresponds respectively to 436 *nm* mercury, 487 *nm* terbium, combined 544 *nm* terbium and 546 *nm* mercury, combined 577–598 *nm* of terbium and europium, 611 *nm* europium, and combined 707, 709 and 712 *nm* of europium[61, 62, 63, 64].

footprint and is one of the main advantages of PDT over traditional surgical methods.

3.3.4.1 Connector Standard

While the telecommunications industry have long abandoned SMA connectors, the medical lasers industry have been slow to adopt newer, more advanced connector specifications. For our system we chose to adopt the FC connector standard over SMA for several reasons:

1. FC connectors are spring loaded while SMA connectors are not.

   Spring loaded connectors maintain an acceptable level of contact pressure and prevents over tightening of connectors. Because polished connector ends come into physical contact to make the optical connection, over-tightening could result in cracking of fiber tip severely impacting the light transmission. Any dust and debris can also easily scratch the polished fiber ends or even crack them when overtightened. SMA connectors do not give enough of a tactile feel for sufficient tightness. In our lab, our old iPDT system was SMA connectorized and have been plagued with power losses due to scratched connectors. While scratched external patchcords can be repolished relatively easily, repolishing internal connectors such as connectors in the laser module or in the fiberoptic switch are difficult and expensive. Spring loaded FC connectors offers better equipment longevity for our applications where repeated reconnections are common during testing and optimization of equipment.

2. FC connectors have fixed rotational orientation while SMA connectors do not.

FC connectors have a tab that locks in the rotational orientation between the two connectors. This allows FC connectors to be polished with matching angled surface. The angled surface reduces back reflection and laser feedback which can cause laser instability and reduce laser lifetime. HPD, the laser module supplier, have specifically told us to minimize feedback or else the laser diode can burn out.

3. FC connectors in general have better insertion loss than SMA connectors.

   Because FC connectors offers higher precision alignment, there is lower insertion losses. This is important from an engineering standpoint as this allows for a lower requirement for laser source output power and may reduce system cost.

However, there are several pieces of equipment that can only be ordered with the SMA connector standard. These interface with our FC connector equipment via FC-to-SMA patchcords.

3.3.5 Fiber Coupled Diffusers

The obvious choice for light delivery tip for our applications are fiber coupled cylindrical diffusers. The goal is to illuminate the prostate as evenly as practically possible with minimal collateral illumination. Because flat cleave fibers and fibers terminated with micro lenses have highly directional output with hot spots near the tip, they fail at delivering an isometric light dose, and at the same time risk thermal induced tissue damage at the hot spots. Well made spherical diffusers offers the possibility of near isometric output; however, it is difficult to create approximate isometry with point sources in a 3D space. Many point sources would be necessary in 3 dimensions precisely

positioned throughout the volume. Extending isometric point sources out in one dimension into isometric linear sources reduces one degree of freedom and improves isometry along that dimension. While multiple diffusers are still necessary to improve isometry within the target volume, isometry is improved over point sources. Extending to linear sources do not place extra surgical burden or physiological burden on the patient compared to spherical sources because both would require the same linear access pathway. Therefore, it is more optimal to choose linear diffusive sources. Extending to higher dimensions are both difficult engineering wise in terms of creating such a diffusive source, as well as impractical medically. It would increase surgical complexity as well as increase invasiveness of procedure. The most practical fiber coupled linear diffusive sources are cylindrical diffusers.

There are three fiber coupled cylindrical diffuser manufacturers that were examined: MedLite (Switzerland), Polymicro Technologies (USA), and Walsh Medical Devices (Canada). Comparing light transmission, Polymicro Technologies had the highest throughput, followed closely by Walsh Medical Devices and a distant third at approximately 30% lower was MedLite. There are two properties highly desirable properties for a linear (cylindrical) diffuser. One is that the light output is omnidirectional. That is, at every point on the linear diffuser, it radiates light equally in all directions. The second property is that the light output is equal in power at all points along the diffuser. The Polymicro Technologies diffusers were made from laser etched glass and clearly showed directional output biased towards the tip of the diffuser. Examining along the length of the diffuser, there was also greater light towards the tip of the diffuser. Both problems could be easily identified with the naked eye; therefore, although the cheapest of the three, Polymicro Technologies diffusers were dismissed immediately. MedLite

diffusers were contained in a white polymer sheath which helped in improve scattering. However, the diffuser tip has a 2 mm non-diffusing section. This would result in the need to puncture through the target volume by 2 mm and is undesirable. These diffusers also are not made with the FC connector standard and the manufacturer stated that the diffusers will not work if they were reconnectorized them into FC connectors due to their proprietary technology near the connector end to improve diffusion. Additionally, the diffusers contained more autofluorescence than WALSH MEDICAL DEVICES diffusers (See figure 3.17). Table 3.1 summarizes the comparison of basic diffuser properties between the three manufacturers. Linear diffusers from WALSH MEDICAL DEVICES had acceptable emission profile and, although delicate, was chosen out of the three by process of elimination.

Note that afterloading needles (ALN) (Flexineedles with obturator and cap, BEST MEDICAL INTERNATIONAL, USA) similar to the ones commonly used for brachytherapy were used to prevent non-sterilized cylindrical diffusers from direct contact with tissue. They also serve as protection for the diffusers as well as additional scattering. We chose 15 and 18 gauge ALN. In practice, we found that while 18 guage ALN were much easier to insert and use for rat experiments, the limited access of canine prostate resulted in much higher forced insertions causing the 18 gauge needles to bend. 15 gauge needles were used upon this discovery.

Measured emission profile of the WALSH MEDICAL DEVICES 15 mm linear diffusers is shown in figure 3.4. A distinct cut-off is not present as the ALN cavity is wider than the diffuser radius allowing for light to reach beyond the 15 mm diffuser length. Note that the ALN has a solid tip with low light penetration. This makes the extra 2 mm non-diffusing section of MEDLITE diffusers even

	Walsh Medical Devices	MedLite	Polymicro Technologies
Relative Transmission (normalized to highest diffuser)	0.98	0.72	1
Omnidirectional Output	Good	Good	Poor
Uniformity Along Diffuser	Good	Good	Poor
Autofluorescence Noise	Yes	Yes	N/A
FC Compatibility	Yes	No	N/A
Ease of Handling	Poor (diffusers are very delicate)	Good	N/A
Relative Cost (normalized to highest cost)	0.6	1	N/A
Others		Extra 2 mm opaque section on tip of diffuser	

Table 3.1: Summary of basic diffuser properties between the three cylindrical diffuser manufacturers.

more undesirable. More information on Walsh Medical Devices linear diffusers can be found in Vesselov[65] and Lilge[66].

3.3.6 Template

For precise and repeatable *in vivo* positioning of diffusers, a template is use for guidance. 15 and 18 gauge templates were designed in AutoCAD for use with the two sizes of ALN (Figure 3.5). The 10 mm thick templates are made out of clear plastic and precision drilled such that the ALN can slide in easily but with just enough friction to hold the ALN's own weight. The hole spacing is designed as close as possible to allow for the most flexibility in terms of matching holes to dimensions of treatment volume; however, the structural integrity of the plastic must be considered. An older template made of the same material suffered structural failure from too many holes. Screw threading were also drilled into the side of the templates to allow for mounting. These templates are for use with 7 fibers but may accommodate more if needed. In a 7 fiber configuration, 1 is at the center and 6 are at outer positions in a hexagonal pattern. The location depends on the size and shape of the treatment volume.

3.3.7 Optical Filter

Ocean Optics FHS-UV filter stations were used to hold in-line optical filters. Various filters of less than 25 mm diameter and 6 mm thick can be accommodated. Multiple thinner filters can be stacked. Each FHS-UV is equipped with a pair of 74-UV collimating lenses to maximize throughput. Varying thicknesses of 665 and 645 nm long pass filters (RG665 and RG645

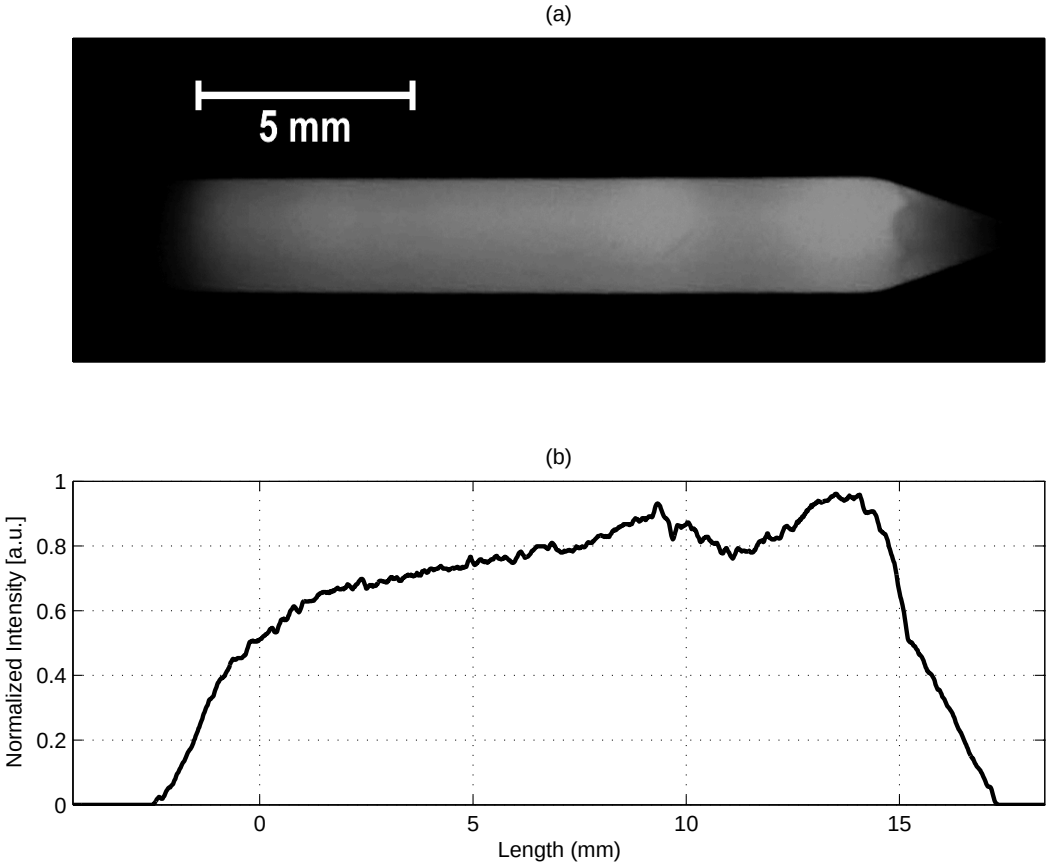

Figure 3.4: Walsh Medical Devices cylindrical diffuser emission (a) image and (b) profile in 15 gauge afterloading needle.

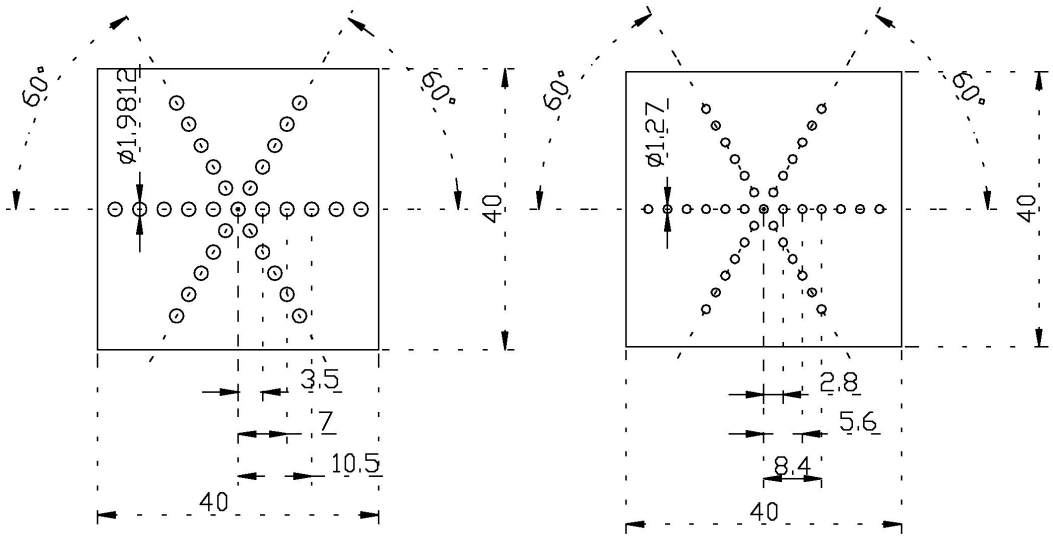

(a) (b)

Figure 3.5: Engineering diagrams of diffuser position templates (a) for 15 gauge ALN and (b) for 18 gauge ALN. Measurements are in millimeters. The templates are made out of clear plastic and are 10 mm thick.

Optical density of RG filters at respective wavelengths	635 nm (OD)	815 nm (OD)
2 mm RG645	0.68	0.049
3 mm RG645	1.2	0.053
2 mm RG665	4.2	0.050

Table 3.2: Measured filter attenuation for RG filters at SL-052 excitation and fluorescence wavelengths.

respectively) are used in combination during iPDT. When necessary, a 635 nm bandpass filter ($635/10x$) is also used to clean up the laser line. Filters are obtained from Chroma Technology Corp (Rockingham, USA).

Figure 3.6 shows the filter profile of 2 mm of RG665 calculated by measuring filtered and unfiltered signals from a broadband light source ($40W$ incandescent light bulb). Note that the transition is not very sharp, spanning over approximately 50 nm. Table 3.2 gives measured filter attenuation for RG filters at SL-052 excitation and fluorescence wavelengths. This data will be used in discussions and applied in calculations later on.

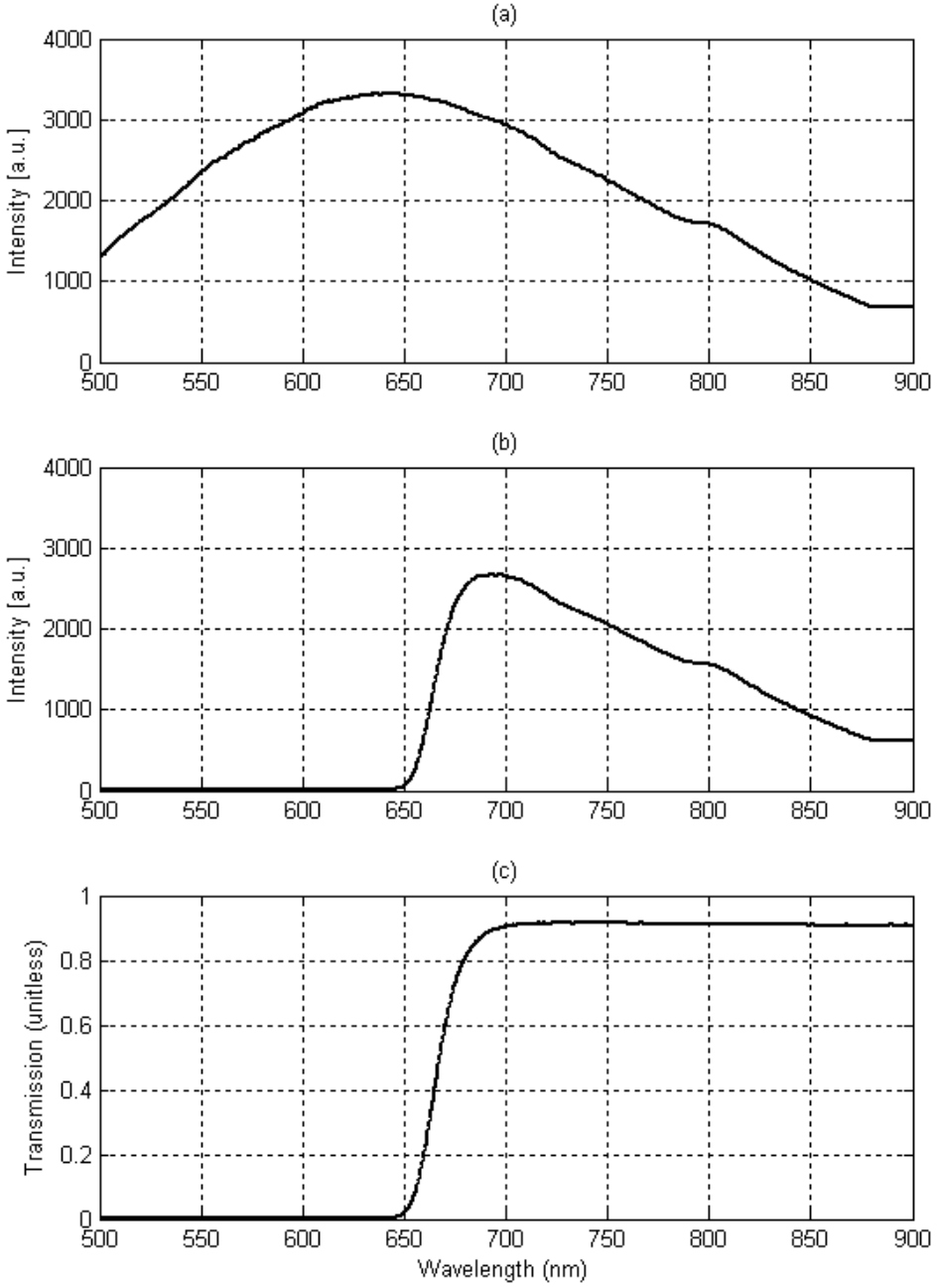

Figure 3.6: Filter profiling using broadband incandescent light source showing (a) the unfiltered spectrum, (b) the filtered spectrum, and (c) the obtained filter profile.

3.4 System Integration and Operation

3.4.1 Layout

Figure 3.7 shows the layout of the light delivery and detection system. For the light delivery component, the two 7404 diode lasers are fed into two different 3×9 modules on the mechanical switch. Module 1 is connected to 4 fiber coupled diffusers corresponding to the center position and 3 outer positions on the template while module 2 is connected to 3 fiber coupled diffusers corresponding to the remaining 3 outer positions on the template. This allows for the switched light delivery pattern described in section 3.4.2. The setup can be easily expanded to accommodate up to 18 light delivery fibers. The optical switch is connected and controlled by laptop via GPIB (IEEE-488) interface. All diffusers are contained within ALN's in the volume such that they made no direct contact with tissue.

For the light detection component, the integrating sphere can be used to detect intensity of excitation light by light fed back through the diffusers and through the switch. This is done when one module is switched to the laser and deliveries light while the other is set to the integrating sphere and detects light. Multiple fibers can be fed into the input of the integrating sphere which allows for both modules to be connected to it at the same time. The integrating sphere is controlled by the laptop and detected light power is automatically recorded.

The USB2000 spectrometer captures spectral information during iPDT. Currently, it is setup such that an eighth fiber is inserted between the center fiber and one of the outer fibers, also within an ALN. This collection fiber is a 600 μm custom made flat cleave Ocean Optics fiber. Between the collection fiber and the spectrometer is the FHS-UV in-line filter station. Long pass

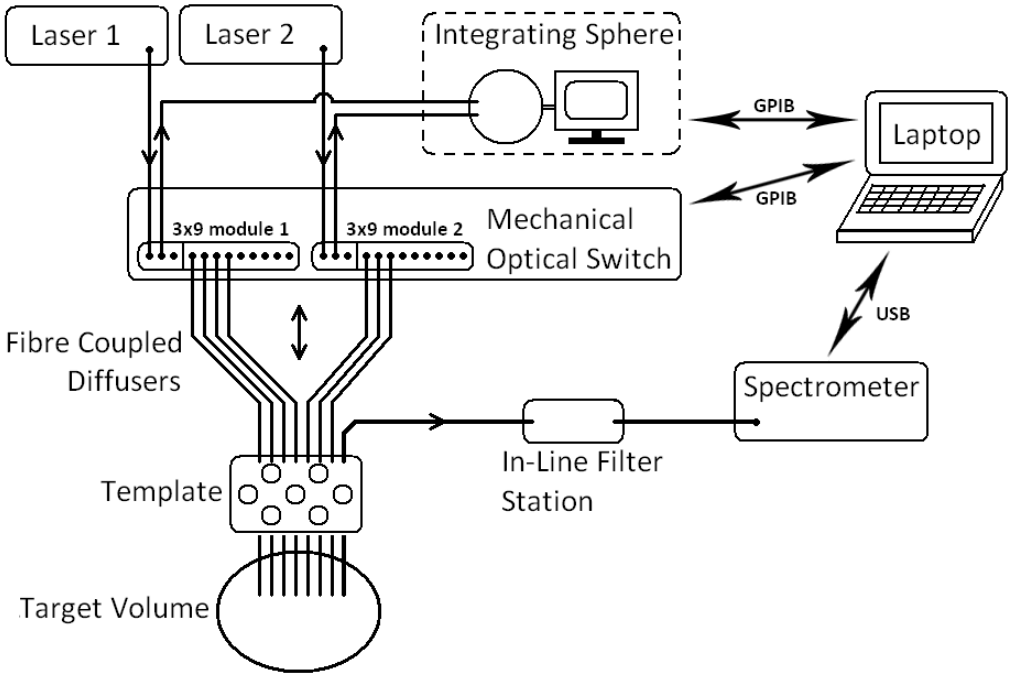

Figure 3.7: iPDT light delivery and detection schematic

filters are used to attenuate the 635 nm light such that it does not saturate the spectrometer when 815 nm SL-052 fluorescence is being measured. The detected 635 nm excitation intensity is much stronger than fluorescence so filters must be used. Figure 3.8 is a photo taken of the experimental setup during iPDT of the canine model.

3.4.2 Switched Light Delivery and Detection

Interstitial PDT of canine is carried out with the switch setup for a 7 fiber setup (Figure 3.9). Each diffuser is switched between a 90s or 100s, depending on the setup, light active state and 300s dark state. Figure 3.10 shows the switch timings for configurations with or without the integrating sphere detection. Light active states for the outer diffusers are set such that only opposing pairs in the hexagonal shape will be active together so that the active diffusers

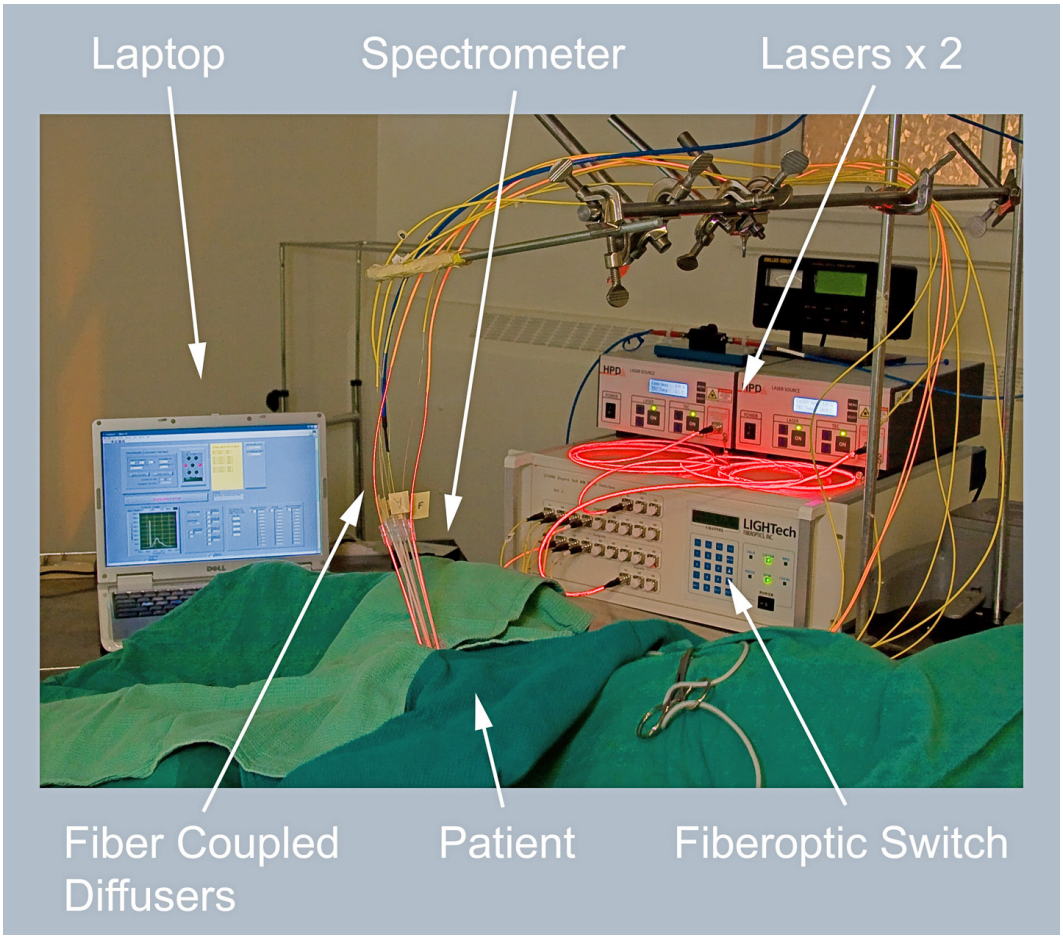

Figure 3.8: Illustrative photo of setup during canine iPDT.

have maximum distance between each other. This maximizes the tissue re-oxygenation time and should improve the effectiveness of time-fractionation. When the center fiber is active, the other 6 are dark. Before light delivery, power check is performed for each fiber to ensure uniformity and to dial in the desired power settings. Due to the nature of fiber optics, optical switch alignment errors as well as diffuser manufacturing can easily lead to small differences in output power between diffusers. Deviations less than 10% of the mean was considered acceptable.

For integrating sphere light detection, the fiber coupled diffusers for excitation light delivery doubles as light collectors. When the middle fiber is delivering light, the 3 outer fibers on the opposite module are switched in turn to detect light. For each outer fiber that is delivering light, a neighboring fiber on the opposite module is used to detect light. Since this detected light is unfiltered, it will be dominated by light from the excitation source. Background and fluorescence sources are assumed to be negligible. This detected light will be used to track changes in tissue transmissivity at the excitation wavelength assuming the laser power does not significantly change. One data point (three for center fiber) is captured per fiber per cycle.

Because both the drug and the drug delivery protocol are novel, the spectrometer's initial purpose was to check for SL-052 fluorescence to confirm the presence of drug in the target tissue. In order to detect fluorescence, long pass filters had to be employed to attenuate the excitation light such that 635 nm would not saturate the spectrometer. Filter combinations were used such that the 635 nm peak signal magnitude would be attenuated to similar levels as the fluorescence peak signal magnitude. This allowed us to not only use the spectrometer as a fluorescence monitor, but also an excitation light

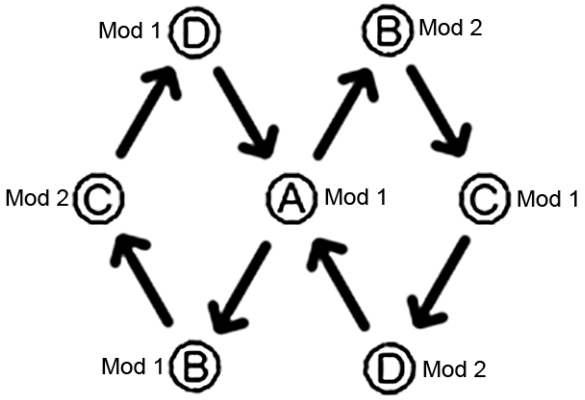

Figure 3.9: Hexagonal layout of treatment fibers. Switched light delivery begins at fiber A, switches to fiber set B, then C, followed by D, and cycle repeats back to A. The outer fibers are connected in alternating modules (i.e. B, C and D alternate between Mod 1 and 2) and each pair (e.g. B's) are on opposite modules.

monitor. During the first iteration of this iPDT system, one spectrum is manually captured per 100s sub-cycle using SpectraSuite (Ocean Optics). Because our initial interest was the overall change of 635 nm and fluorescence signals, one data point per sub-cycle was sufficient. Upon investigation of results, (chapter 4), we found that the spectrometer obtained better signals for excitation light monitoring than the integrating sphere. In addition, unlike the integrating sphere detection where fibers had to be used for delivery as well as detection, employing the eighth detection fiber for the spectrometer means the fiber is used solely for light detection and can monitor the treatment continuously. As the operator, I noticed significant changes in both detected excitation and fluorescence signals within each 100s sub-cycle. This meant signal intensities for the capture for each sub-cycle was dependent upon the time of capture within that sub-cycle. I quickly changed the capturing protocol such that each manual spectrometer capture occurred at relatively the same time within each sub-cycle. Because the intra-sub-cycle changes were faster

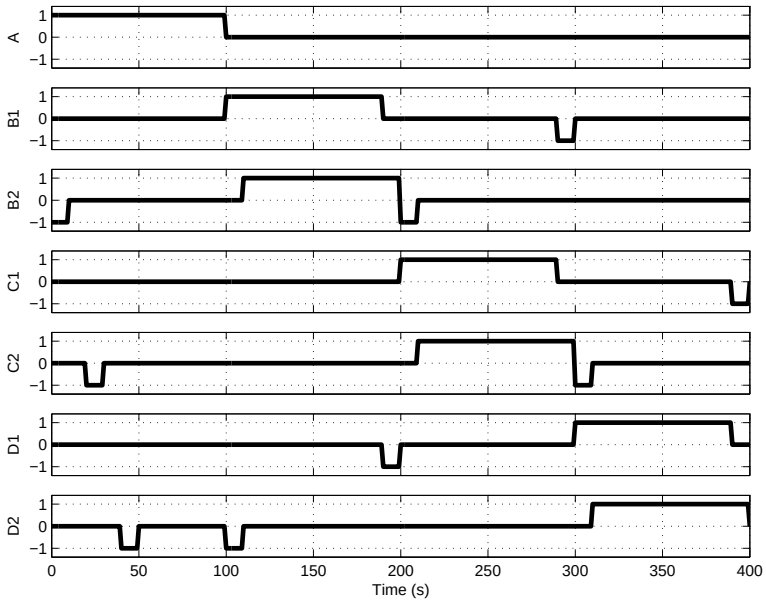

(a) With Integrating Sphere Detection

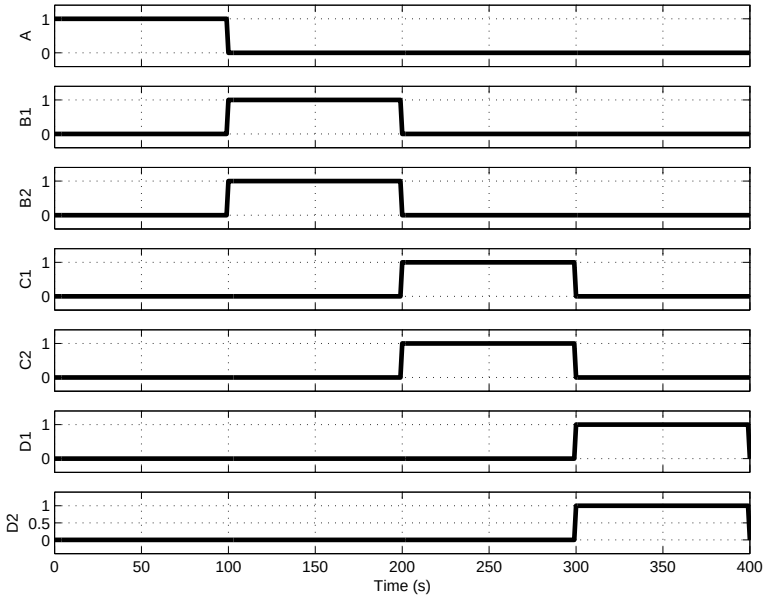

(b) Without Integrating Sphere Detection

Figure 3.10: Timing diagrams for fiber optic switch operation for (a) with integrating sphere light detection and (b) without integrating sphere light detection. State 0 represents the inactive state for the fiber coupled diffuser, 1 represents when it is delivering excitation light, and -1 represents when it is functioning as a light collector for the integrating sphere.

at the beginning of each sub-cycle and much slower near the end, the manual captures occurred close to the end of each sub-cycle.

With the most recent iteration of this iPDT system, the spectrometer capture has been completely automated. All settings including integrating time, averaging, and dark spectrum subtraction was automatically controlled by the control software developed in LabVIEW (Section 3.4.3). Time stamp was tagged along with each spectral capture at a capturing rate of up to 1 spectrum per 5 seconds (practical limitation). This captured never before seen sub-cycle signal oscillations discussed in Chapter 4. With this iteration, the integrating sphere detection was removed (Figure 3.10b) and excitation light detection is fully replaced by the spectrometer. This resulted in a full 100s light per fiber for each 100s sub-cycle rather than 90s per 100s sub-cycle and reduced total treatment duration.

3.4.3 Software

Overall control software was built in its entirety in LabVIEW (National Instruments, USA). LabVIEW is chosen for its:

1. Ability to interface easily with multiple I/O's.
2. Easy timing control with execution of multiple loops in parallel.
3. Graphical user interface (GUI) support for front panel to allow for operation by non-technical personnel.
4. Ability to generate of stand alone code for export of our control system in a business setting.

5. Excellent global support such that LabVIEW subroutines OEM hardware are available.

The software font panel controls is shown in figure 3.11. The operator only needs to input the dimensions of the treatment volume, the average power at the diffusers, and the desired volumetric light dose. Alternatively, the operator may simply input the desired number of cycles, or the desired total treatment time and the code will round down to the closest total time with complete cycles. The time per fiber defaults to 100s and remains as such for all of our experiments, but the code does allow that to be changed as well. A switch reset can be used to put the switch into a known state and begin treatment will initiate the treatment once all fibers are in position. The indicator lights to the right represents each fiber and will turn *red* if that fiber is lasing, or *green* if that fiber is being used for integrating sphere light detection. That status indicator can update the operator as to the stage of current operation. Below is a graph that gives spectra captured in real-time. The remaining fields to the right of that are for file naming purposes when the software auto-saves captured data. The emergency stop button will immediately terminate light delivery.

In order for the code to be easily modified and transferable, it is built with a main wrapper program and various modules, each module responsible for a device or function. The main wrapper program simply calls these devices and functions in the correct order and with timing considerations. It is also responsible for array initializations. A screen capture of the wrapper program is shown in figure 3.12. The wrapper is the main code that calls upon other subroutines to complete the tasks of the full program software.

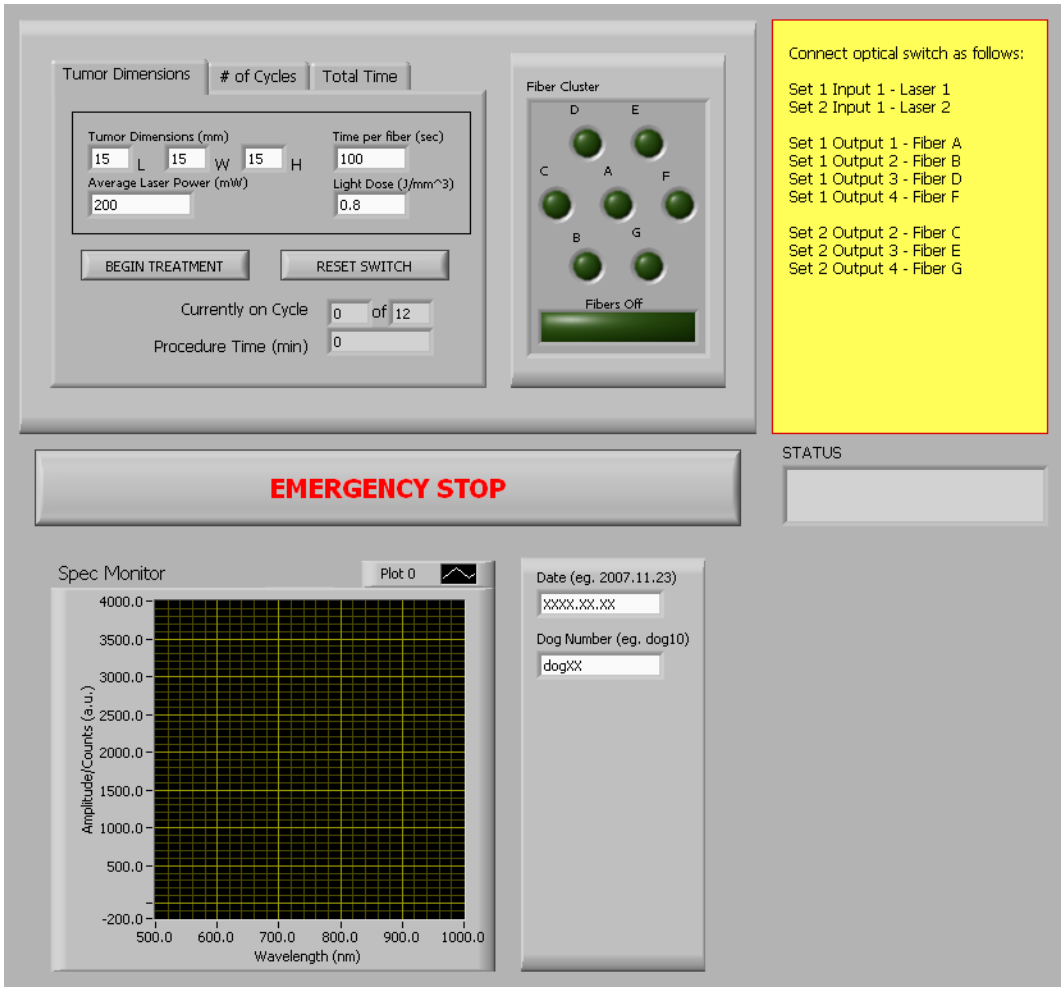

Figure 3.11: The front panel GUI for the overall control software.

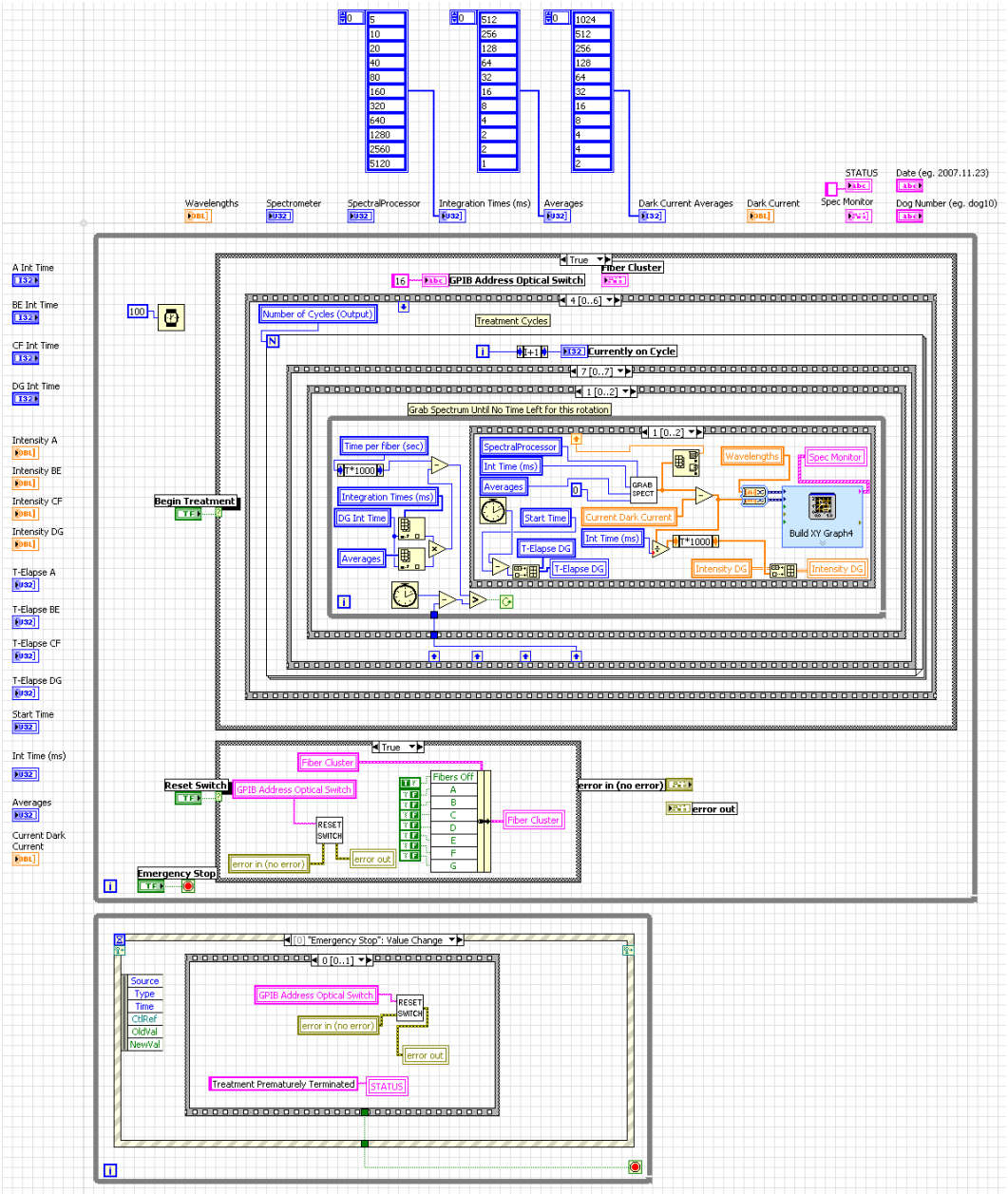

Figure 3.12: Sample screen capture of the LabVIEW block diagram for the control software's main wrapper code.

Because the system is meant to be used in a clinical setting, any glitch or failure could result in serious consequences for the patients' well being or result in a costly wasted experiment. Therefore, various software redundancies for the modules are built in to attain in-field robustness of operation, especially during fully automated delivery and detection. For optical switch control modules, each switch command is followed by a switch confirmation command to ensure that the switch command has registered and that it has mechanically moved to the proper channels. Because the switch is a mechanical device and travel by car is required between lab and surgical facility, this extra software check ensures that critical device components have not been rendered stuck, or if it has, will immediately warn the operator. The integrating sphere has been known to report false data if insufficient time has been given to allow its auto-range to properly detect the signal strength/range. Software is designed such that sufficient time is given to the integrating sphere even in the worst case scenario. This ensures the accuracy and reliability of our experimental data. For the automated spectrometer detection modules, there is concern that during auto-acquisition when the signal is changing, the integrating time interval might not be set appropriately. Modules were used to control the integration time interval and number of averages such that the data rate is at an acceptable level and the output data range is not clipped. Dark current subtraction is also automatically applied. Again, these procedures help to ensure the accuracy and reliability of experimental results. One thing that the software does not check throughout the experiment is laser power; however, we have found that the laser modules perform with enough stability for our applications (see Section 3.3.1). As a safety precaution, the emergency stop button is available to immediately break the code out of any loops or wait commands, shut off any fibers from delivering light, and stop all operations.

Data that have been captured up to that point is not lost.

3.4.4 Detector Noise Considerations

There are numerous possible sources of noise for spectrometer detected signal. We have already covered the laser output noise in terms of stability over time of the laser modules in section 3.3.1. The less than 1% long term fluctuation in laser output is small compared to other sources of noise and is considered negligible on the detection side. However, on the time scale of a few milliseconds, laser stability may be questionable. When input signal is strong enough such that the appropriate integration time of the spectrometer is around the range of 5 ms or less, the laser line, as well as other laser induced spectra, become noticeably unstable, fluctuating upwards of 5% of measured counts. I found that by applying averaging over multiple acquisitions this noise is greatly reduced. For total acquisition time (integration time multiplied by number of averages) greater than 400 ms, the fluctuation magnitude from this phenomenon is much less than 1% of detected counts. At higher integration times, such phenomenon is not observed since increasing integration time reduces this type of noise in the same way averaging does.

The spectrometer itself generates dark signals. When all light sources are removed, there is a base level of signal across the entire spectrum. The average level is approximately 160 to 300 counts out of a range of 4096 counts for typical operational ranges of integration time (3ms - 5000ms). Ocean Optics has programed in specific dark current removal tools for using the spectrometer and when enabled, it subtracts a given number across the entire spectrum. While this removes the base level, it is not the most optimal method. At integration times of greater than 1000 ms, significant systematic noise appear in

the collected spectrum capture of a smooth broadband source (60W incandescent bulb). The noise does not decrease with averaging and is therefore not random noise. Because the spectrometer's sensor is CCD (Charge Coupled Device) based, there may be fabrication differences in each of the CCD photosites. This may result in different levels of leakage current at each photo site and be a source of systematic noise. I found that a manual subtraction of dark current, that is, make a capture at the zero light case then subtract it from the signal, was not only good at removing the base level of dark current, but also excellent at removing this systematic noise. Figure 3.13 shows the before and after effects of my dark current subtraction versus Ocean Optics's automatic subtraction. The specific improvement of signal-to-noise ratio using the manual subtraction method will mainly depend on the integration time used as well as the signal being detected. For the purpose of this thesis, spectrometer data is collected in a method such that both averaging and manual dark current subtraction is applied.

3.4.5 Spectral Noise Considerations

For concurrent detection of iPDT excitation light and SL-052 fluorescence light, the excitation light must be attenuated significantly such that both spectral characteristics fit within the dynamic range of the spectrometer. That is, a filter must be used to attenuate the 635 nm down to approximately the same order of magnitude as the fluorescence signal. Depending on the concentration of SL-052, the separation distance between source and detector, and the medium of light transmission, different amounts of 635 nm attenuation must be applied. When the fluorescence signal is weak, a longer integration time is necessary. This in turn would reveal other undesirable spectral features which

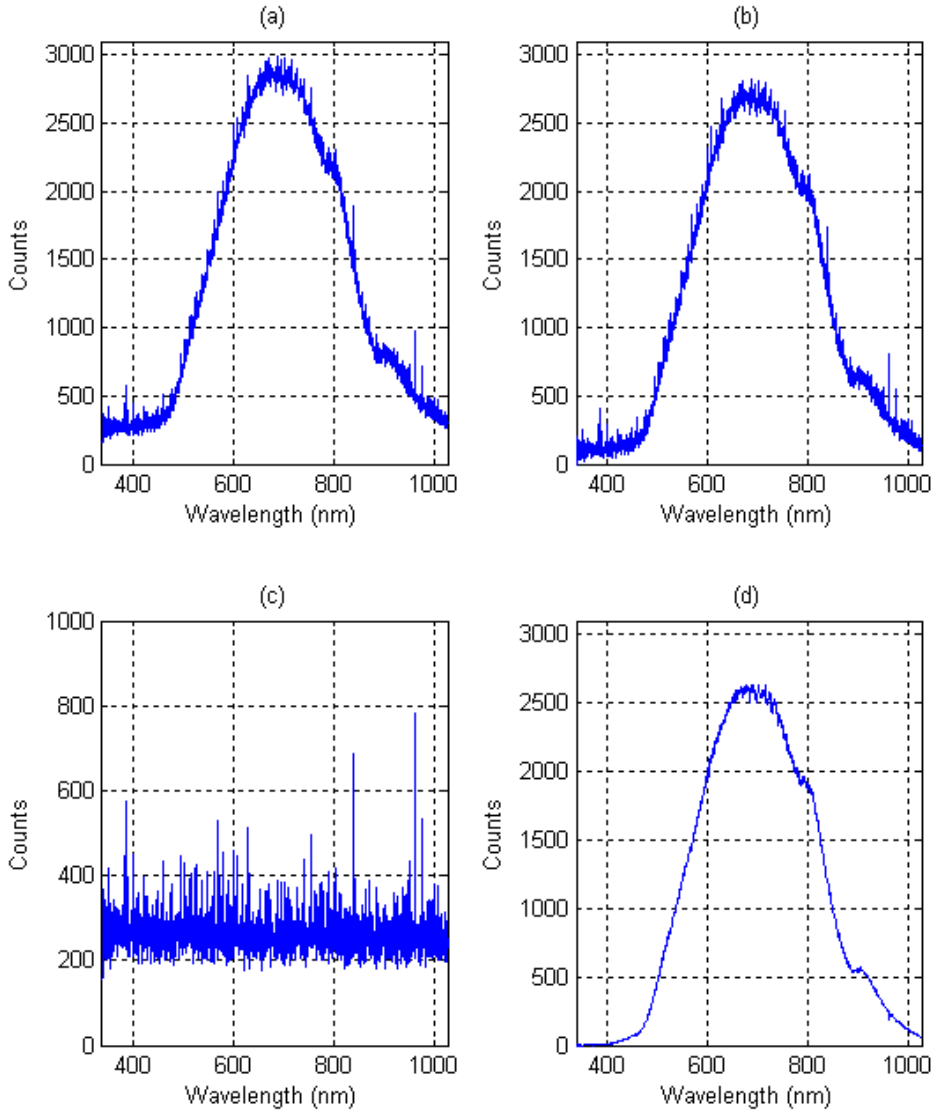

Figure 3.13: Spectrometer Noise Subtraction. (a) Raw noisy spectrum of a smooth broadband source including the base level of dark current. (b) Result with Ocean Optics's dark current subtraction. (c) Manually captured dark current at the same integration time as previous captures. It is captured with a closed shutter in front of the spectrometer. (d) Result of manual subtraction showing much less noise than Ocean Optics dark current subtraction. Averaging did not noticeably improve the noise in any of these captures.

I am labeling as spectral noise. This would be similar to large amplification of a weak signal revealing underlying noise sources. There are two main sources of spectra noise that are detectable during normal operations: laser noise and diffuser autofluorescence.

3.4.5.1 Laser Noise

Figure 3.14 outlines the laser noise situation. When 635 nm laser line is attenuated by approximately 42dB (2 mm RG665 at detector) a wide laser noise profile is apparent. When a $635/10x$ bandpass filter (bandwidth 10 nm centered about 635 nm) is used at the output of the laser to clean up the laser signal, the noise disappears. Please note that this spectral noise is not detectable when laser line is completely unfiltered (no RG665 or $635/10x$) due to the high signal-to-noise ratio causing the noise to be not visible on the same scale as the unattenuated laser line.

In figure 3.14(a), the laser noise appears to peak near 664 nm; however, this would be incorrect. The false peak is a result of a wide spontaneously emitted laser noise profile being cut off by the RG665 filter which has a filter transition at 665 nm (Figure 3.15). Monitoring laser output from pre-threshold injection current through to normal operating currents shows the noise exists pre-threshold and increases as injection current increases. However, the increase in noise power compared to increase in total laser power seem to behave logarithmically (Figure 3.16). As injection current increases, much more of the power goes into the lasing mode rather than the noise.

Such a broad noise profile which exists pre-threshold (but does not exist at zero injection current), suggests that it is spontaneous emission from the excited laser diode. There is also a spatial dependence on this spectral noise. If θ

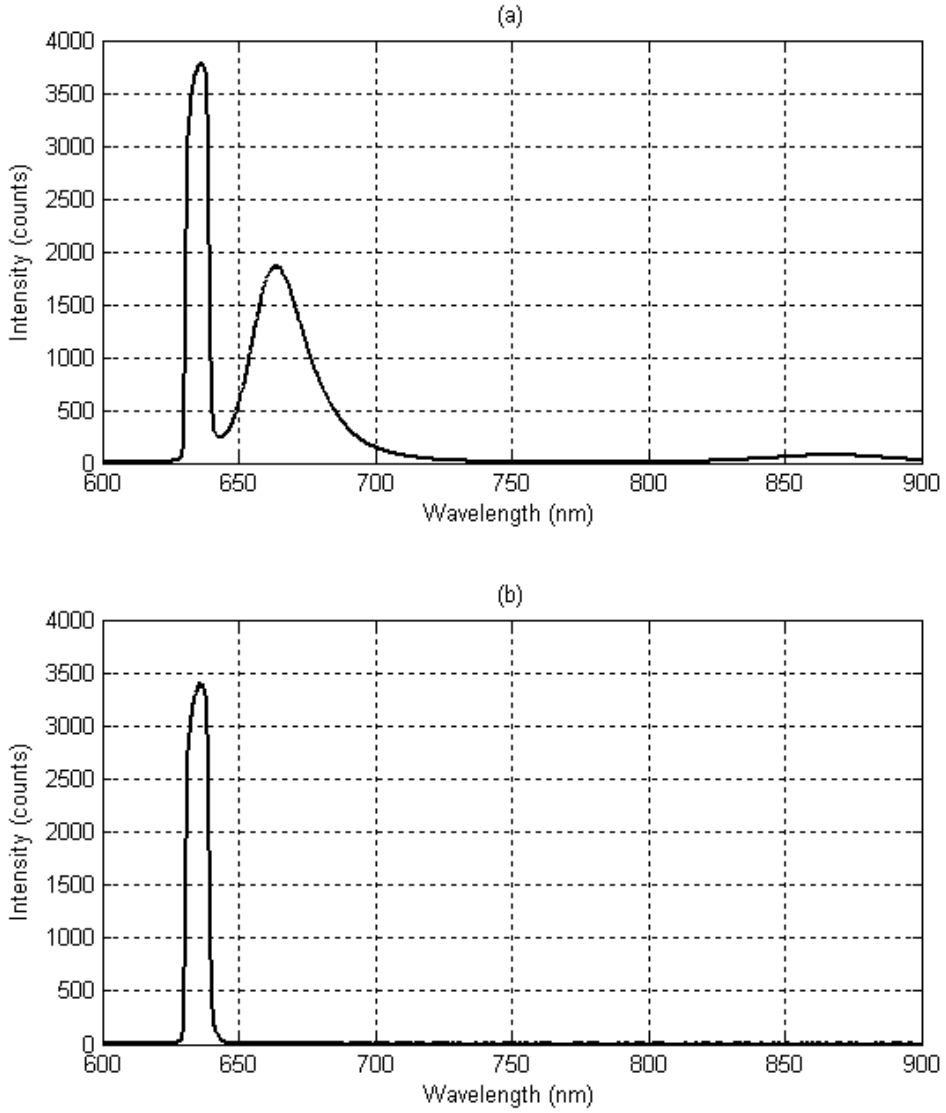

Figure 3.14: (a) Laser spectral noise is visible when laser line is attenuated by approximately 42dB (2 mm RG665). (b) When a $635/10x$ bandpass filter (bandwidth 10 nm centered about 635 nm) is used at the output of the laser to clean up the laser signal, the noise disappears.

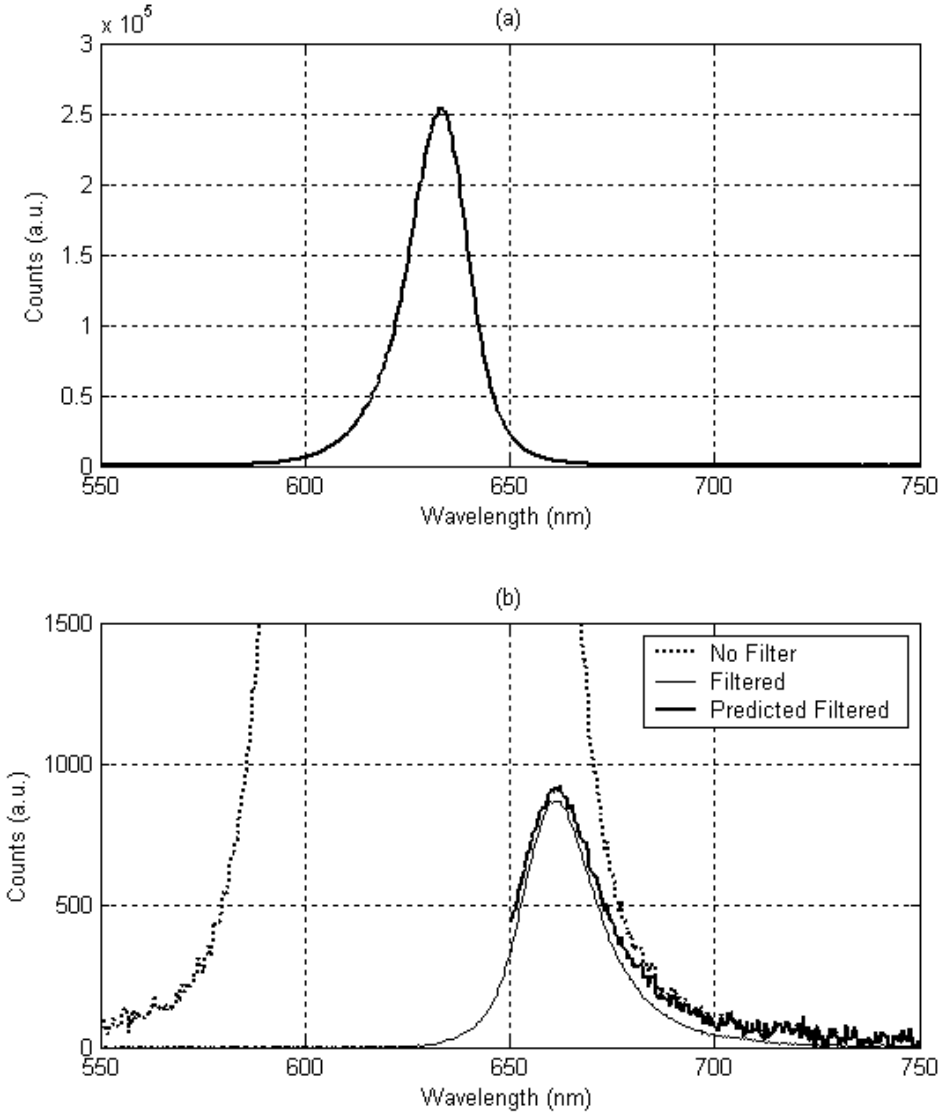

Figure 3.15: Pre-threshold laser noise showing (a) the unfiltered noise and (b) the noise profile with RG665 filter. The predicted filtered line is composed of the non-filtered line multiplied by an independently measured filter profile to show that the result is very similar to the filtered profile. This ensures that the noise peak near 664 nm of RG665 filtered spectrum is indeed a result of filter attenuation of a much broader noise profile.

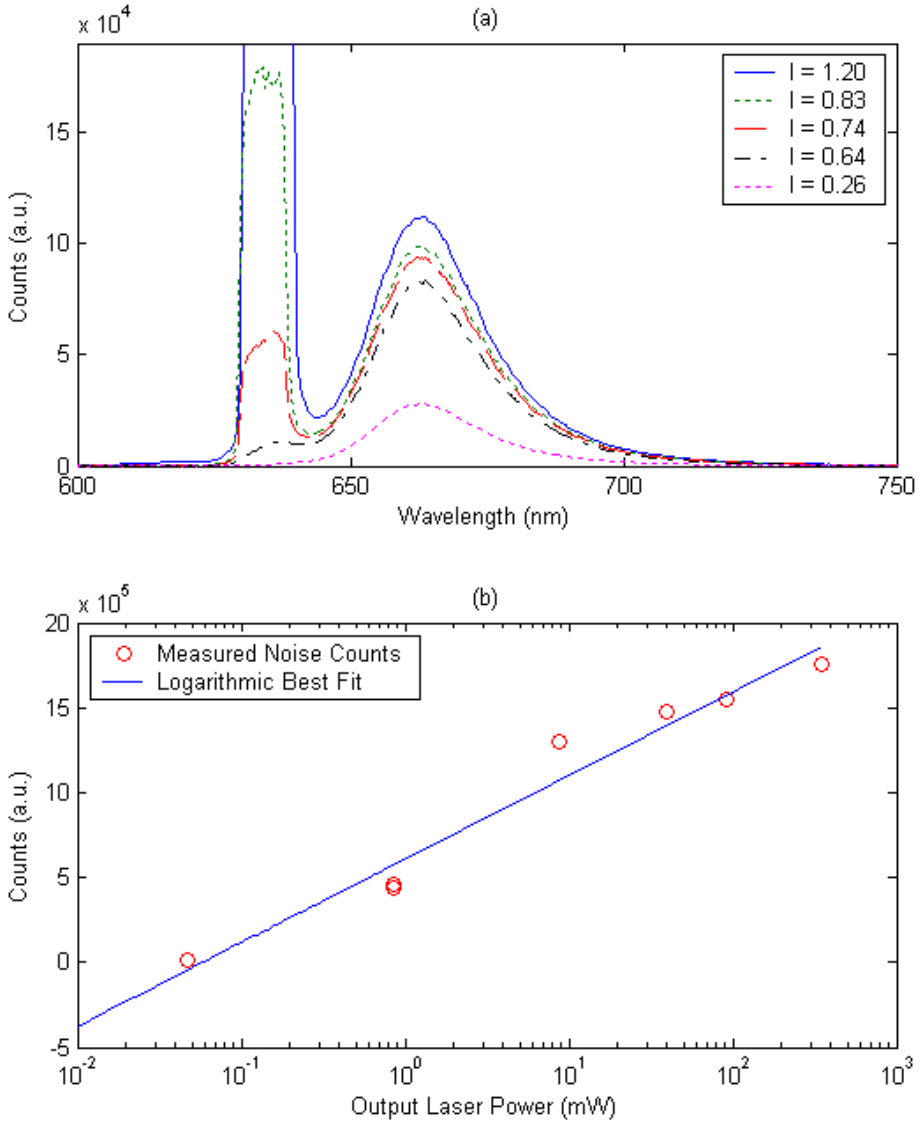

Figure 3.16: Comparison of laser spectral noise with respect to output power. (a) Profile of 635 *nm* laser line and noise with RG665 filter. As laser diode injection current increases, noise profile also increases without changing shape. (b) Noise power increases logarithmically compared to total laser power. The noise counts is a summation across the peak of the noise while output laser power is full unfiltered laser power measured directly from a power meter.

is the angle of the cone of light leaving the output fiber, then when laser output is measured at a high θ, signal-to-noise ratio (SNR) goes down. That is, this noise is less collimated than the 635 nm emission which we would expect if the noise is spontaneous emission. The manufacturer (HIGH POWER DEVICES) also confirmed that the noise is spontaneous noise when I presented this evidence to them.

While figure 3.14 shows that the laser noise can be cleaned up with a $635/10x$ bandpass filter, such filtration is not necessary for our applications because the noise does not extend to regions where fluorescence is measured (815 nm). See figure 3.17(c). The in-line filter station necessary to hold the $635/10x$ filter also greatly reduces light throughput reducing output power by approximately 30%. Therefore, it is beneficial to not use the bandpass filter for clean up of laser spectral noise.

3.4.5.2 Diffuser Noise

The autofluorescence noise generated by diffusers is exemplified in figure 3.17. The data is captured with the $635/10x$ (unless otherwise specified) to ensure a clean laser line enters the diffusers. This isolates the source of this spectral noise to the diffuser itself. The MEDLITE diffusers showed slightly more fluorescence than our chosen WALSH MEDICAL DEVICES diffusers. Adding an ALN to the outside of the diffuser does not change the spectral noise. When the laser spectral noise is allowed to pass through (i.e. $635/10x$ is removed), the noise profile only increases at wavelengths below 800 nm, and therefore the laser noise does not significantly contribute to 815 nm background when measuring fluorescence. The autofluorescence of diffusers causing a background at 815 nm is a significant source of noise for fluorescence measurements as we

shall see in Chapter 4.

3.4.6 Losses in Optical Power

Optical power losses through connectors are quite significant for our system. Power losses through the entire system (laser aperture to diffuser output) was less than 1.6dB (31% loss) when equipment was new. However, current power losses are up to 2.5dB (44% loss). The in-line optical filter station with $635/10x$ laser line cleanup filter has an additional 2.2dB loss (40% loss). Fortunately, the $635/10x$ is not necessary for iPDT operation.

3.4.7 Practical and Engineering Considerations

There are several practical and engineering considerations that must be taken into account for the use of this iPDT system.

1. Portability - For marketability and practical reasons, it is desirable for the system to be easily transportable between operating rooms or between hospitals. Currently, the system fits on a small $2' \times 4'$ push cart for transportation between operating rooms, or fits in a compact vehicle for transportation between hospitals. Once on location, setup time and clean up time takes less than one hour to complete including equipment and power checks. For future considerations, the entire system may be rack mounted for robustness and improved setup and clean up time.

2. Adaptability for other photosensitizers - One major difference with utilizing other photosensitizers is the need for a secondary laser source for detecting light induced fluorescence. However, our optical switch was

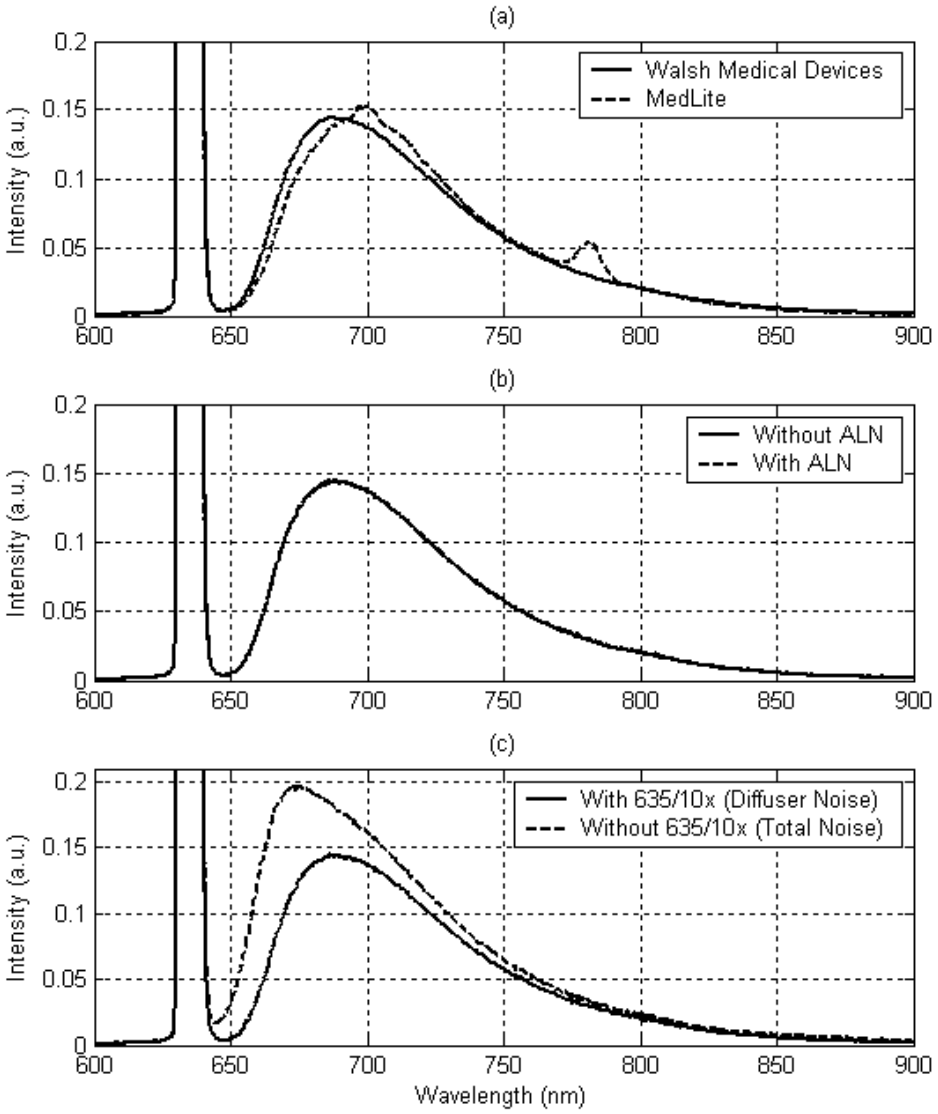

Figure 3.17: Walsh Medical Devices Cylindrical diffuser autofluorescence noise. All data except the dashed line in (c) has been taken with the $635/10x$ laser line clean up filter so that only diffuser autofluorescence remains. (a) A comparison between Walsh Medical Devices and MedLite diffusers showing slightly higher autofluorescence with the MedLite diffuser. No afterloading needle (ALN) used. (b) A comparison between diffuser with and without ALN. The two profiles are nearly identical meaning that the ALN does not significantly fluoresce. (c) A comparison of total noise (laser + diffuser) and diffuser noise showing that the laser noise only significantly adds to the diffuser noise at wavelengths less than 800 nm. Therefore, the laser line cleanup filter ($635/10x$) is not necessary because fluorescence is obtained at 815 nm. Note, the excitation source strength has been normalized to 1.

constructed to allow for the that flexibility by adding the extra input port for each stitch module to allow for a secondary wavelength source.

3. Spectrometer connected to switch - A possible future consideration could to be attach the spectrometer directly to the fiberoptic switch eliminating the need for the extra detection fiber. It may function as a detector in a time sequence similar to the time slots the integrating sphere utilized for detection. However, this would in non-continuous detection.

4. Diffuser breakage - There were several circumstances which we noticed the diffusive coating on the WALSH MEDICAL DEVICES cylindrical diffusers were breaking off during canine testing. I tracked the reason down to the stress placed on the ALN's during insertion into canine prostate for 18 gauge needles. The insertion method caused the ALN's to bend even when obturator was present. When the cylindrical diffusers were inserted through the bend, the brittle coating would sometimes break off. The problem was discovered and alleviated by switching to the 15 gauge needles which contained a stronger obturator as well as large inner diameter for diffuser to slip through. Before human testing or testing in other models, it is important to consider the amount of flex in the ALN's to ensure diffusers do not break upon entry.

5. Capture rate limit - The data capture rate limit was programmed to be a maximum of 1 spectrum per 5 seconds. This was a practical limit due to available memory in current day computer setups for treatments over several hours. The equipment is well capable of much higher data rates. There are solutions to the computer memory issue, but 5 second refresh rate is assumed to be fast enough for optical changes during iPDT.

6. Code robustness - As previously mentioned, the system is meant to be

used in a clinical which glitches may result in serious consequences. Software has been built with various redundancies to ensure smooth operation. Such fail safe procedures should be also implemented in future systems to attain a reliable and in-field robust system.

3.5 *In vitro* Hardware Testing and Operational Considerations

3.5.1 Optical Response *in vitro*

Using the intralipid phantom mixture from section 2.3.2 with optical properties similar to that of canine prostates, the optical response of the iPDT system was tested at varying photosensitizer concentrations and varying source-detector distances for the cylindrical diffusers that are used for canine experiments. Due to limited availability of SL-052 from QUEST PHARMATECH, the varying concentrations of photosensitizer was modeled with a substitute absorber matching the absorption coefficient of SL-052 at the excitation wavelength of 635 nm with the assumption that at treatment concentrations, SL-052 has negligible scattering coefficient compared to that of the canine prostate. The optical response of interest is the transmission of excitation light, or more specifically, the measured 635 nm intensity at the detector. The fluorescence response could not be measured in this experiment as methylene blue does not have similar fluorescence characteristics as SL-052. Using the exact same setup as canine experiments, results from this assay could serve as a look up table for local SL-052 concentration when the transmission intensity and separation distance are known. Such data could not be easily derived from theory as the

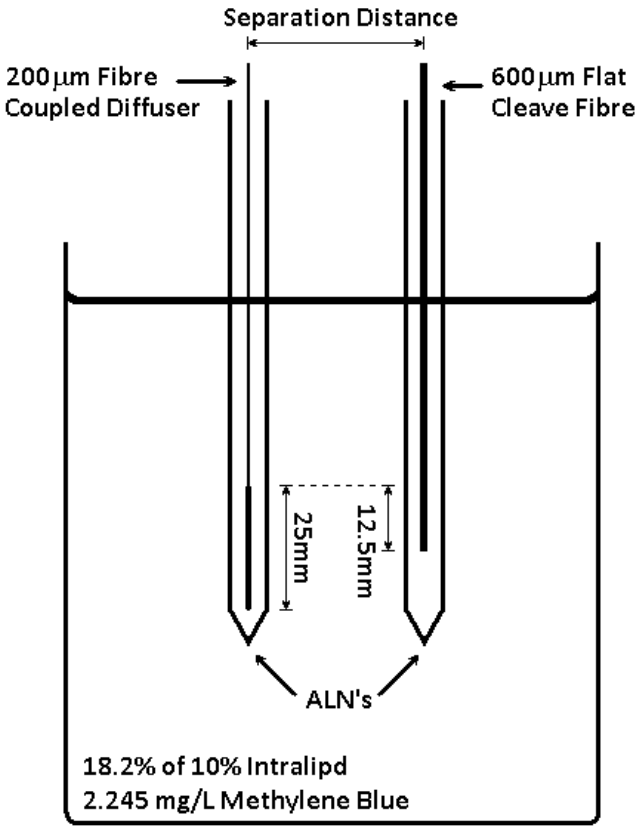

Figure 3.18: *in vitro* experimental setup showing the relative heights of the source diffusing element and the flat cleave fiber detector within afterloading needles (ALN's). The manipulated variable is the separation distance as well as drug concentration (modeled by additional methylene blue). The container is large enough such that the closest distance between any ALN and container boundary is several skin depth away. This is necessary to allow for negligible boundary effects.

geometry is not simple. The source is a 200 μm core diameter, 25 mm long cylindrical diffuser while the detector is a 600 μm core diameter flat cleave fiber. Both are housed inside 15 gauge ALN's which are scattering elements themselves. Figure 3.18 shows the partial experimental setup. Note that to use these results as a look up table, prostate boundary effects need to be ignored. This is possible as prostate dimension is large enough such that each fiber is multiple skin depths away from boundary and any boundary effects such as reflection would be greatly attenuated and can be ignored.

Optical phantom of 18.2% of 10% intralipid and 2.245 mg/L of methylene blue was prepared with varying concentrations of additional methylene blue to simulate SL-052 absorption. At 635 nm, every 0.26 mg of methylene blue has the same absorption as 1 mg of SL-052 when dissolved in the same volume. Equation 3.1 has the conversion formula with equation 3.2 having the numerical values obtained from Liu[67] and Prahl[48]. Figure 3.19 and 3.20 shows the detected 635 nm intensity at varying source-detector separation distances and varying SL-052 concentrations. The smooth gradation and linearization in the logarithmic plot shows that there is no significant equipment noise sources and helps to confirm reliability of our equipment setup. There was concern that because the inner diameter of the ALN is larger than the diameter of the cylindrical diffuser, the diffuser can shift laterally inside the ALN causing shifts in detected counts generating noise, but results show that such noise is insignificant.

These *in vitro* experimentation measurements are taken with the same setup used for actual canine prostate experiments, including going through the same optical switch, diffusers, ALN's, and patchcords as well as using the same laser sources. The effect of filters at 635 nm have been reversed (normalized as if there no filter was present). This is necessary for the data to be used as a look up table for canine experiments when separation distance is known but prostate drug concentration is unknown. The counts are normalized to 1 mW cylindrical diffuser output and a 1000 ms spectrometer integration time. One technical note is that gas bubbles tend to form on the outside of the ALN's when submerged for prolonged periods of time ($>$10 min). The bubbles were from dissolved gasses during rigorous mixing of the solution and the build up of bubbles was found to greatly affect experimental results due to index of refraction changes across the bubble layer. This problem was overcome by

frequently removing the ALN's from the mixture and re-submerging just prior to taking measurements.

$$m_{SL} \times \frac{1}{M_{SL}} \times \mu_{a_{SL}} \times \frac{1}{\mu_{a_{MB}}} \times M_{MB} = m_{MB} \tag{3.1}$$

$$1\,g_{_{SL}} \times \frac{1\,mol}{592\,g} \times \left(5.0 \times 10^4\,\frac{L}{mol \cdot cm}\right) \times \frac{1\,mol \cdot cm}{103986\,L} \times 319.85\,\frac{g}{mol} = 0.26\,g_{_{MB}} \tag{3.2}$$

3.5.1.1 Boundary condition errors

Since the container for the test medium is large enough such that the closest distance between any ALN and container boundary is several skin depth away, it was possible to ignore boundary effects.

3.5.2 Region of best signal-to-noise ratio

The purpose of this section is to determine the spectral location to take SL-052 fluorescence measurements from. Because the drug has a wide fluorescence profile spanning across regions with spectral noise, it is desirable to determine the optimal wavelength to extract SL-052 fluorescence data. This section is written with knowledge of canine experimentation. Specifically, this section uses data from canine light only control experiment to determine background noise in the absence of SL-052. Canine experiments are described in Chapter 4.

Figure 3.21 shows the fluorescence signal-to-noise ratio (SNR) plotted against SL-052 fluorescence profile and *in vivo* spectral noise lines. The SL-052 profile is the same as in Section 2.2.3. The spectral noise is background signal obtained during canine light only control experiment (no drug present). A

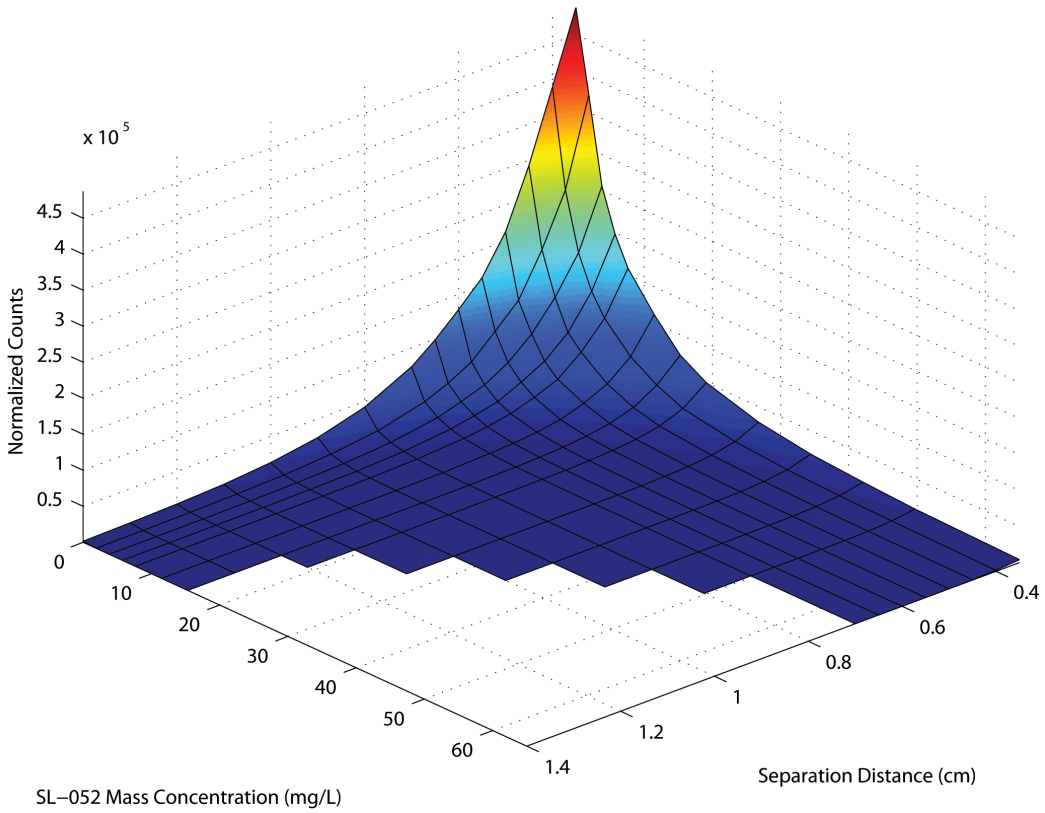

Figure 3.19: Experimental *in vitro* optical response at 635 *nm* used to model light transmission in canine prostate at varying separation distances and SL-052 concentrations.

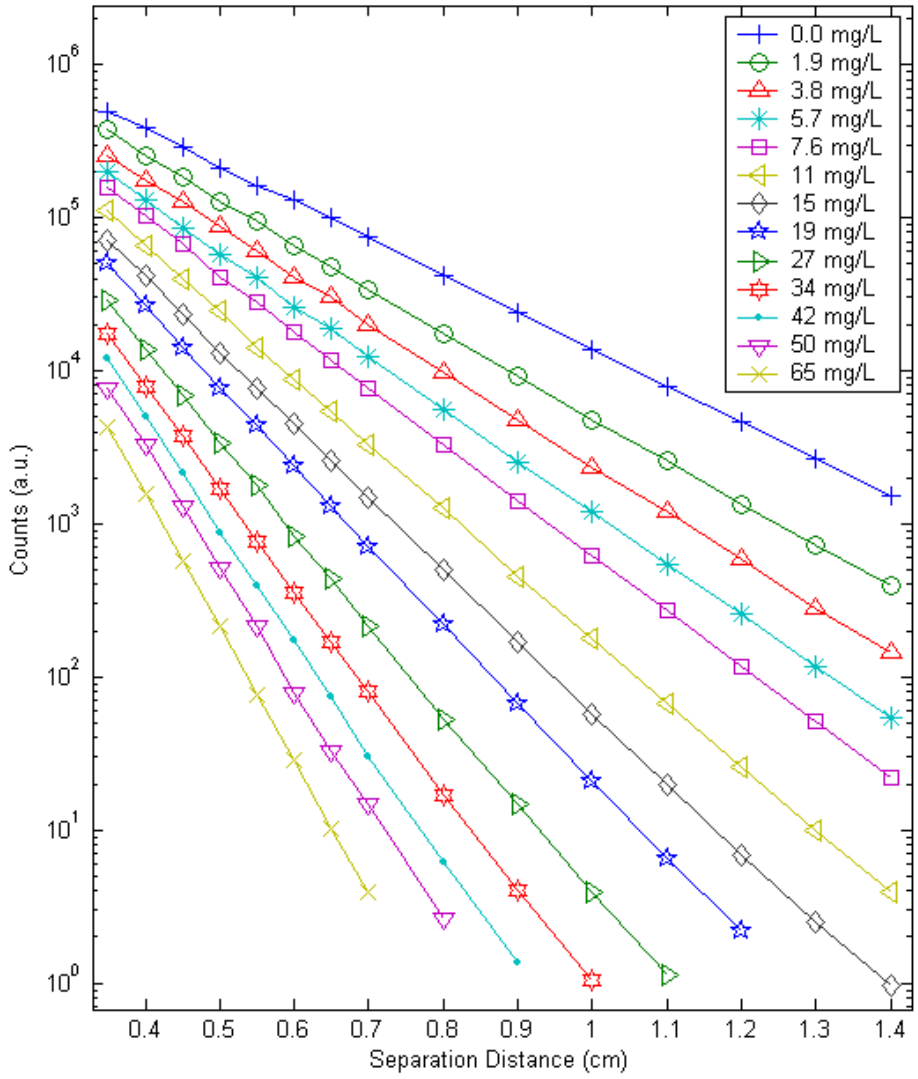

Figure 3.20: Logarithmic plot of experimental *in vitro* optical response at 635 *nm* with varying separation distances and SL-052 concentrations.

filter is used to suppress 635 nm excitation so that sufficient integration time can occur to capture the noise without spectrometer saturation due to strong excitation. This noise is on the order of 10^{-4} that of the detected excitation light (2mm RG665 filter with measured 635 nm of OD4.17). Note that "noise" here refers to a characterizable autofluorescence and is not the same as random noise which would greatly affect detection sensitivity.

In the absence of drug, the spectrometer detected spectral noise (see Section 3.4.5) when the tissue was illuminated with 635 nm light. To determine the wavelength range for the highest SNR, the fluorescence profile is divided by the *in vivo* spectral noise. Between 805–839 nm the SNR is at 95% of its maximum value. The wavelength range chosen for measuring *in vivo* fluorescence data is 810–820 nm, centered about the isosbestic point of oxy- and deoxy-hemoglobin: 815 nm (See Sections 2.1.4 and 2.2.3). This simplifies analysis of fluorescence data as it would be less affected by oxygenation state of hemoglobin since both oxy- and deoxy-hemoglobin have same 815 nm absorption coefficients.

3.5.3 Hardware Operation Considerations

While fiber optic technology is the obvious choice for interstitial light delivery, it has certain drawbacks. For our applications, there are two main draw backs associated with day to day operation of the system. One draw back is that fiber optic connectors are brittle and may be damaged when dropped onto a hard surface. A damaged connector may result in fiber misalignment and lead to large power losses and possible damage to laser source from feedback. In addition, a damaged connector may be difficult to identify leading to diagnosis difficulties when low power output is experienced. A second draw back is

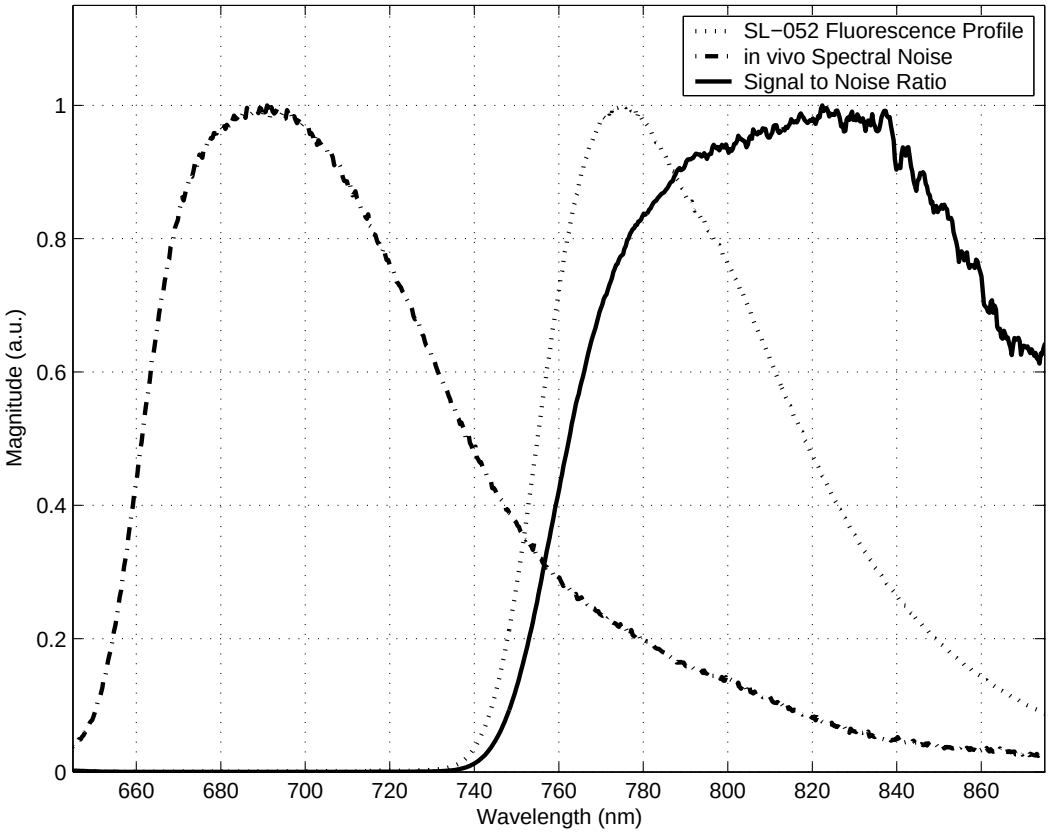

Figure 3.21: Fluorescence signal-to-noise ratio (SNR) plotted against pure SL-052 fluorescence and *in vivo* spectral noise lines. The noise is captured during canine light only control. The SNR line is a plot of the fluorescence profile divided by the noise signal to determine the wavelength location for the highest SNR. The SNR plot line gets noisy above 800 nm due to division by a small number magnifying the noise on the spectral noise line.

that fiber junctions (i.e. connector tips) need to maintain a high degree of polish for high light throughput. It is critically important that during every reconnection both fiber ends are clean of any debris. This applies to patch-cord ends, diffuser connectors and bulkhead connectors on the optical switch and the laser modules. Debris at fiber junctions may absorb, scatter light a well as scratch or even break the fiber core when pressure is applied during reconnections.

For lab applications, it is particularly important to exercise caution and maintain cleaning working environment and use high quality cleaning products. Through the course of this thesis, we have experienced high power losses (>90%) due to debris causing a loss of polish at a fiber junction. The problem resulted in excessive feedback light (a potential problem for any high power laser systems) into the laser module and caused damage to the laser diode. Service repairs had to be made. Since this experience we have used CLETOP (McKinney, USA) products, an industry leader in fiber optic cleaning products, for all fiber ends and bulkhead connectors every time a connection is made.

While being meticulous with cleaning procedures are acceptable for lab applications, such requirement is not ideal for clinical applications. However, the system built for clinical applications would be absent of these problems because reconnections should not be necessary. A permanent clinical treatment system should be fully enclosed within a small push cart with fibers permanently connected. There is no need for reconnections with the exception of broken fibers but such events should be rare. Therefore, the use of fiber optic technology is suitable for both lab and clinical applications.

For current apparatus, it should be noted that setup time takes approximately

1 hour including unpacking each piece of equipment, cleaning and reconnecting each fiber, all power checks, electronics connections, power connections, and program setup. For an inexperienced operator, plan for at least twice that time frame.

Chapter 4

Optical Response of SL-052 Mediated Canine iPDT

The majority of this project encompasses creating the iPDT system, testing it on canine prostates, and analyzing the resulting optical response. However, before canine testing, a set of investigations were performed on Dunning R3327-AT and -H tumor models to ensure that considerable photodynamic action and tissue damage can be attained *in vivo* on a smaller scale using the light delivery system and SL-052. This chapter begins with discussions of these rat investigations before moving on to the canine model. Note that *in vivo* experimentation was performed in collaboration with the biology group of our multidisciplinary PDT team.

4.1 Dunning Rat Models

In vivo experimentation were performed on two types of tumor models grown on the flank of Copenhagen rats: Dunning R3327-AT and Dunning R3327-H.

The -AT tumors are characterized by highly aggressive growth with less developed vasculature. The -H tumors are less aggressive and have better developed vasculature. The purpose of this investigation is to affirm the photodynamic action and tumor control capability of SL-052 on these two tumor models when excited with our switched light delivery system *in vivo*.

4.1.1 Drug Delivery

SL-052 delivery for all rat models are performed through tail vein injection of the liposomal formulation of the drug. That is, the lipophilic SL-052 is encapsulated in 100 - 200 μm liposomes so that it is soluble in blood. Drug-light interval (i.e. the time between drug injection and light delivery) is set at the optimal time of 3 hours[68]. Drug dose was prescribed as a per body mass figure and ranged between 4 to 8.5 mg/kg.

4.1.2 Light Delivery

The light delivery and detection system continually evolved through the course of this program. Initially, for the rat investigations, the system was designed for only light delivery without detection. The initial system is as described in chapter 3 except without any detection components. Integrating sphere and spectrometer detection were later introduced in preliminary form and will be discussed later. Power output for each cylindrical diffuser was set at 200 mW giving a linear power density of 133 mW/cm for the 1.5 cm long diffusers. Prescribed light doses varied between 0.4 to 1.0 J/mm^3 with volumes varying between 1.4 to 4.6 cm^3 for -AT tumors and 0.6 to 1.0 J/mm^3 with volumes varying between 1.7 to 6.4 cm^3 for -H tumors.

4.1.3 Results

Figure 4.1(a) shows R3327-AT tumor growth rates for treated animals compared to various control groups. As light and drug dose increase, tumor growth is delayed and the time at which it takes the tumor to grow to 4X pre-treatment volume increases. Figure 4.1(b) divides the treated animals into 3 groups: low dose ($<$6.5 mg/kg, 0.3 - 1.0 J/mm^3), medium dose (7.5 mg/kg, 0.5 - 0.7 J/mm^3), and high dose (7.5 - 8.5 mg/kg, 0.8 - 1.0 J/mm^3) and shows survival proportions over time post-treatment. Animals are sacrificed when tumor volume reaches 4X pre-treatment volume. Comparing treatment groups with control groups, these two figures clearly show that photodynamic action has occurred as a result of the unification of drug and light. Drug only and light control only groups had similar responses as completely non-treated animals (true controls), whereas animals with combined drug and light showed tumor growth delay. Figure 4.2 shows examples of monitored daily tumor growth post-iPDT. Again, clearly photodynamic action as occurred as groups with both drug and light showed much slower growth rates than the control groups. Minor tumor growth delay is observed at the low dose group while much more significant growth delay, including tumor volume reduction in some cases, is observed at medium and high dose groups demonstrating tumor control capability of SL-052 when excited with our switched light delivery system *in vivo* for aggressive -AT tumors. Similarly, photodynamic action and tumor control were present for the Dunning R3327-H tumor investigation. Observed results show significant tumor growth delay for all drug and light dose combinations[69].

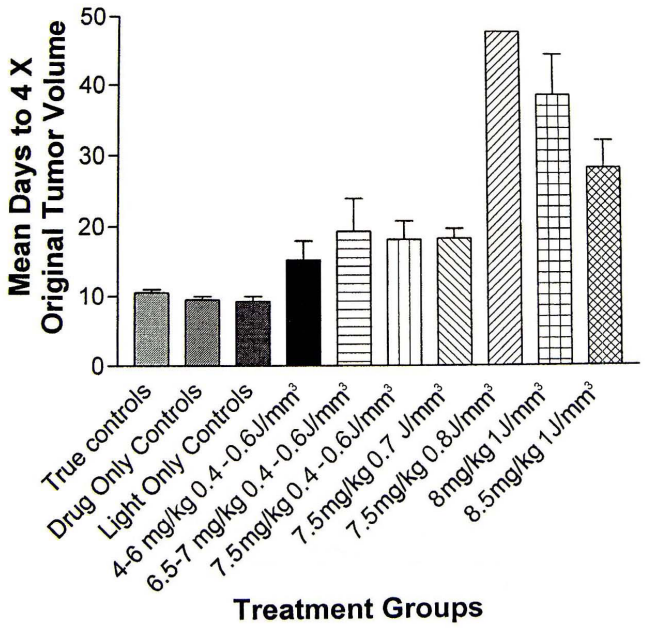

(a)

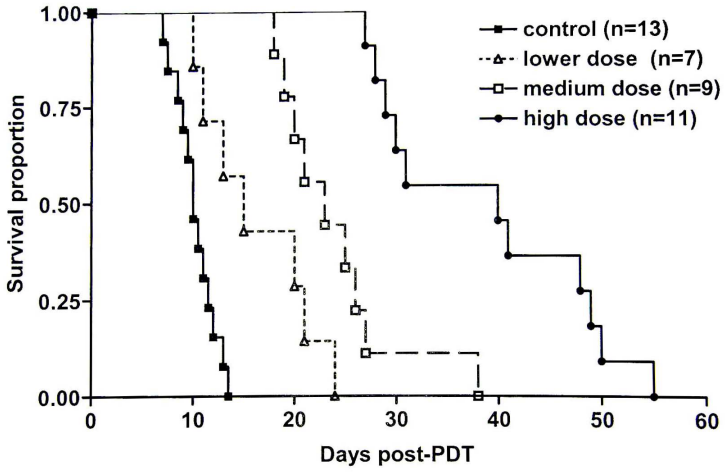

(b)

Figure 4.1: Dunning R3327-AT tumor control. (a) Tumor growth rates post iPDT showing mean days to 4X pre-treatment tumor volume. (b) Copenhagen rat survival proportion as a function of time post-iPDT for the four treatment groups. Animals are sacrificed when tumor volume reaches 4X pre-treatment volume. Figure prepared in collaboration with the biology group of our PDT team[70].

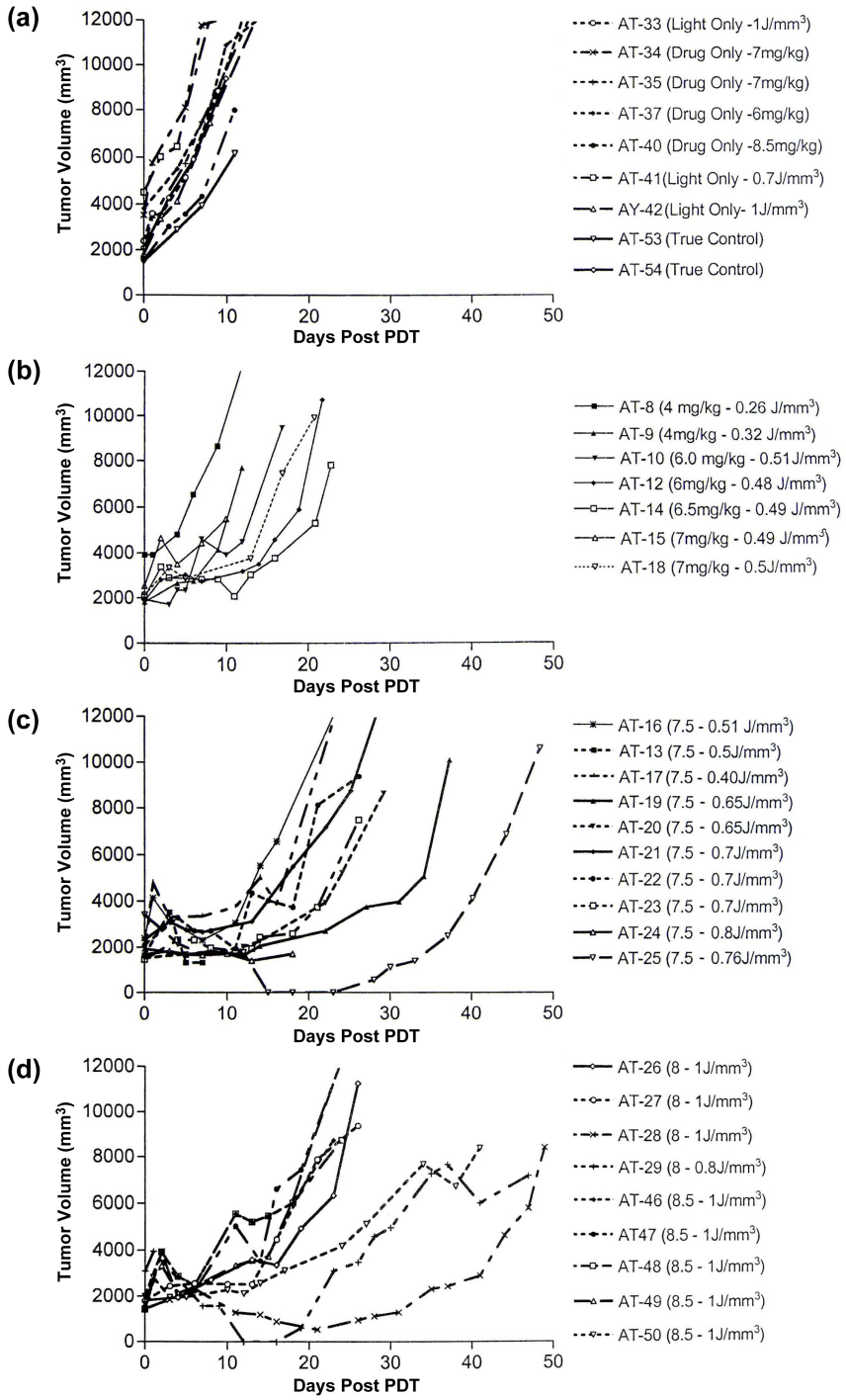

Figure 4.2: Dunning R3327-AT tumor growth, volume versus days post iPDT, for the four groups: (a) control group, (b) low dose, (c) medium dose, and (d) high dose. Compared to the control group, there is a clear indication of delayed growth for all treatment groups. In the medium and high dose groups, tumor volume reduction was present in some animals. Figures prepared in collaboration with the biology group of our PDT team[70]

4.1.4 Discussions

Although a complete necrosis of tumorous tissue would have been the preferred clinical result, the rat investigation did achieve significant tumor growth delay with tumor volume reduction in some cases. The union of SL-052 and 635 *nm* light clearly demonstrated tumor control capability in both the aggressive R3327-AT and the more vascularized -H tumor lines. The investigation showed that this particular switched light delivery system was effective at delivering excitation light to induce photodynamic action. In fact, switched light delivery have shown to be superior to continuous delivery for a different photosensitizer[50]. While further rat investigations may lead to complete eradication of the cancerous tissue through adjustments in drug or light dose, such investigation is not necessary as the purpose of the rat investigation was to show photodynamic effect. The specific dose required for possible complete necrosis of Dunning R3327 tumor lines on Copenhagen rats will most likely not be equivalent to the appropriate dose required for canine investigations or human clinical trials due to physiological differences and differences in drug delivery (IV versus IA), and drug dynamics. Therefore, such rat investigations would be irrelevant.

4.1.5 Integrating Sphere Excitation Light Detection

Using integrating sphere to monitor *in vivo* 635 *nm* excitation light fluence was preliminarily tested on the rat model before implementation of auto detection in the canine model (see section 3.4.2). The preliminary testing involved setting up the integrating sphere to detect light via diffusers through the fiber optic switch to gauge if sufficient light throughput would be available to be

detected. With the typical sizes of the rat tumor models, the integrating sphere picked up signal on the order of 100's to 1000's of nW. This was above the device's dark signal of a few nW but by only 2-3 orders of magnitude and presented a challenging problem. In order to confidently gauge if such detection would be applicable in canine iPDT, we need to know two things: (1) approximate canine prostate dimensions so that we can estimate source-detector separation distances and (2) drug distribution within the prostate so that we can estimate attenuation within the prostate. The second point was an unknown, especially considering a novel intra-arterial drug delivery method was the main subject of investigation. At this point, the most practical step was to test this monitoring system during actual canine experiments to see if sufficient light is available to be detected.

4.2 Canine Experimental Design

4.2.1 Drug Delivery

Traditionally, iPDT photosensitizer is administered via intravenous (IV) delivery allowing the drug to circulate throughout the body and accumulate in the target tissue. There are several disadvantages to this method. First, a large amount of drug must be used to accommodate for dilution and uptake losses over the entire body. Second, because a large amount of drug circulates within the body, the skin may become photosensitive. Third, selectivity of PDT is dependent on the overlap range of light and photosensitizer. Most photosensitizers are not highly selective to prostate tissue or to cancerous cells. IV administration of photosensitizer results in significant accumulation in prostate adjacent tissues[71, 72, 73, 74]. Since diffuse light in tissue does

not have a distinct cut off, light administration with high selectivity is challenging. Inter-patient variations and optical anisotropies within the prostate make highly accurate light targeting more difficult. Because IV administration of photosensitizer is not highly selective and light selectivity is difficult to control, patients are at risk of collateral damage. In contrast, intra-arterial (IA) photosensitizer administration, a novel concept for PDT introduced recently by our PDT group[75], delivers a small amount of drug directly into an artery feeding the target tissue. This allows the photosensitizer in first-pass to be either trapped in the target tissue arteries or capillaries, with subsequent uptake by the endothelial cells and delayed delivery to glandular and stromal tissue cells. The method may potentially achieve higher therapeutic ratios as less photosensitizer may be used to attain higher localized concentrations due to direct access to target tissue before being trapped by liver and spleen filtration during first pass. Photosensitizer that makes it past the target tissue and circulates throughout the body is of limited concern because the amount of drug is small compared to the full body mass of the patient. This results in an ideal situation for PDT, where the target tissue has a high concentration of drug while the rest of the body contains negligibly small concentrations. IA delivery mode has the potential for much higher therapeutic ratios than IV delivery, with minimal risk of skin toxicity and better selectivity and thus less demand on light delivery accuracy.

Because SL-052 is lipophilic, there were two types of drug formulations utilized. DMSO formulation involved SL-052 dissolved in 2.0 ml of dimethyl sulfoxide (DMSO) for IA delivery. Liposomal formulation required the drug supplier preparing SL-052 trapped in 100 - 200 μm liposomes to allow it to be soluble in an aqueous environment. For liposomal formulation, both IA and IV delivery methods were tested.

IA delivery protocol involved interventional radiographic delivery where prescribed drug dose is bilaterally delivered directly into the canine prostatovesical artery via percutaneous cannulation through the iliac artery using standard angiographic techniques. For IV delivery protocol, SL-052 is delivered via left cephalic vein along with 80 ml of PBS.

iPDT was performed on 17 healthy canines with 13 for IA–DMSO, 2 for IA–liposomal, and 2 for IV-liposomal. Additionally, there were 1 light only control and 2 drug only controls. IA drug dose varied from 1.0 to 18.0 mg of SL-052 per prostate, equally divided between the two lobes. There is a large variance in prescribed drug concentration. The high concentration of 18.0 mg was prescribed initially to ensure that sufficient drug stayed in the tissue and could be verified with the light detection system. Verification was confirmed at all concentrations via SL-052 fluorescence[67]. Prescribed photosensitizer dosage was slowly backed off following verification of drug from previous animals. The two animals that underwent IA–liposomal delivery were each given 18.0 mg of drug. The two animals that underwent IV–liposomal delivery were given 160 mg which converts to approximately a per body weight dosage of 7.5 mg/kg.

4.2.2 Light Delivery and Detection

Light delivery setup for canine experiments is as described in Section 3.4. Light was delivered 3 hours post IV drug injection to allow for bio accumulation and uptake. The 3 hour delay (drug-light interval) was the optimal time shown in Dickey[68] for Dunning R3327-AT tumors. This accumulation time is not necessary for IA delivery and light was delivered 1 hour post IA drug injection to accommodate time for surgery.

Fibers were implanted into the prostate ventral to dorsal during laparotomy using the template as a guide spaced out in the 7 fiber configuration. Seven 1.5 cm cylindrical diffusers, six hexagonally spaced with one at the center, with linear power densities between 167 to 233 mW/cm equally delivered 635 nm light. Note that initially, while all fiber connectors are new, we were able to easily attain throughput of approximately 400 mW per fiber. We chose to use 350 mW (233 mW/cm) at the time. However, due to repeated assembly and disassembly, the throughput slowly dropped most likely due to light loss at fiber junctions. The maximum power we could deliver per fiber slowly dropped with each use. During the last few canines, the power was set to only 250 mW (167 mW/cm). For future clinical applications, the system is expected to be enclosed and mounted on a push cart with sufficient robustness allowing for transportation without the need to disassemble the fibers.

Treatment was based on light dose per prostate volume using a ellipsoid volume approximation for the prostate. Prescribed doses varied between 0.2 to 0.6 J/mm^3 with prostate volumes varying between 6 to 36 cm^3. Light delivery per fiber location is time-fractionated into 100 second intervals per set, 4 sets per cycle as described in Section 3.4.2. Initially, the system utilized both the integrating sphere and spectrometer. Upon review of results, it was evident that the spectrometer alone was sufficient, allowing for decreased complexity and shorter treatment duration (see section 4.5.1.1). Continuous spectral detection was performed via an eighth probe implanted between the center fiber and one of the six outlying fibers. Long-pass filters were used to keep the excitation 635 nm source signal and 815 nm fluorescence signal within the dynamic range of the spectrometer so both signals can be continuously monitored. Table 4.1 summarizes the treatment parameters for all 18 canines. The charted "drug dose" is a calculated figure based on the following: For

Dog #	Treatment Mode	Total Drug Weight (mg)	Drug Dose (mg/L)	Tumor Volume (cm^3)	Light Energy (J)	Light Dose (J/mm^3)
LO-1	Light Only	0	0	10.4	4053	0.39
IV-lipo-01	IV (liposome)	160	7.5	12.8	4422	0.35
IV-lipo-02	IV (liposome)	160	7.5	10.5	6313	0.60
IA-Lipo-01	IA (liposome)	18	1395	12.9	6432	0.50
IA-Lipo-02	IA (liposome)	18	1184	15.2	4824	0.32
IA-DMSO-01	IA (DMSO)	18	1314	13.7	8085	0.59
IA-DMSO-02	IA (DMSO)	18	984	18.3	8220	0.45
IA-DMSO-03	IA (DMSO)	9	381	23.6	9380	0.40
IA-DMSO-04	IA (DMSO)	15	417	36.0	6432	0.18
IA-DMSO-05	IA (DMSO)	6	225	26.7	8040	0.30
IA-DMSO-06	IA (DMSO)	6	405	14.8	5829	0.39
IA-DMSO-07	IA (DMSO)	6	955	6.3	1257	0.2
IA-DMSO-08	IA (DMSO)	4	243	16.5	4948	0.3
IA-DMSO-09	IA (DMSO)	4	249	16.0	4811	0.3
IA-DMSO-10	IA (DMSO)	2	150	13.3	3992	0.3
IA-DMSO-11	IA (DMSO)	2	134	14.9	4464	0.3
IA-DMSO-12	IA (DMSO)	1	49	20.3	6083	0.3
IA-DMSO-13	IA (DMSO)	1	79	12.6	3794	0.3

Table 4.1: Treatment parameters for Canine iPDT. Note that drug dose for IV administration is delivered drug weight divided by animal mass and has units (mg/kg). For IA administration, it is delivered drug weight divided by volume of prostate with units (mg/L). It is not the actual drug dose in the prostate but is presented here to give the ratio of drug weight delivered to canine mass or to prostate volume.

IV administration, it is delivered drug weight divided by canine mass and has units (mg/kg), assuming that SL-052 distributes evenly throughout the animal body. For IA administration, it is delivered drug weight divided by volume of prostate with units (mg/L). This term does not describe actual localized drug dose in the prostate but is presented as a reference figure to describing the drug-to-animal-mass or drug-to-prostate-volume ratio. However, we expect some correlation between actual prostate drug dose and the charted "drug dose" figure as we would expect the prostate volume or canine weight to have an effect on prostate drug concentration.

4.3 Raw Optical Response

This section presents the raw optical response seen from the spectrometer. Presented first is the optical response observed during the light only control animal to show the background noise. Then a description of the components of a typical raw optical response will be presented, followed by be raw data from the various iPDT treatment modes.

4.3.1 Canine Background Spectra

The spectral profile of canine light only control is plotted in figure 4.3. The detected spectra measured *in vivo* from multiple fiber sets of light only control canine are nearly identical in shape. The profile is also very similar in shape to that produced with the same equipment configuration *in vitro*. This has a few implications. Firstly, it shows that that the detectable spectral noise *in vivo* is most likely the same equipment noise discussed in Section 3.4.5. Secondly, this shows that at around this wavelength range (700-850 nm) and for prostate dimensions on the order of centimeters, propagation through tissue does not drastically alter the shape of the noise profile. That is, in this range, tissue absorption is not highly wavelength dependent. Thirdly, it shows there is no significant tissue autofluorescence observed at the intensity level of the equipment noise. That is, any tissue autofluorescence is buried and not easily discernible from the hardware noise. Note that in these zero drug spectra, the peak of the noise is between 690 and 696 nm.

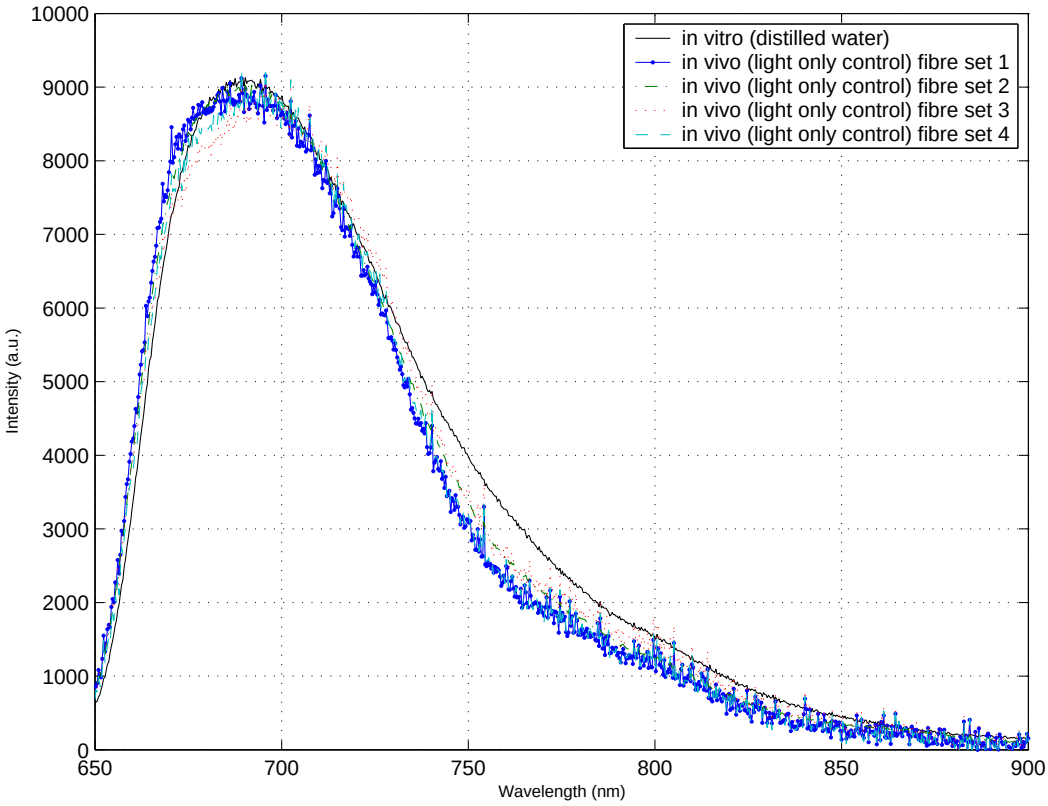

Figure 4.3: Spectral profile of canine light only control showing similar shape to *in vitro* testing in distilled water with same equipment setup. This spectral noise does not significantly change in shape as it propagates through canine prostate tissue.

4.3.2 iPDT Optical Response

There are 3 main components to the detected spectral response of iPDT: 635 nm excitation, SL-052 fluorescence, and system noise from autofluorescence of diffusers. Figure 4.4 overlays SL-052 fluorescence profile with raw detected spectral response from a canine receiving IA-DMSO delivery mode. This is a typical spectrum for IA delivery modes with relative intensities changing slightly depending on drug dose delivered. The two peaks formed by the drug fluorescence and diffuser autofluorescence are at 796 and 740 nm respectively. System noise spans between 665 and 800 nm. SL-052 absorption convolutes with the system noise and reduces measured noise intensity nonlinearly causing a red shift of the noise peak (See Section 4.3.2.1).

From *in vitro* measurements of system noise and drug fluorescence (See Section 3.5.2), the location of best SL-052 fluorescence signal-to-noise ratio is between 810 and 820 nm. Recorded fluorescent intensity is integrated over this range and recorded excitation intensity is averaged over 631 and 640 nm. These averaged counts are then normalized to the case of 1000 ms spectrometer integration time and divided by the filter transmission over their respective ranges. They are then divided by the laser output power. The final resulting count is a figure representing the averaged counts over their respective wavelength range that would would be detected by an unfiltered spectrometer at 1000 ms integration time for a 1 mW laser source. This is considered the absolute fluorescence or excitation counts (or count rate since it is a per second figure). This is the exact same way the counts for *in vitro* optical response are measured (Section 3.5.1). These wavelength ranges are shown in as the highlighted regions in figure 4.4. The overlaid *in vitro* drug fluorescence profile matches the raw signal in the range outside system noise and drug

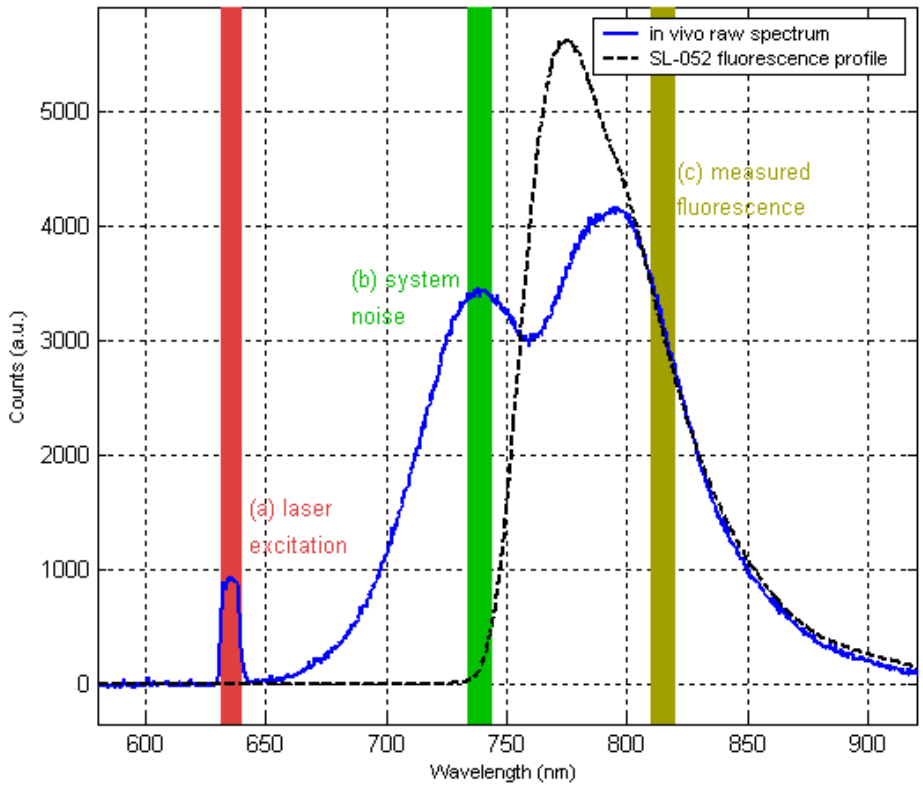

Figure 4.4: Typical raw detected spectrum from canine receiving IA-DMSO delivery mode showing (a) the excitation light after being partially filtered out by 635 *nm* attenuation optical filter, (b) the system's optical noise generated from autofluorescence of diffusers, and (c) the fluorescent signal in the zone of highest signal-to-noise ratio. The spectrum is overlaid with *in vitro* SL-052 fluorescence to illustrate fluorescence region.

self-shielding effects. It is important to note that self-shielding from the drug may cause the drug fluorescence peak to appear to red shift. Location of the noise peak is the wavelength location of the local maximum forming the noise characteristic.

4.3.2.1 Red Shift of Spectral Profiles

To explain the red shift of both the fluorescence peak and the diffuser autofluorescence noise peak, consider the absorption effects of the drug. Figure 4.5 models the transmission profile of SL-052 in a 1-dimensional non-scattering media with length 7 mm at varying drug concentrations. The model is Beer-Lambert law (equation. 4.1) for transmission through a media, with molar absorption coefficient μ_a, length l, and molar concentration of absorbing agent c. For our applications, the absorption coefficient is obtained from figure 2.2; the length is 7 mm (the most common *in vivo* source-detector separation distance) and the molar concentration is converted to mass concentration using the molar mass of SL-052 of 592 g/mol.

$$T = \exp(-\mu_a l c) \tag{4.1}$$

While this 1-D non-scattering model is a gross simplification of our applications, what can be extracted from this is that the transmission profile of SL-052 appears like a long-pass filter over the wavelength range of the autofluorescence noise. The transition wavelength of the long pass filter shifts to longer wavelengths at higher concentrations. This is the most likely explanation for the red shift of both the fluorescence peak and the noise peak. At this point, it may seem possible to correlate a specific red-shift in the aut-

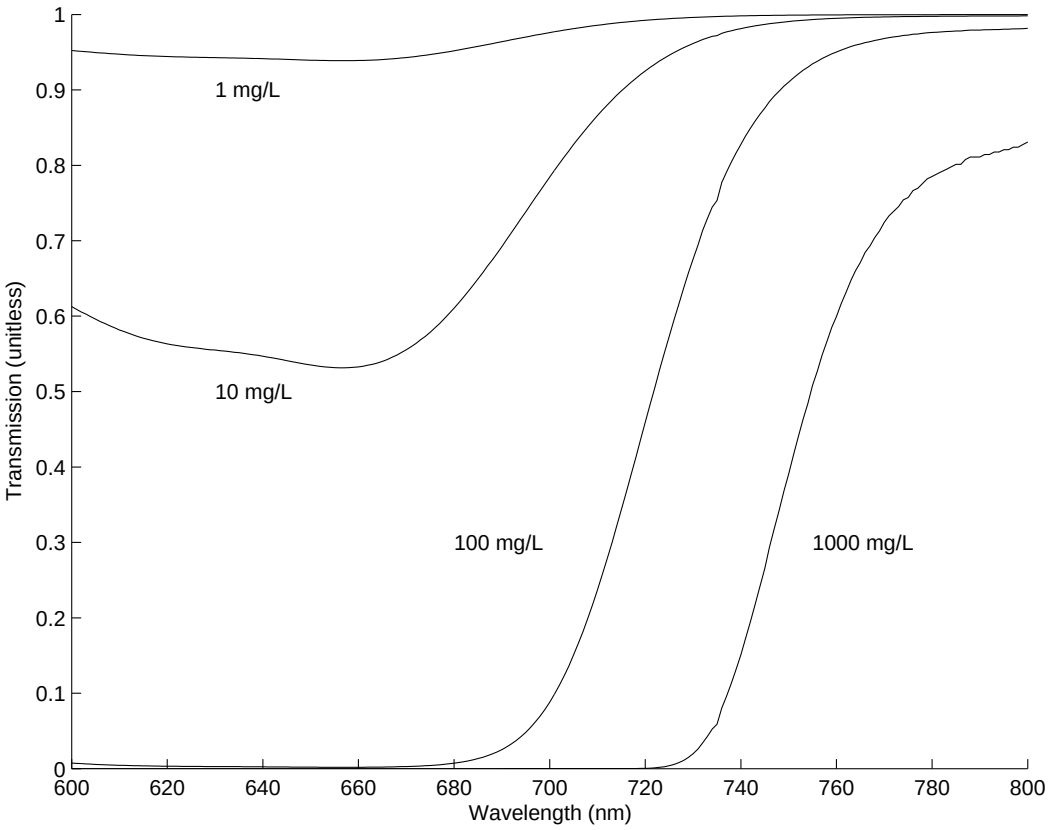

Figure 4.5: Transmission spectra of SL-052 at varying drug concentrations modeled for 1D non-scattering media with length of 7 mm.

ofluorescence noise profile with a specific transmission profile of SL-052 and in turn correlate with a specific drug concentration necessary to create that transmission profile. However, due of the simplicity of this model, the exact shape of the SL-052 transmission profile *in vivo* cannot be extracted, nor can a quantitative correlation with SL-052 concentration be obtained accurately.

It may be a worthwhile endeavor for future investigation to model the transmission profile of SL-052 in tissue and use the long-pass filter characteristic to determine local drug concentration. Necessary steps would include measuring tissue absorption and scatting coefficients over the wavelength range of interest. If the assumptions of diffusion approximation to light transport can still hold, then it would need to be applied for a linear diffusing source by assuming a linear source is a superposition of spherical point sources. Such a model would also be necessary in order to accurately create a subtraction algorithm for eliminating the autofluorescence noise.

4.3.2.2 IA-DMSO Case

The detected spectra for the iPDT of canines that underwent IA-DMSO drug delivery show a wide range of detected profile characteristics between the 15 animals. Figures 4.6, 4.7 and 4.8 display captured spectra with detected SL-052 fluorescence being high, medium and low, respectively, compared to the autofluorescence noise. High refers to profiles where the drug fluorescence peak is greater in detected counts than the noise peak. Medium refers to profiles where the drug fluorescence peak has less counts than the noise peak but the fluorescence characteristic has a definitive local maximum. Low refers profiles where fluorescence characteristic exists but has no definitive maximum. Note that these categories have no quantitative basis but are declared here

for ease of presentation and description of the graphical spectra. To capture these spectra, the detection filter for this delivery mode was 2, 3, or 5 mm RG645. These filters were necessary to keep both the 635 nm and fluorescence/autofluorescence signals on roughly the same level such that both are within the dynamic range of the spectrometer. In a rare case, the spectra from one fiber set could be captured without any in-line long-pass filters. The optical density of these filters at 635 nm is shown in Table 3.2 where 5 mm refers to stacked 2 and 3 mm. As we shall see, the magnitude of 635 nm attenuation necessary for these IA-DMSO canines is far less than that necessary for the other drug delivery modes. One possible explanation is that for these IA-DMSO delivery modes, there is much higher SL-052 absorption of the excitation light than compared to the other modes.

There is a fourth category which are spectra where the fluorescence characteristic is not discernible from the noise characteristic. Examples of this are shown in figure 4.9. These examples are all taken with 5 mm RG645, the strongest 635 nm attenuating filter used for IA-DMSO canines. In these examples, the excitation light spectra is far greater in magnitude than the peak of the noise spectra and for the purpose of illustrating the noise/fluorescence spectral profile, the peak of the excitation light profile is not visible at this magnification. Note that it does fall within the dynamic range of the spectrometer and is recorded without clipping.

4.3.2.3 IV-liposome Case

There were no clearly discernible fluorescence spectral characteristic observed during the iPDT of canines mediated by liposomal SL-052 delivered via IV-mode (Figure 4.10). The spectra look very similar to that of the canine back-

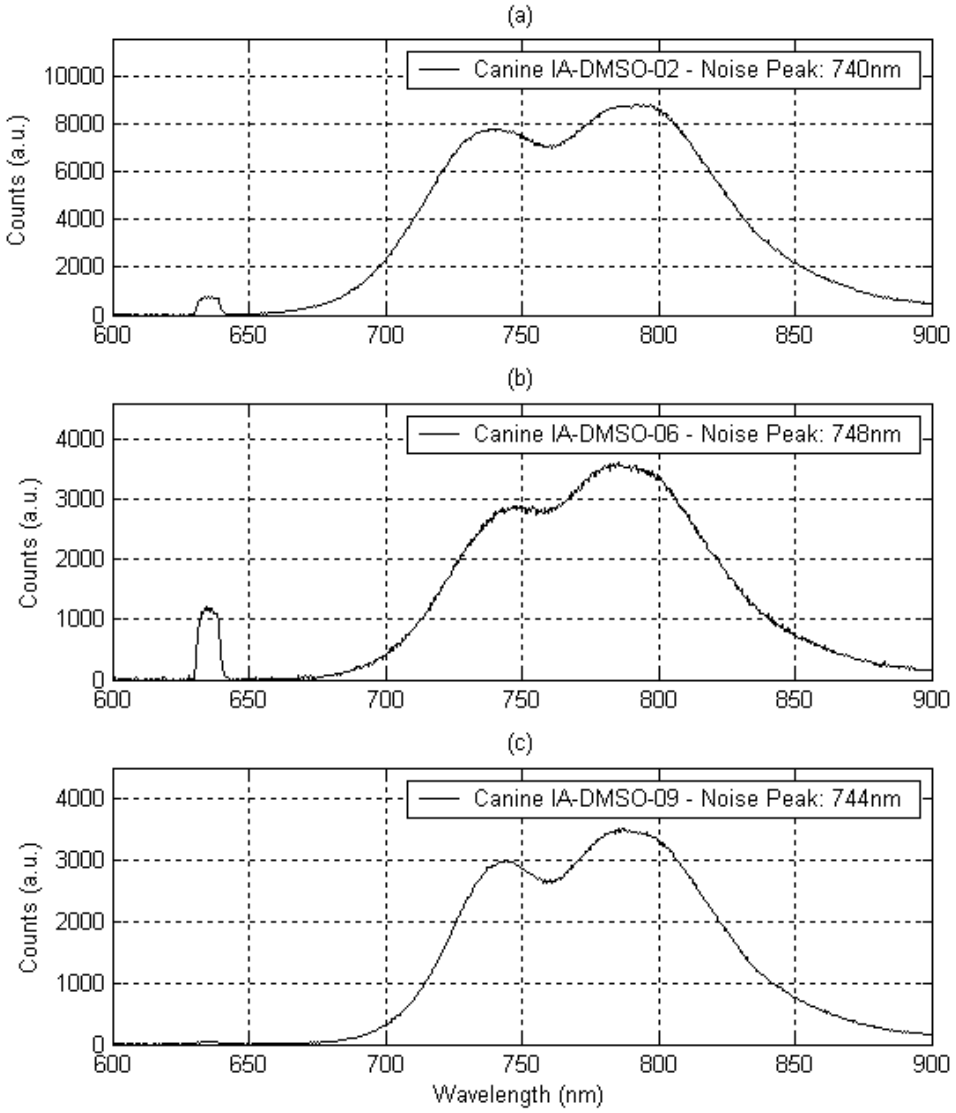

Figure 4.6: Raw spectrometer detected spectra during iPDT of canines mediated by IA delivered SL-052 in DMSO. (a), (b) and (c) are examples from three different canines at fiber sets showing high fluorescence.

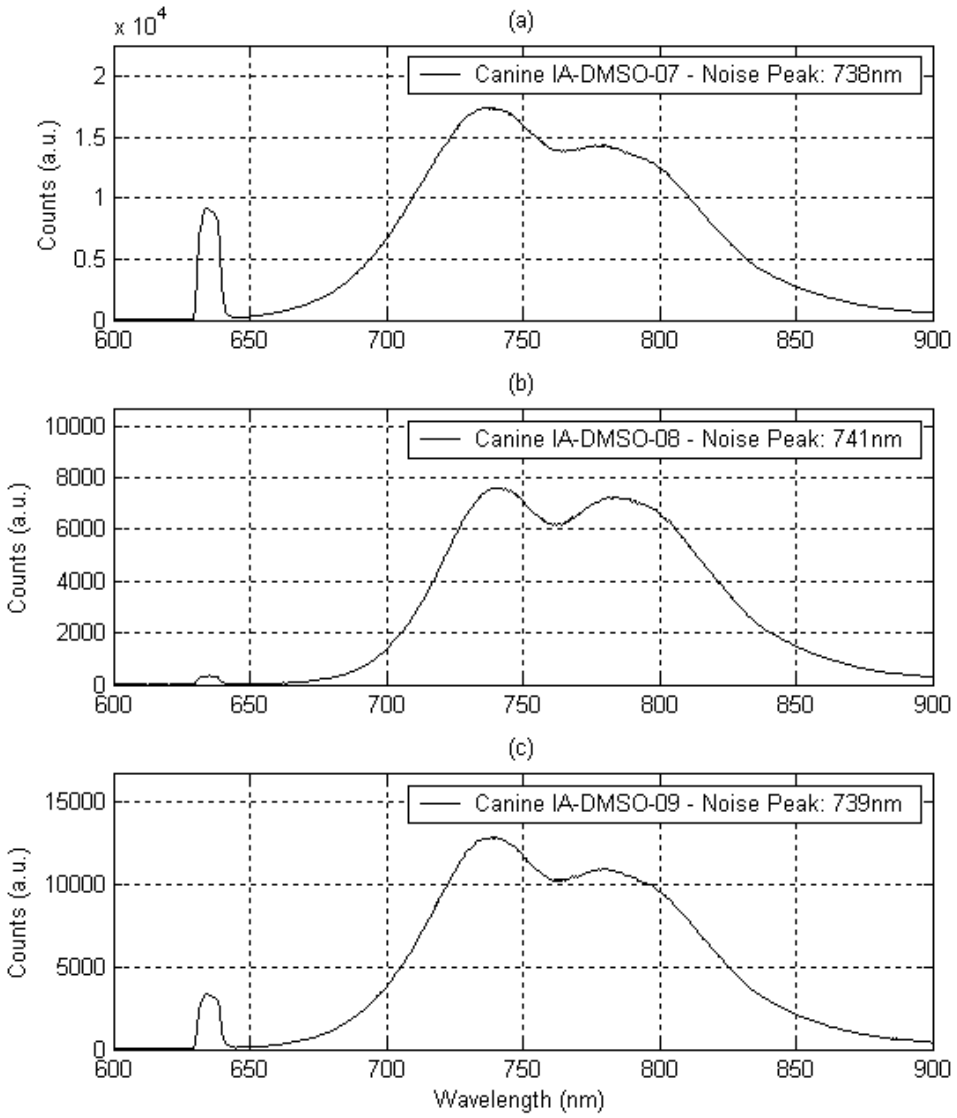

Figure 4.7: Raw spectrometer detected spectra during iPDT of canines mediated by IA delivered SL-052 in DMSO. (a), (b) and (c) are examples from three different canines at fiber sets showing medium fluorescence.

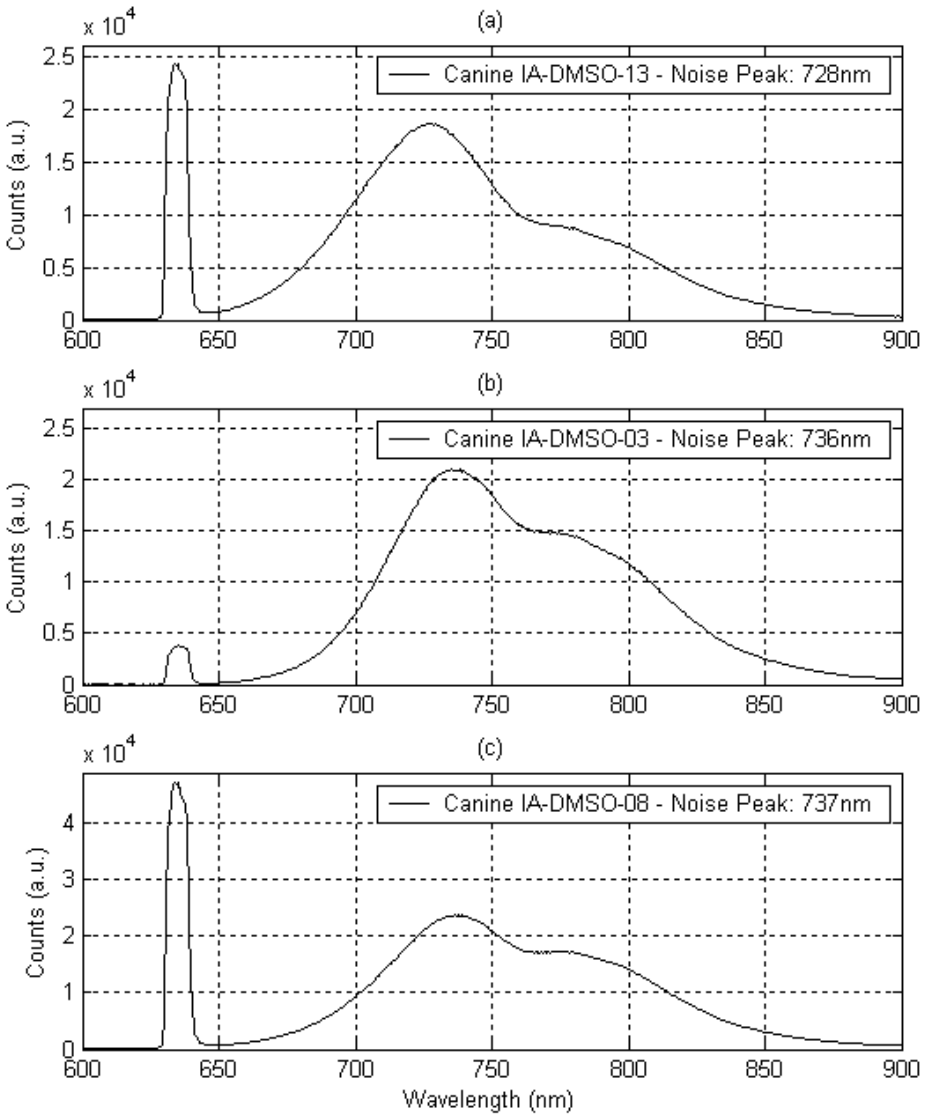

Figure 4.8: Raw spectrometer detected spectra during iPDT of canines mediated by IA delivered SL-052 in DMSO. (a), (b) and (c) are examples from three different canines at fiber sets showing low fluorescence.

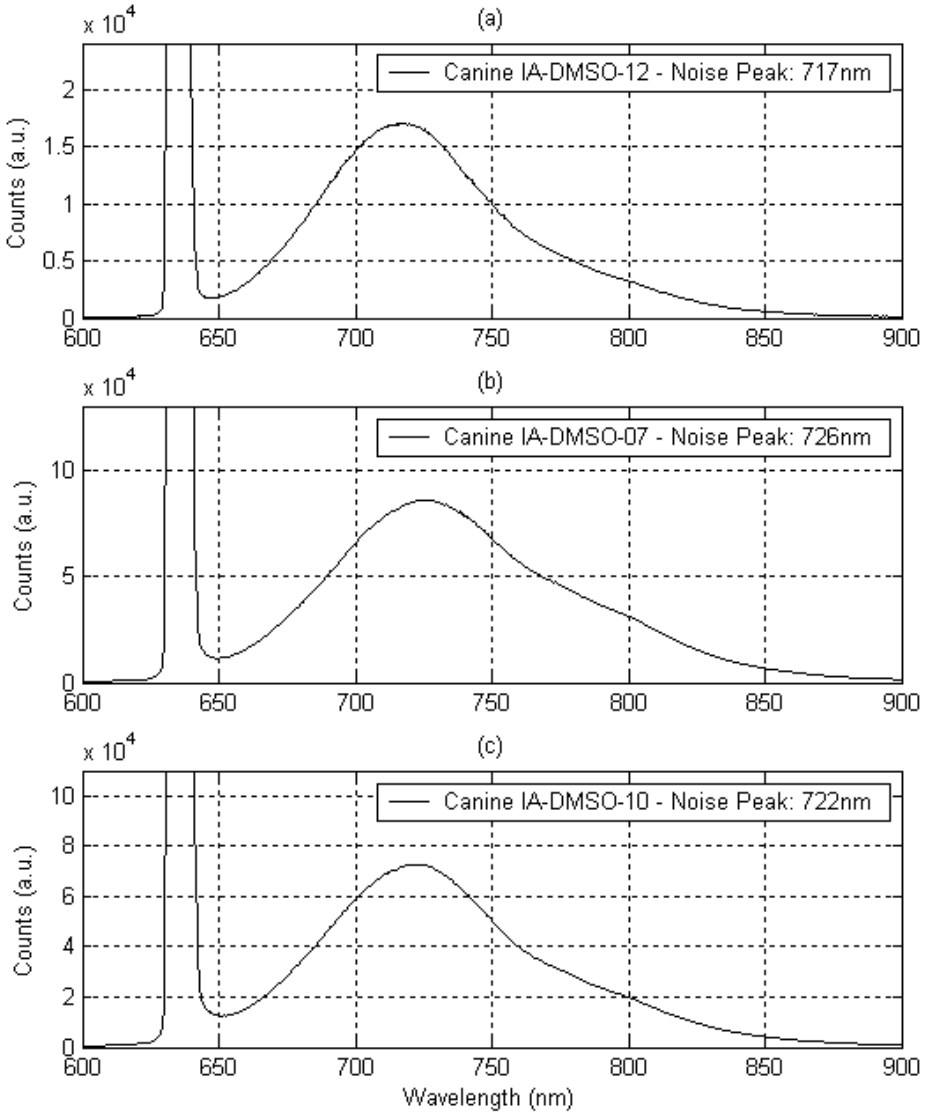

Figure 4.9: Raw spectrometer detected spectra during iPDT of canines mediated by IA delivered SL-052 in DMSO. (a), (b) and (c) are examples from three different canines at fiber sets showing no clearly discernible fluorescence characteristic. Note that in these figures, the excitation spectra is cropped off. The captured data does contain the full excitation spectra but the data is presented this way to focus on showing the noise and fluorescence spectra.

ground. However, there seems to be a red shift in the peak of the noise profile. The peaks of the autofluorescence noise falls between 700 and 712 *nm* for all the recorded fiber sets for these 2 canines. When comparing *in vitro* profiles of liposomal formulated SL-052 in distilled water (Figure 4.11), we see a red shift in the peak of the noise as liposomal SL-052 concentration increased. The magnitude of the red shift seems to be similar to that of the *in vivo* spectra; however, the drug concentration can not be directly drawn as the distilled water medium does not model scattering or tissue absorption.

To capture these spectra, the detection filter for this delivery mode was 2 *mm* RG665. This was necessary to keep both the 635 *nm* and fluorescence signals on roughly the same level such that both are within the dynamic range of the spectrometer. This is the strongest attenuation filter used among all canine experiments. It is also the same one used for the intra-arterial delivery route with liposomal SL-052 carriers.

4.3.2.4 IA-liposome Case

Similar to IV-liposome case, there was no clearly discernible fluorescence profile observed in the spectra for intra-arterial delivered SL-052 in liposome carriers (Figure 4.12). Any fluorescent signal is buried in noise. This may be attributed to a rapid clearance of the water soluble liposomal drug. The peaks of the autofluorescence noise falls between 697 and 714 *nm* for all the recorded fiber sets for these 2 canines.

To capture these spectra, the detection filter for this delivery mode was also 2 *mm* RG665. Again, this was necessary to keep both the 635 *nm* and fluorescence signals on roughly the same level such that both are within the dynamic range of the spectrometer. This is the strongest attenuation filter used among

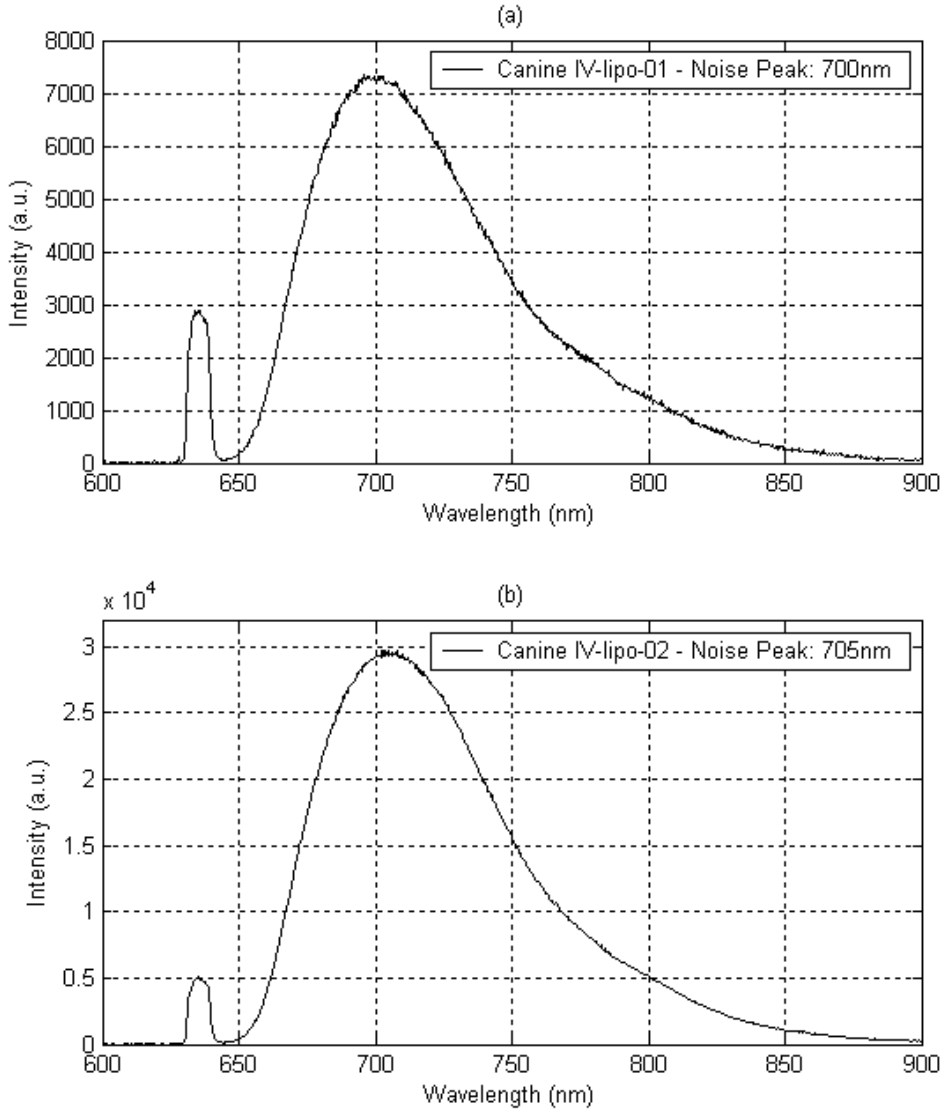

Figure 4.10: Raw spectrometer detected spectra during iPDT of canines mediated by IV delivered SL-052 in liposomal carriers. (a) and (b) are examples from two different canines with noise peak location at 700 and 705 nm respectively.

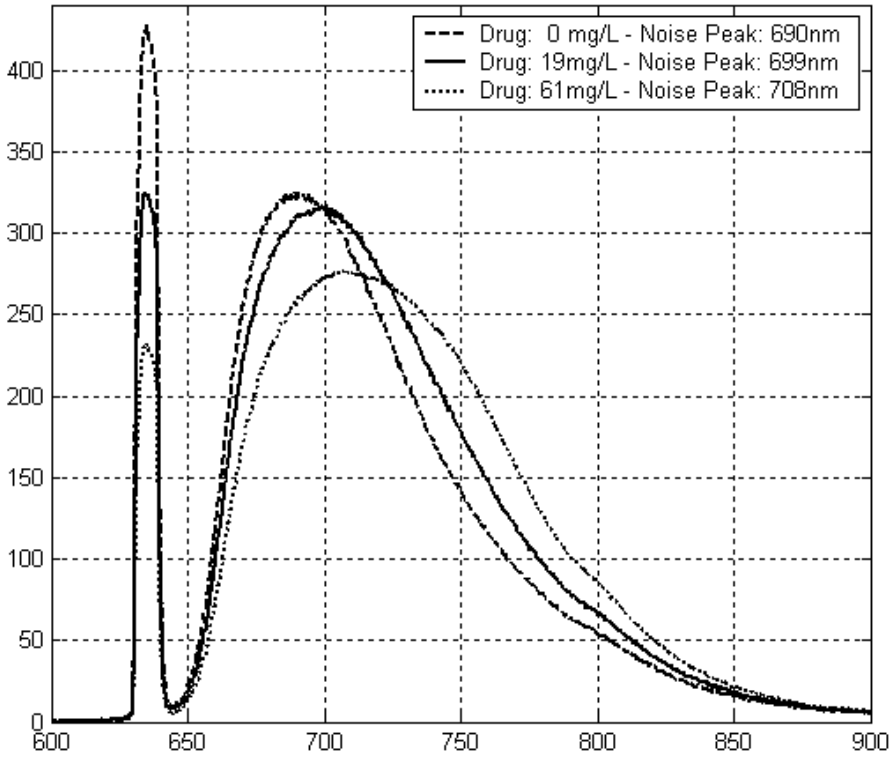

Figure 4.11: Spectra of distilled water with SL-052 at varying concentrations. The peak of the noise characteristic red shifts as drug concentration increases.

all canine experiments. It is also the same one used for the intravenous delivery route with liposomal SL-052 carriers.

4.3.2.5 General Discussions

The above results mainly discussed the fluorescence and autofluorescence signals. The 635 nm excitation light signal remains to be discussed. With the exception of a rare few, the 635 nm excitation signal can be clearly deciphered from the raw spectra. Because detected 635 nm signal strength is very high, long-pass filters had to be utilized to reduce 635 nm radiation and maintain it and other spectral characteristics within the dynamic range of the spectrometer. The larger the relative difference between the excitation signal and the next largest signal, the stronger the long-pass filter that had to be utilized. It has been noted that the IV and IA-Liposome modes required the use of a much stronger 635 nm attenuation filter than any of the IA-DMSO modes. This shows that there is a much larger relative difference between 635 nm excitation and the fluorescence/autofluorescence characteristics for these two modes than the IA-DMSO mode. We speculate that it is due to lower concentrations of SL-052 in these two modes resulting in less 635 nm absorption; however, further analysis needs to be made before any solid conclusions can be made. The next section deals with time-independent characteristics followed by a section discussion time-dependent characteristics.

4.4 Time-Independent Investigation

This section discusses observed results from the first light cycle of the treatment. It considers data extracted from the initial treatment spectra when

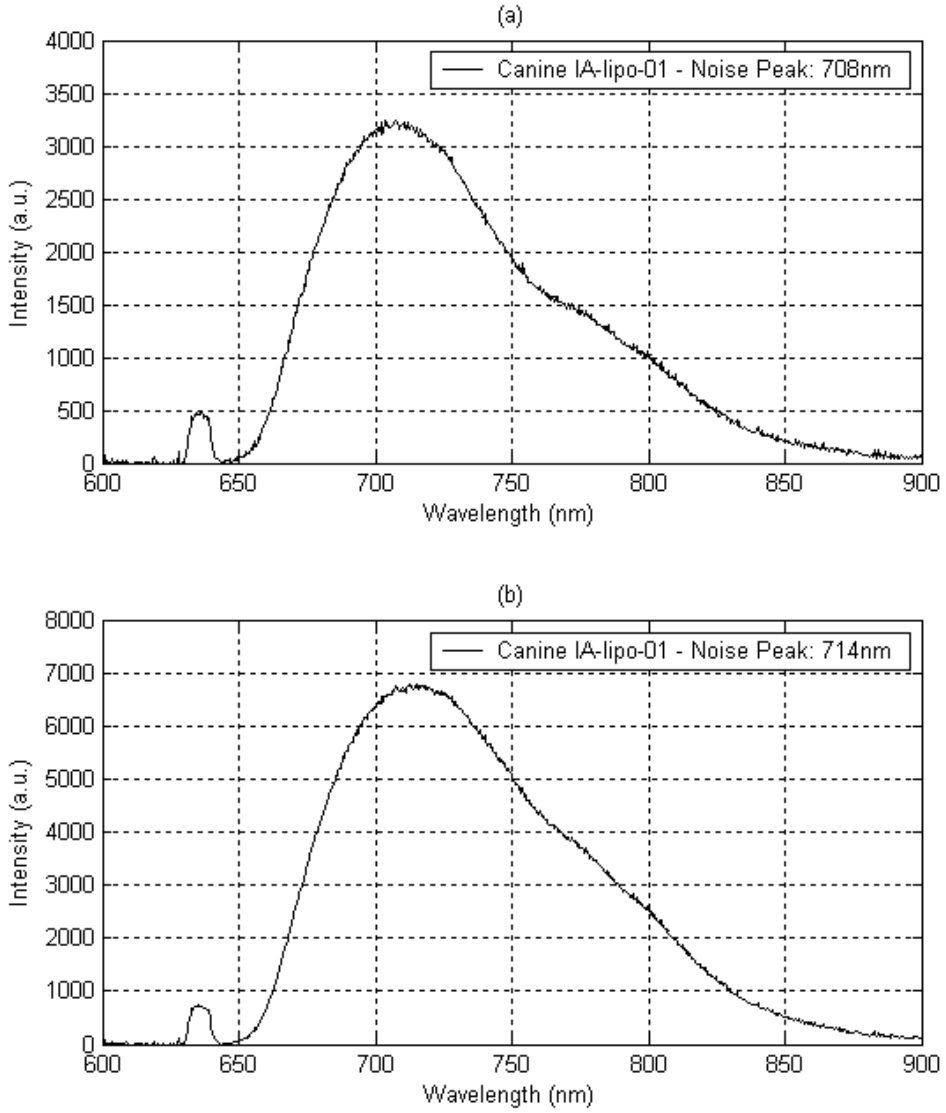

Figure 4.12: Raw spectrometer detected spectra during iPDT of canines mediated by IA delivered SL-052 in liposomal carriers. (a) and (b) are examples from two different canines with noise peak location at 708 and 714 nm respectively.

minimal photodynamic effect had occurred. The purpose is to gain insight to the initial pre-treatment state of the prostate. More specifically, we intend to find a metric to which we can use to determine local drug concentration in the prostate based on the optical response. This would improve our understanding of pharmacokinetics of SL-052 as well as allow for adjustment of light dose based on initial local drug concentration and perhaps lead to improved treatment efficacy.

4.4.1 Relative Fluorescence and Noise Peak Location

One of the most obvious metrics for measuring drug concentration is the drug fluorescence signal. At equal source-detector separation distances, the higher the drug concentration, the stronger the fluorescence (assuming no saturation). However, the amount of fluorescence is also based upon excitation available from the source. With increasing separation distances, the fluorescence signal would decrease due to less excitation light available to induce the fluorescence. Therefore, the metric I propose is the relative fluorescence, or the detected fluorescence counts divided by the detected excitation counts. In this case, the longer the separation distance, the greater the path length available for interaction between drug and excitation light. The most ideal method for evaluating this metric is to compare with actual localized SL-052 concentration in prostate. However, measuring actual drug concentration would require extraction of tissue and invalidate these canine experiments for determining the prostate reduction capabilities of our iPDT system. Therefore, to evaluate this metric, a comparison is made with the previously discussed metric from Section 4.3.2.1. This phenomenon involves SL-052 causing a red-shift of the noise profile with increasing SL-052 absorption. The magnitude of the

red-shift depends on the drug concentration and the effective path length of photons between source and detector. The location of the noise peak is thus the other metric to compare with.

Figure 4.13 shows the comparison of relative fluorescence with the location of the noise peak. Plotted in log scale, the comparison shows very strong correlation with an $R^2 = 0.93$ from the linear regression fit. The excellent fit shows that there is good agreement between the two proposed metrics. The IA-DMSO spectra showed signs of much higher SL-052 concentration than the other two modes (See Section 4.3.2). This is confirmed in the comparison of the two metrics. Both metrics show that the IA-DMSO mode had greater SL-052 concentration than IV-Liposome or IA-Liposome modes, suggesting higher SL-052 concentrations from IA-DMSO drug administration modality compared to the other two. The light only control showed the lowest sign of drug presence which is expected. To the best of my knowledge, similar evidence has not been presented before and this is completely novel.

The greatest weakness for this comparison is that no direct measurement of actual local drug concentration is available to evaluate the two metrics. However, having such strong correlation between metrics that have fundamentally different basis of measurement is evidence suggesting that they may be suitable for optically measuring drug concentration. To achieve this, a set of calibration measurements would need to be made in order to create a reference calibration table, similar to Section 3.5.1, but for these two metrics. For future studies, the calibration table may be used to optically measure *in vivo* SL-052 concentrations in real-time during therapeutic light delivery and may direct changes in light output to coordinate with local drug concentrations and improve treatment dosimetry.

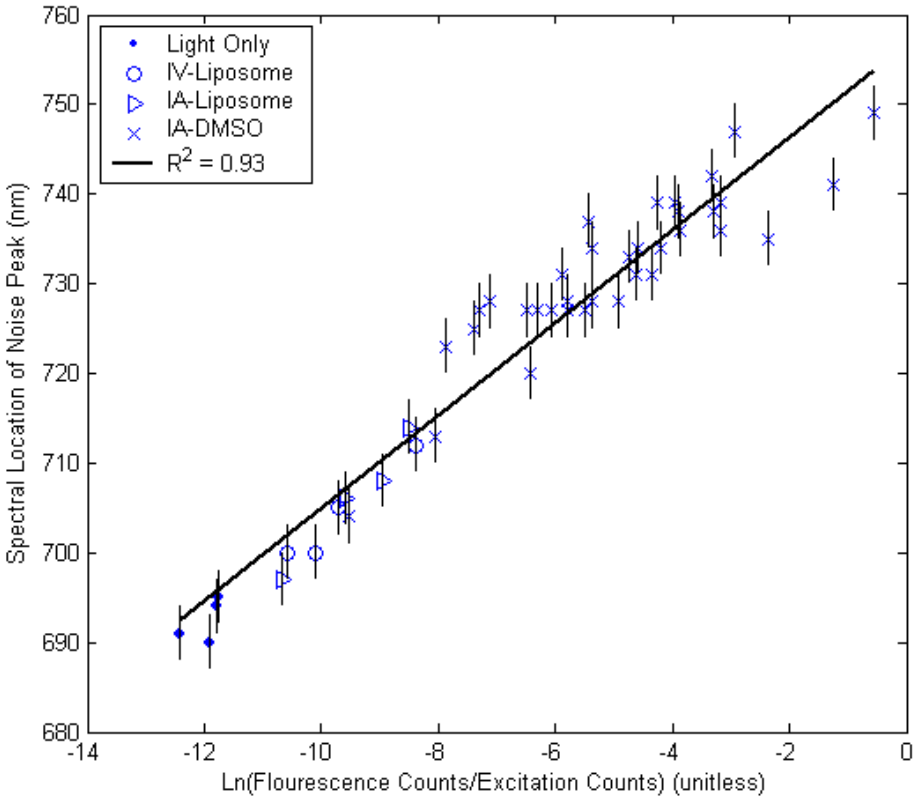

Figure 4.13: Comparison of two proposed metrics for optically measuring SL-052 concentration: relative fluorescence and noise peak location. The two metrics showed strong correlation with a linear regression $R^2 = 0.93$. The error bars are errors from determining peak location of noise profile.

An interesting corollary is that the autofluorescence of the diffusers are used for this analysis for noise peak location. Without this autofluorescence noise, the metric would not have been possible. Again, to the best of my knowledge, using diffuser autofluorescence to measure drug concentration is a completely novel concept for photodynamic therapy.

Because intra-arterial delivery of SL-052 is a novel concept and performed for the first time during this canine investigation, the drug distribution in prostate is an unknown. Comparisons are made for IA-DMSO canines at varying delivered SL-052 drug weights for constant source-detector separation distances to check for correlation between drug delivered and relative fluorescence. The comparisons for the four most common separation distances, 3.5, 6.1, 7.0 and 9.3 mm, are shown in figures 4.14, 4.15, 4.16 and 4.17 respectively. For a given source-detector separation distance, if the prostate drug concentration is highly dependent on total drug weight delivered, then we would expect that the higher the delivered drug weight, the higher the relative fluorescence. In the figures, this would be expressed as a good correlation between delivered drug weight and relative fluorescence. From the figures, this is clearly not the case. No strong correlation is observed at the given number of samples points. However, the volume of the prostate has not been taken into account. The drug dose value from table 4.1 divides the delivered drug weight by the measured prostate volume. The relative fluorescence is then plotted against these drug dose values in the same figures. Again, no strong correlation is observed at the given number of sample points. This result suggests that there is a highly dynamic drug distribution behavior. The optical evidence for prostate SL-052 concentration has no observed correlation with the delivered total drug weight or the drug dose. This is not too surprising as we expect DMSO dissolved SL-052 to aggregate when injected into blood stream and be trapped

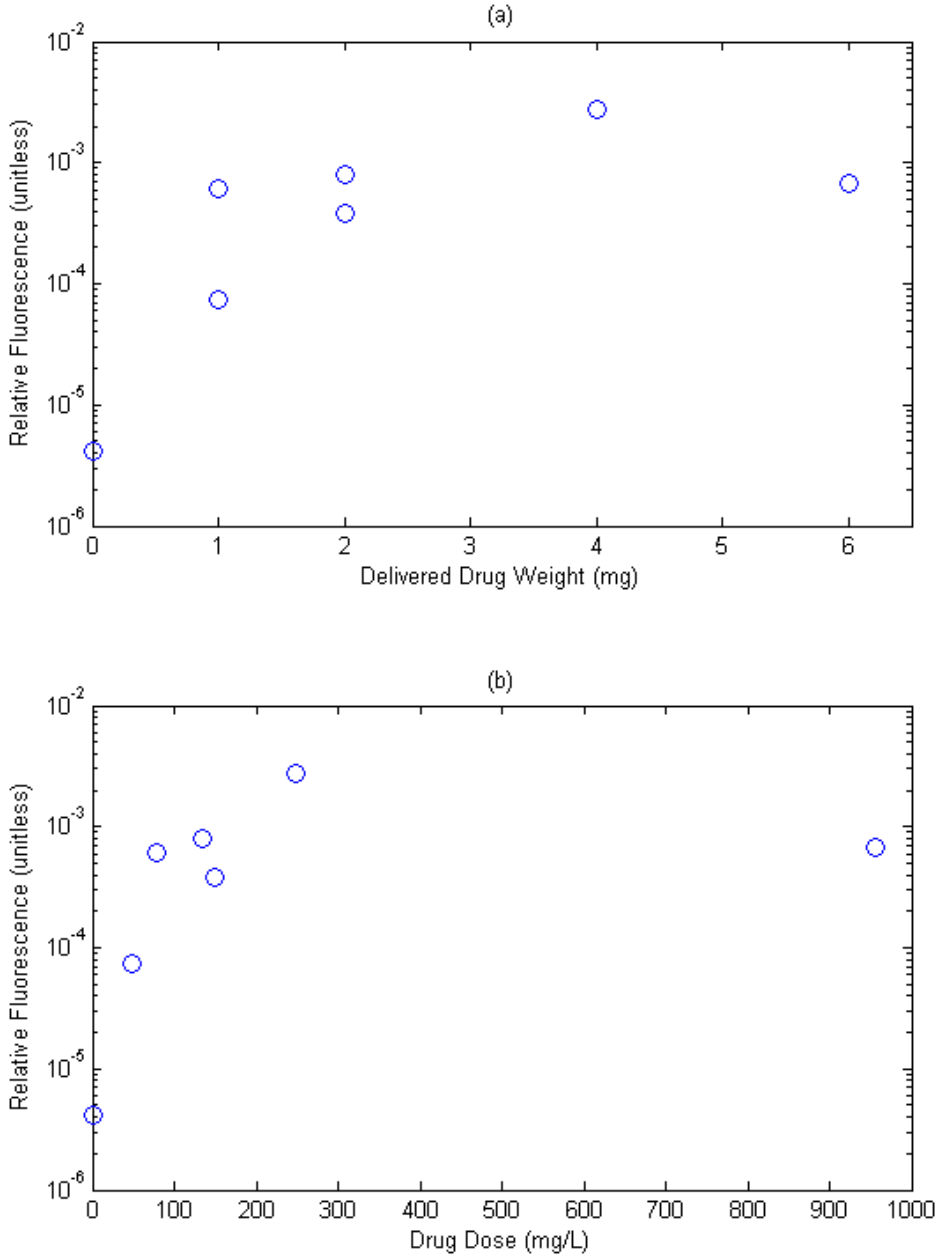

Figure 4.14: Comparison of relative fluorescence to (a) total delivered drug weight for the canine and (b) the drug dose in terms of total drug weight divided by prostate volume. This is for source-detector separation distance of 3.5 mm.

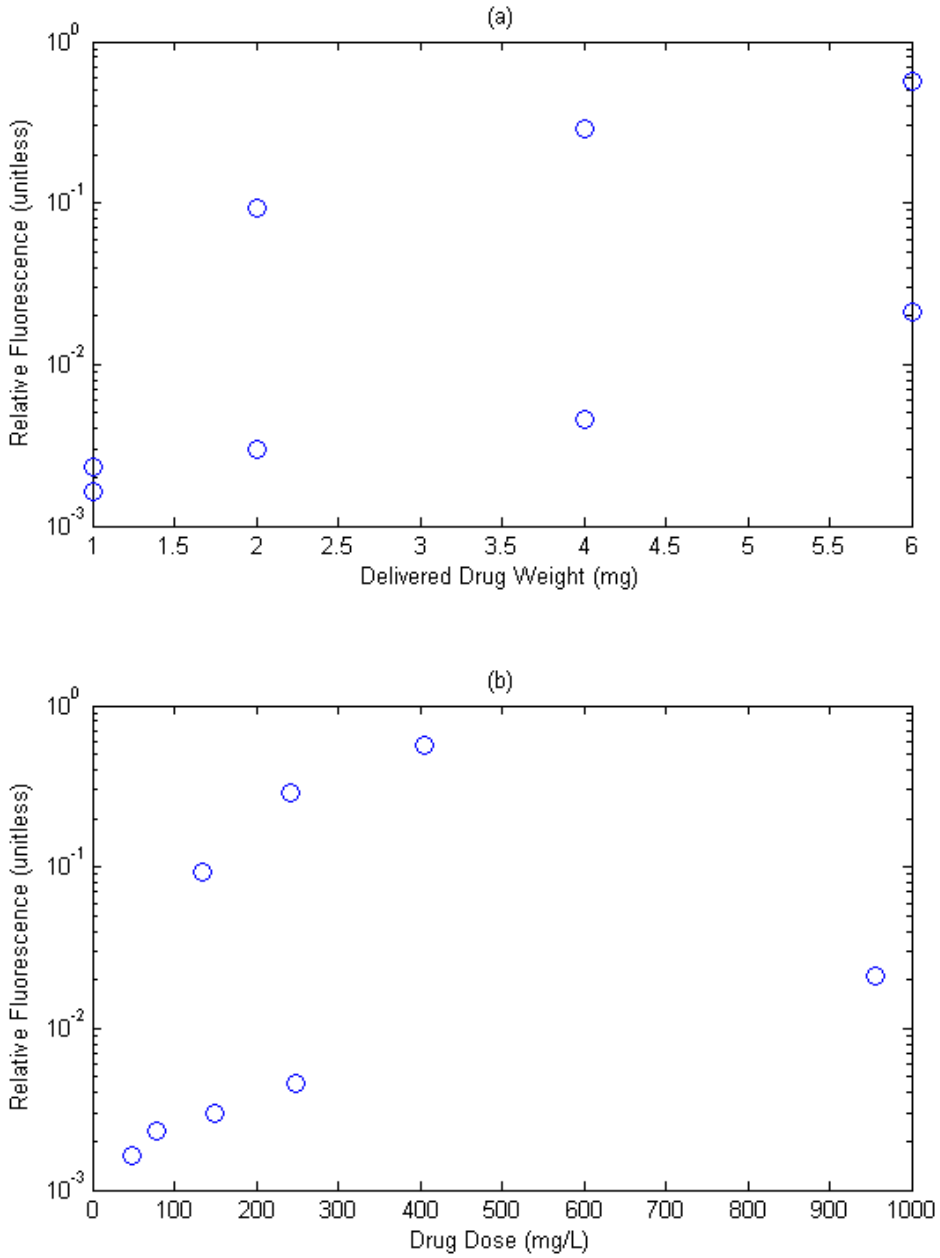

Figure 4.15: Comparison of relative fluorescence to (a) total delivered drug weight for the canine and (b) the drug dose in terms of total drug weight divided by prostate volume. This is for source-detector separation distance of 6.1 mm.

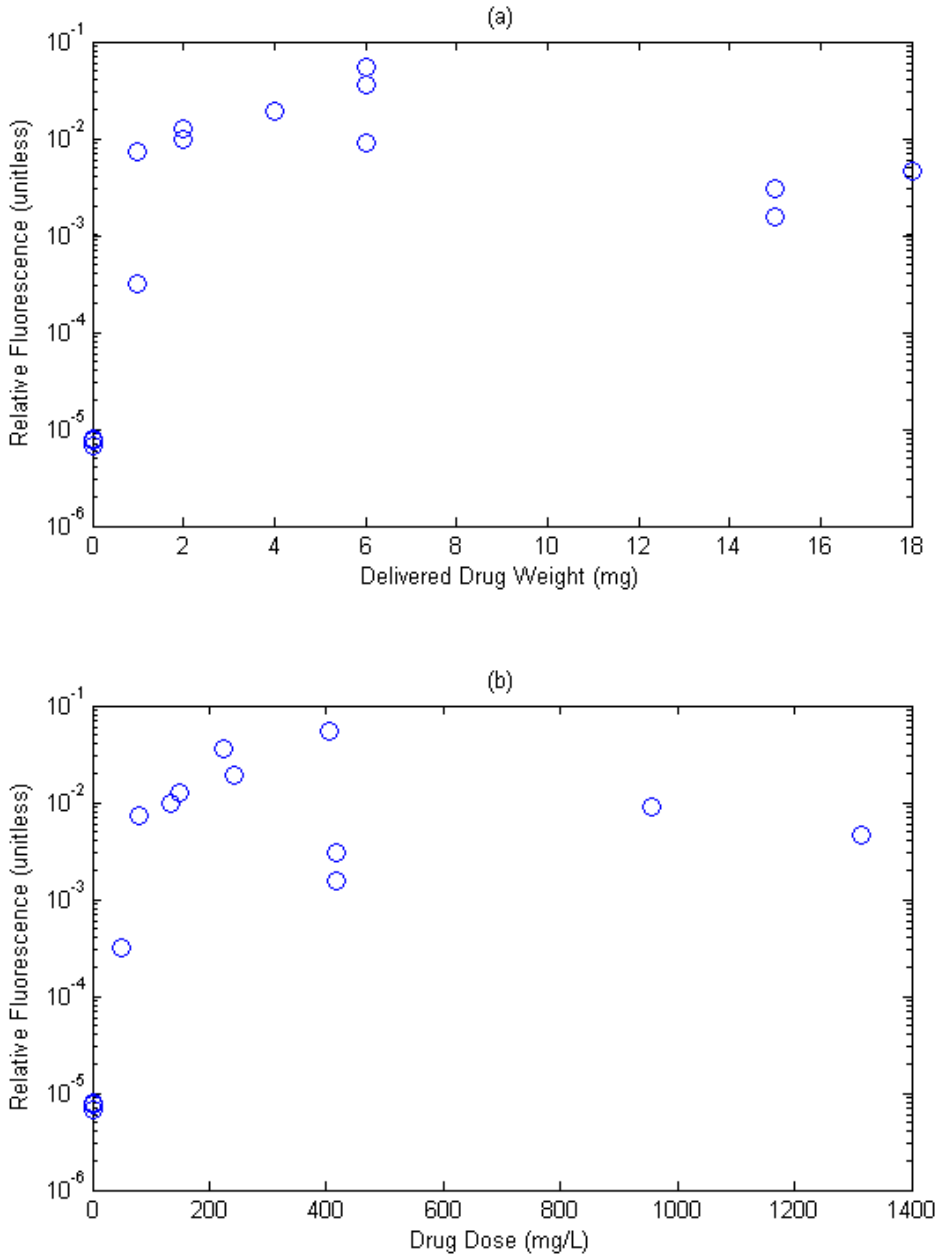

Figure 4.16: Comparison of relative fluorescence to (a) total delivered drug weight for the canine and (b) the drug dose in terms of total drug weight divided by prostate volume. This is for source-detector separation distance of 7.0 mm.

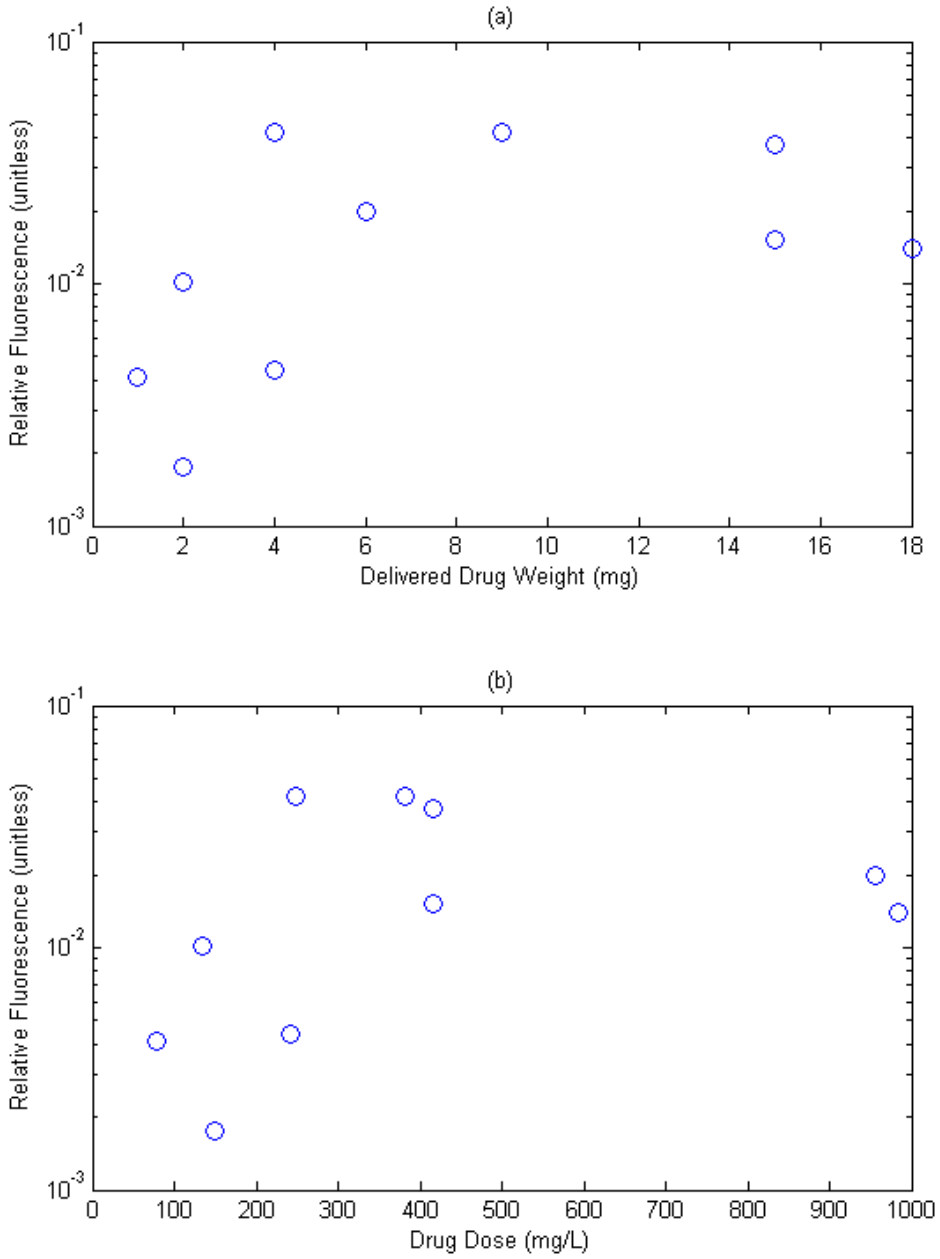

Figure 4.17: Comparison of relative fluorescence to (a) total delivered drug weight for the canine and (b) the drug dose in terms of total drug weight divided by prostate volume. This is for source-detector separation distance of 9.3 mm.

in the capillary beds. Such aggregation behavior would depend the dynamics of SL-052 going from a dissolved state in DMSO to an aqueous environment in blood. The size of the aggregates may depend on the rate of drug entering the bloodstream, the concentration of SL-052 in DMSO[1], the blood flow rate during injection and the size of the artery being injected into. In turn, this affects how and where these aggregates might get trapped. In addition, we are unfamiliar with the drug behavior post-aggregation, such as diffusion, deaggregation, or cellular uptake dynamics. With such complex pharmacokinetics, it is difficult to determine direct correlation between delivered drug dose and local prostate concentrations. Therefore, having no correlation between the relative fluorescence metric and drug weight or drug dose is expected.

Comparison between noise peak location and delivered drug weight or drug dose showed similar results as the comparison with relative fluorescence. No correlation is observed in this comparison. This is expected due to the strong correlation between noise peak location and relative fluorescence.

4.4.2 Absolute Excitation

For any given source-detector separation distance, the detected excitation counts should depend on drug concentration between source and detector. The lower the detected counts, the higher the drug concentration. Therefore, the absolute excitation should be another metric that may be used to measure prostate SL-052 concentration. Comparisons between absolute excitation and drug weight and drug dose for the four most common separation distances, 3.5, 6.1, 7.0 and 9.3 mm, are shown in figures 4.18, 4.19, 4.20 and 4.21 respectively.

[1]The concentration was not kept constant for this investigation. Instead, the total volume of DMSO was kept constant for varying drug weights

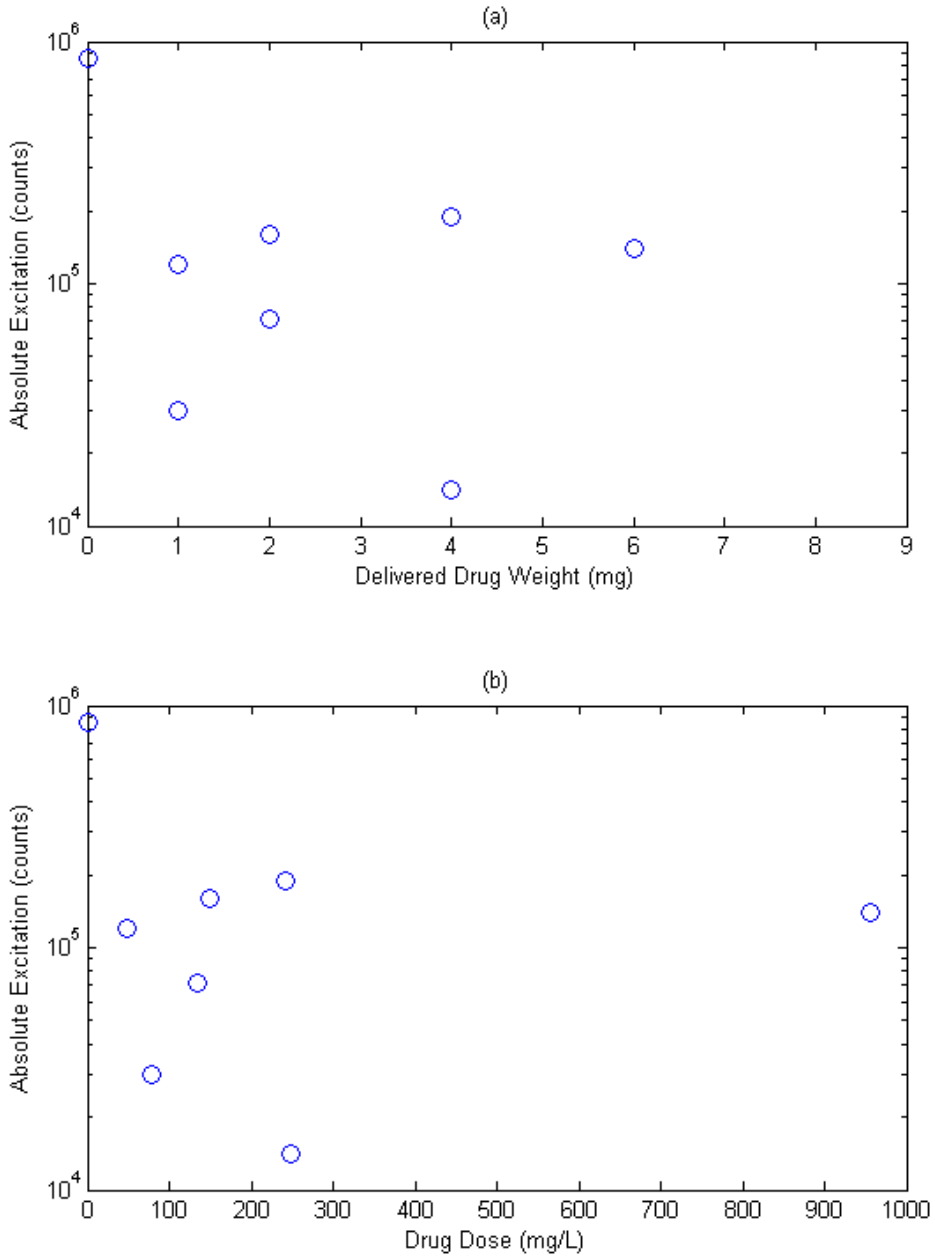

Figure 4.18: Comparison of absolute excitation to (a) total delivered drug weight for the canine and (b) the drug dose in terms of total drug weight divided by prostate volume. This is for source-detector separation distance of 3.5 mm.

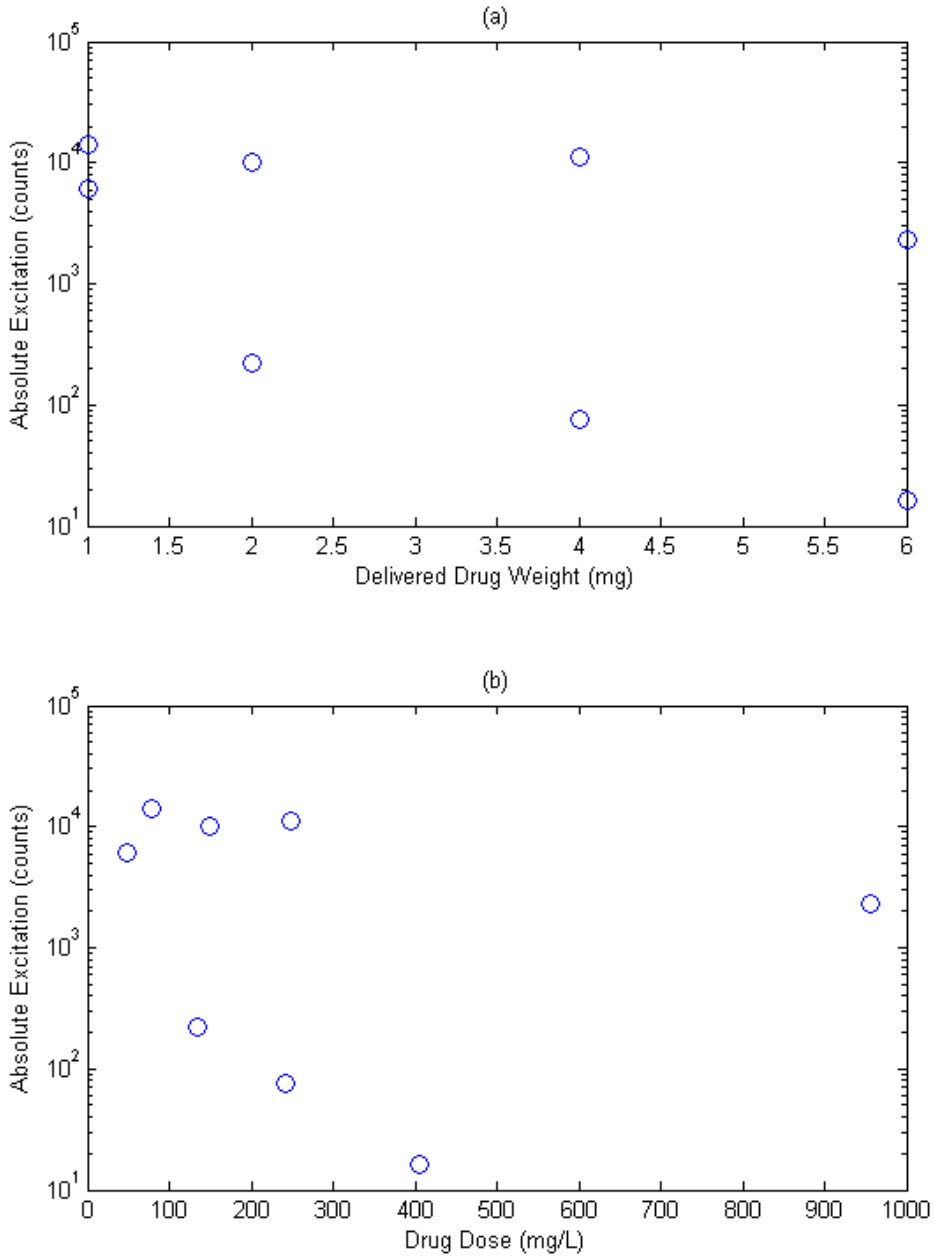

Figure 4.19: Comparison of absolute excitation to (a) total delivered drug weight for the canine and (b) the drug dose in terms of total drug weight divided by prostate volume. This is for source-detector separation distance of 6.1 mm.

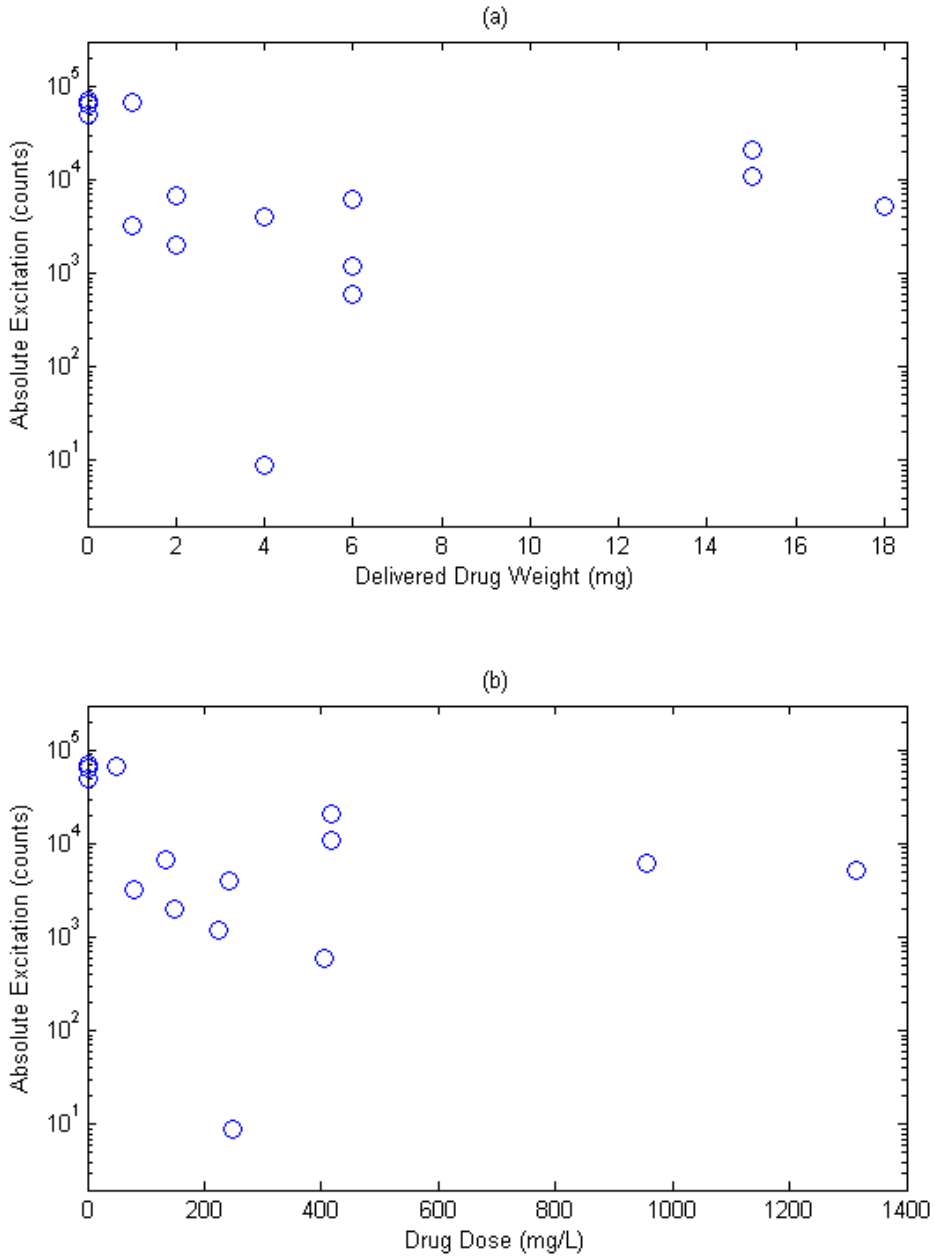

Figure 4.20: Comparison of absolute excitation to (a) total delivered drug weight for the canine and (b) the drug dose in terms of total drug weight divided by prostate volume. This is for source-detector separation distance of 7.0 mm.

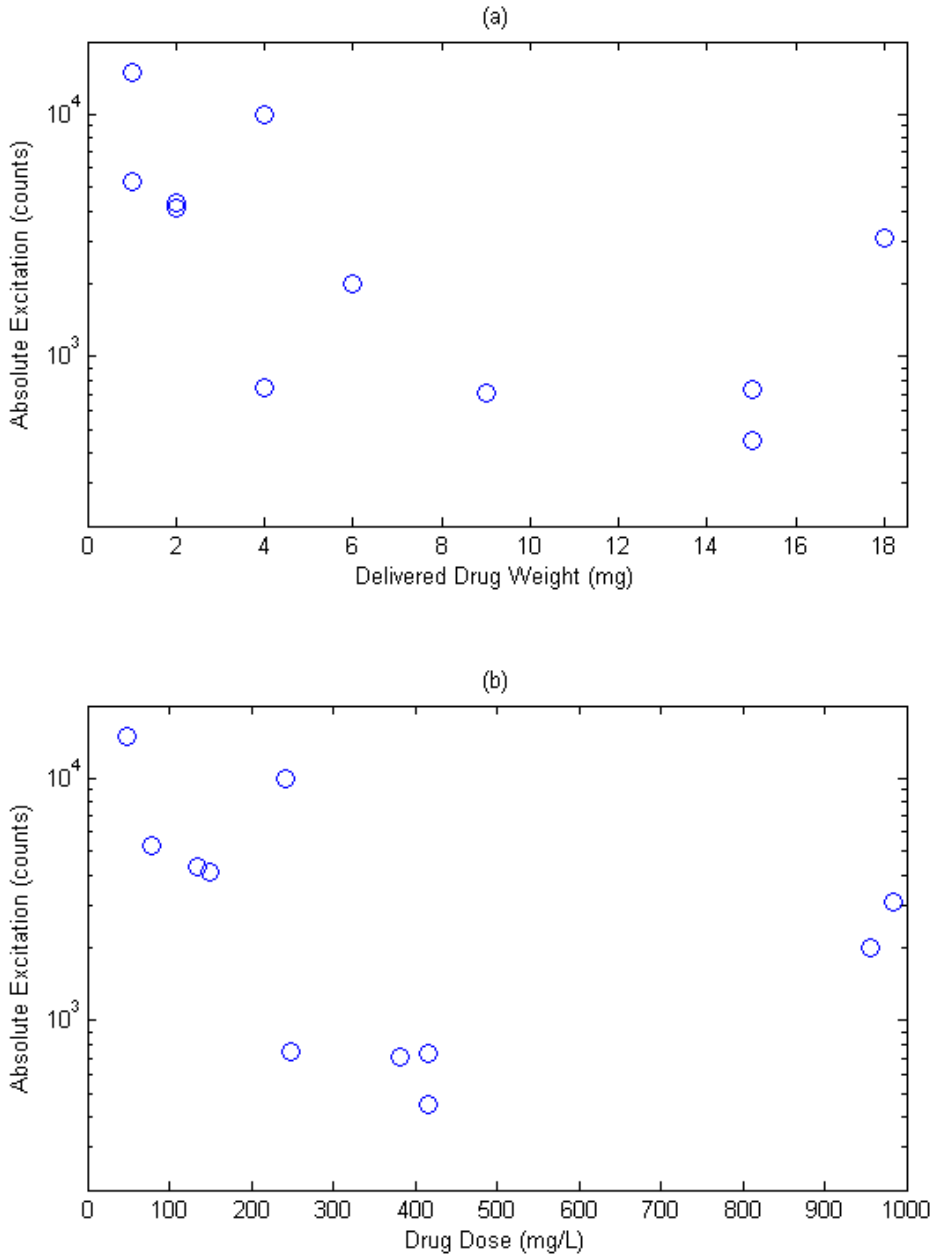

Figure 4.21: Comparison of absolute excitation to (a) total delivered drug weight for the canine and (b) the drug dose in terms of total drug weight divided by prostate volume. This is for source-detector separation distance of 9.3 mm.

Similar to the previous section 4.4.1, there is no strong correlation between the absolute excitation counts and delivered total drug weight or drug dose. The comparison with this simple metric (as opposed to the more convoluted metrics in the previous section), is further evidence that suggests that there is a highly dynamic drug distribution behavior and that the local drug concentration is solely dependent on total delivered drug weight or drug dose. It suggests that there may be various other factors that have not been accounted for.

4.4.2.1 Absolute Excitation Comparison with Calibration Table

The chaotic or variable nature of delivered drug versus optical metric for drug concentration has already been shown. This section examines that drug distribution within each prostate. More specifically, it examines if the drug distribution within each prostate is homogeneous. When canine absolute excitation data is compared against the reference data (calibration table) from section 3.5.1, the seemingly chaotic nature of drug distribution becomes more apparent. Figure 4.22 plots representative IA-DMSO canine absolute excitation overlaid on *in vitro* reference data. The plotted canine data sets are the ones with four available data points per prostate with each data point representing a different region in the prostate. The drug lines are the same as figure 3.20. The other ones have one or two and is therefore not useful for this comparison. The 4 data points from the light only control canine is the only one where all 4 data points are near[2] one line. This line is the zero drug line and this result is expected as the light only control prostate has zero drug. This agreement between *in vivo* and *in vitro* data reaffirms the reference data itself. All other canine data sets span across several drug lines and most

[2]The largest deviation is 0.24 orders of magnitude with average deviation of 0.13 orders of magnitude.

are more than an order of magnitude away from the closest line to all 4 data points. The data set that expresses the most homogeneous drug distribution is IA-DMSO-04 where all 4 data points are within half an order of magnitude away from the 7.6 mg/L drug line. However, overall, the data suggests an inhomogeneous drug distribution within the prostate.

An inhomogeneous prostate SL-052 distribution would further assert the suggestion that the pharmacokinetics for IA-DMSO delivery of SL-052 is dependent on various factors that were not taken account of for this canine investigation. These factors have already been discussed in section 4.4.1.

4.4.3 Time-Independent Discussions

The pre-PDT state of the prostate is examined in this section by assessing the detected optical spectra for the first cycle of the canine experiments. The purpose is to determine possible metrics to optically determine prostate drug concentration and improve understanding of SL-052 pharmacokinetics. Absolute excitation is a known and obvious metric where at a given source-detector separation distance, the higher the SL-052, the lower the observed absolute excitation. Canine absolute excitation assay suggests inhomogeneous SL-052 concentrations within each prostate and that the *in vivo* drug concentration is not highly dependent on delivered drug weight/dose for IA-DMSO canines. Relative fluorescence was another metric examined. The greater the drug concentration, the larger the fluorescence-to-excitation ratio should be. Location of autofluorescence noise peak was also examined. This peak red-shifts due to the transmission profile of SL-052. The higher the SL-052 concentration, the greater the red-shift. Comparison between these two metrics showed excellent correlation between them for all canine data and improves the validity of the

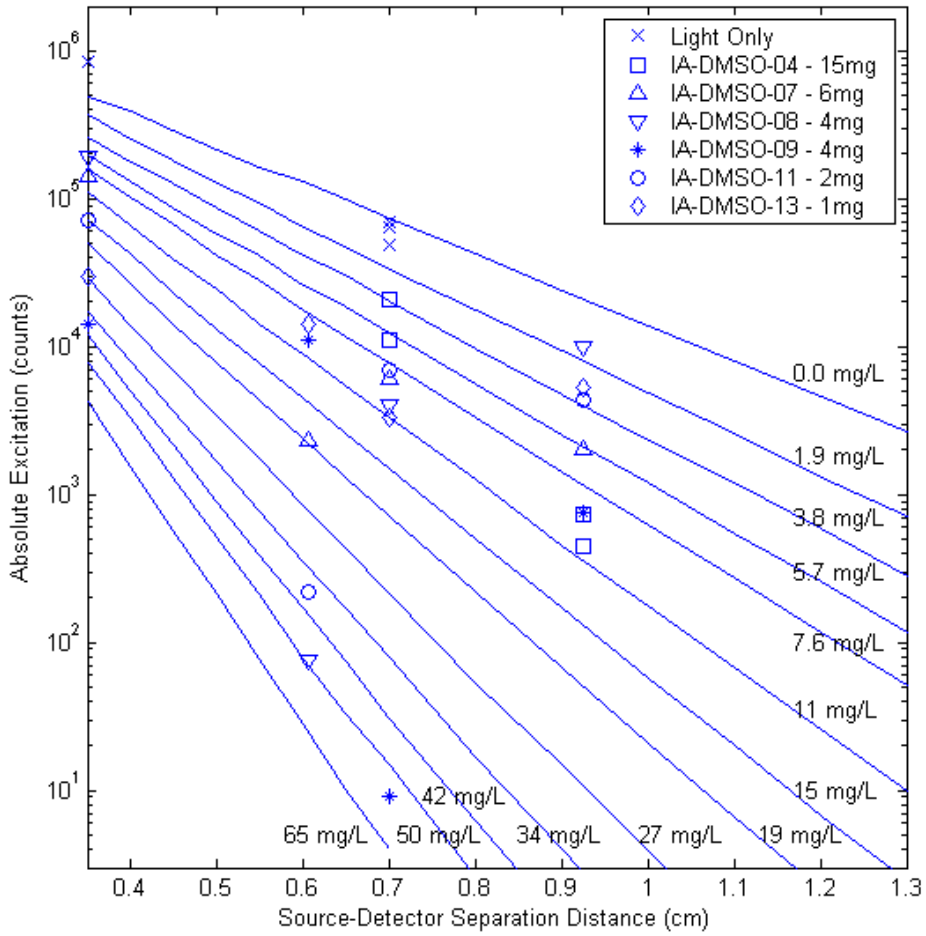

Figure 4.22: Canine absolute excitation data overlaid on *in vitro* experiment reference data.

metrics themselves. Both metrics showed poor correlation with delivered drug weight or drug dose, again suggesting the *in vivo* drug concentration is not highly dependent on delivered drug weight/dose for IA-DMSO canines.

All time-independent evidence suggests a highly dynamic SL-052 pharmacokinetics for IA-DMSO drug delivery[3] due to poor correlation with delivered drug weight or drug dose. However, there is one significant source of error that should be accounted for: fiber placement. Although the template was used to guide ALN placement and that during placement ALN contains a metal obturator stencil to maintain straightness, there may still be placement errors from prostate stretching/compressing causing flex to ALN after removal of stencil. Bent ALN are reflected as errors in source-detector separation distance. From figure 4.22, a placement error of 1 mm can affect absolute excitation by up to 0.5 orders of magnitude. However such large placement error is unlikely with the template in place. In addition, fibers suspected of having placement errors are recorded in experiment notes. The same analysis has been performed with those data points removed and results were unaffected. The data still suggested a highly dynamic SL-052 pharmacokinetics that is not highly dependent on delivered drug weight/dose.

This strong evidence that suggests inhomogeneous SL-052 distribution and poor correlation with delivered drug weight/dose provides good motivation for the need for a minimally invasive method to determine actual local SL-052 concentrations post drug delivery. Therefore, it is important for the continued use of our optical detection instrumentation to measure local prostate drug concentration at the onset of light delivery. This allows for a customized light treatment tailored for the specific drug distribution and may improve

[3]Insufficient data points were available for the IV-Liposome and IA-Liposome canines because the main primary direction of this study is to concentrate on IA-DMSO mode.

treatment efficacy in future investigations.

4.5 Time-Dependent Investigation

This section discusses observed results over the course of the entire treatment. It considers trends in data extracted over time with the purpose of gaining insight to the changes in the state of the prostate as treatment progresses.

4.5.1 Overall Change Over Time

Monitoring treatment progress by optically monitoring change over time is not a novel concept. There are many factors which may cause optical changes over time. Photochemical reactions rapidly consume oxygen and because deoxy-hemoglobin (Hb) absorbs more 635 nm excitation light than oxy-hemoglobin (HbO_2), there might be an overall decrease in transmission of excitation light leading to a decrease in detected absolute excitation and fluorescence over time. On the other hand, because SL-052 is highly absorbing, any bleaching or clearing away of drug will manifest as an increase in detected absolute excitation with a decrease in fluorescence. The total blood flow may also have an impact. An increase in blood flow would result in more hemoglobin absorption and decrease both absolute excitation and fluorescence, while a decrease would cause the opposite. There could also be bleeding around the ALN causing decreased absolute excitation and fluorescence. In particular to SL-052 IA-DMSO mode, deaggregation of aggregated drug may lead to decreased excitation with increased fluorescence.

The basis for comparing overall change over time will be to compare final

	Increase (%)	Neutral (%)	Decrease (%)
Absolute Excitation	54	15	31
Absolute Fluorescence	0	31	69
Relative Fluorescence	15	23	62

Table 4.2: Overall changes over treatment time for IA-DMSO mode in canines prostates. The values are expressed as % of total in that bracket. Available data points: $n = 26$.

absolute excitation, absolute fluorescence and relative fluorescence values at the end of treatment with their initial values at the onset of light delivery. The data is divided into three groups: increase, decrease, and neutral. The average change in absolute excitation for the light-only control is 14% with maximum change of 25% for one data point. The division point between the three groups is set at 28%, double the light-only control average; that is, any change over time between +28% and -28% is considered neutral with above and below grouped into increase and decrease groups respectively.

The overall changes are summarized in table 4.2 for IA-DMSO mode. The majority of the data shows a trend with increase in absolute excitation, decrease in absolute fluorescence, and decrease in relative fluorescence over the course of the treatment. The only factors mentioned above that would be consistent with this result would be a bleaching or clearing away of the highly absorbing SL-052 over time. From figure 3.20, we know that SL-052 can cause significant changes to tissue optics. Therefore, it is plausible that the clearing or bleaching of SL-052 may be the dominant factor for the overall change over time. For IV-Liposome and IA-Liposome modes, there is an insufficient number of data points for this type of analysis.

Figures 4.23, 4.24, 4.25 shows examples of the overall changes over time for absolute excitation, absolute fluorescence, and relative fluorescence respectively. Notice there are two very different types of trend plots, one with lines con-

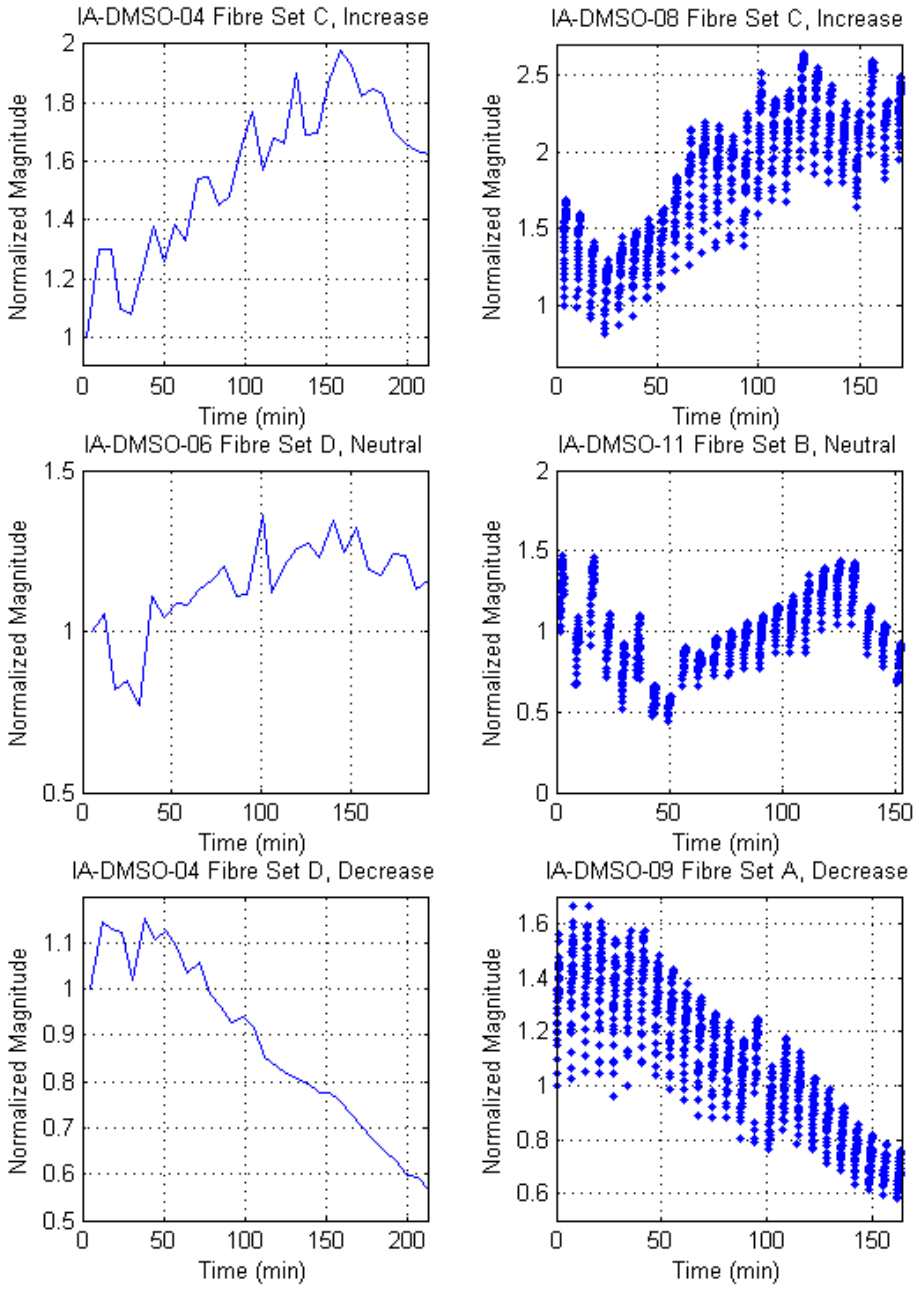

Figure 4.23: Detected absolute excitation signal over time normalized to first data point showing examples of increase, neutral, and decrease trends.

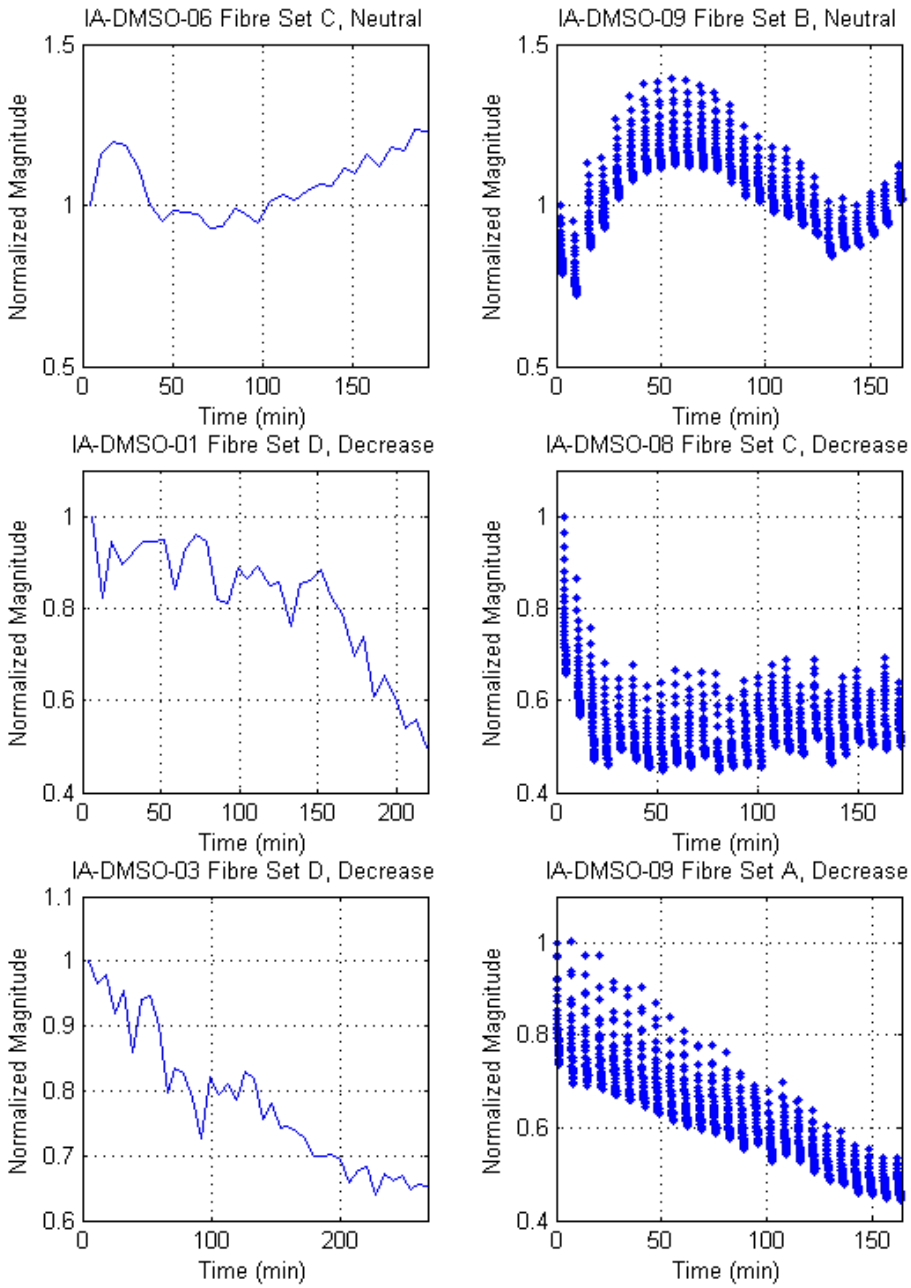

Figure 4.24: Detected absolute fluorescence signal over time normalized to first data point showing examples of neutral, and decrease trends. There were no increase examples

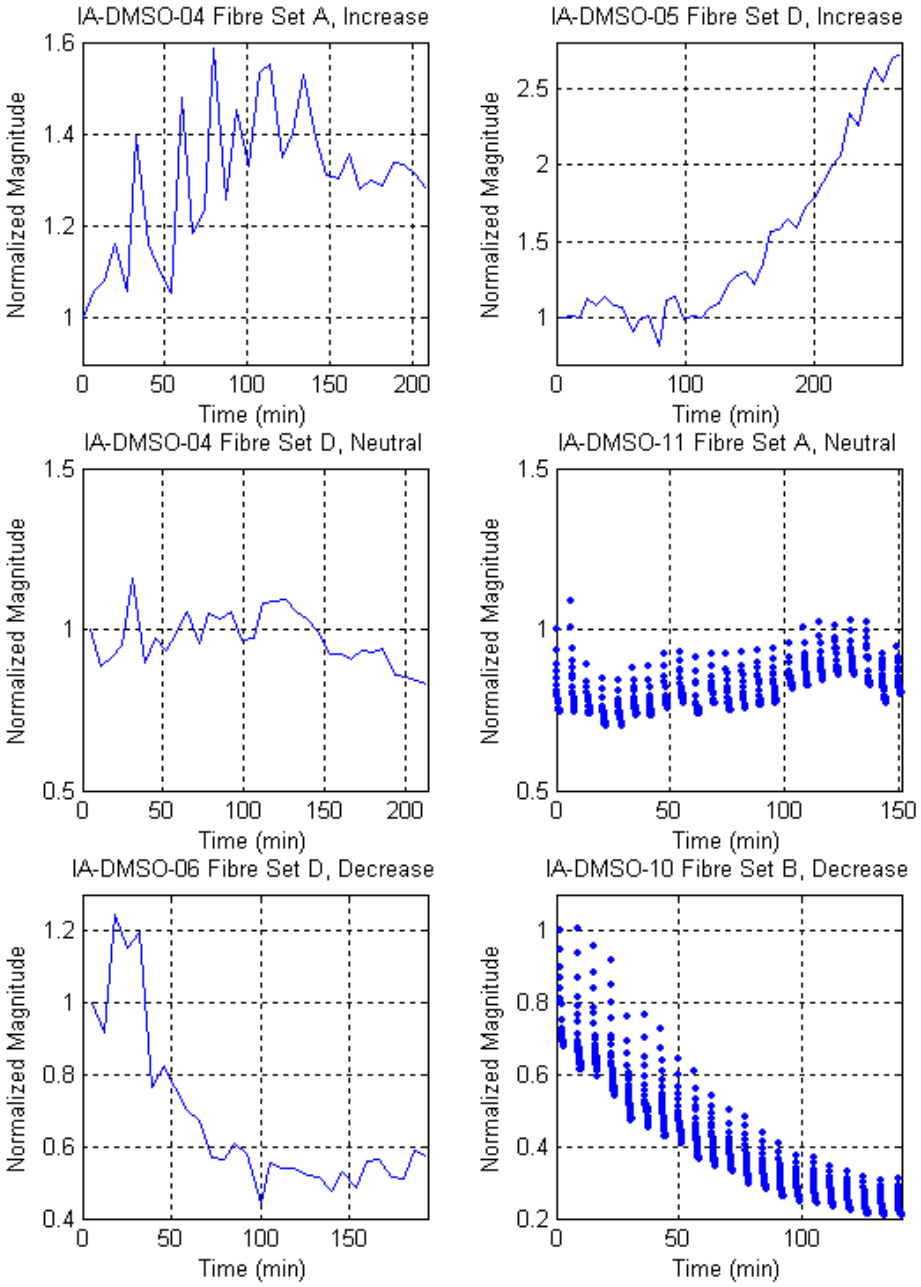

Figure 4.25: Relative fluorescence signal over time normalized to first data point showing examples of increase, neutral, and decrease trends.

nection each point, one point per light-on sub-cycle, and one with multiple data points per light-on sub-cycle plotted as dots. An improvement to the optical detection method was made beginning from canine IA-DMSO-07. As described in section 3.4.2, manual spectrometer detection was converted to automatic detection, greatly improving detection resolution in time. This change was made because I observed noticeable changes in the spectra during each light-on sub-cycle. The automatic detection allowed for approximately 15 to 50 data points (depending on integration time) during each $100s$ sub-cycle whereas manual detection only had 1. These examples showed that there is an oscillatory behavior between the light-on and light-off sub-cycles. This is the topic of discussion for section 4.5.2.

4.5.1.1 Integrating Sphere Detection in Canine Model

The initial iteration of the light delivery and detection system utilized an integrating sphere as one of the methods for monitoring excitation light over the course of the treatment. As tested on rat models (see section 4.1.5), there was sufficient light for integrating sphere detection through the unused delivery fibers. However, for the canine model, we found there was insufficient excitation light detected using this method. The integrating sphere only detected powers on the order of a few nW, a signal strength that is on par with the dark signal. Therefore, the integrating sphere detection was removed in newer iterations of the detection protocol (see section 3.4.2).

4.5.2 Oscillatory Behavior in Detected Excitation and Fluorescence

Thus far, we have not mentioned much about photobleaching of SL-052 with IA-DMSO delivery method. Because SL-052 is lipophilic, we expect the drug to aggregate and form temporary embolized states once administered into blood serum. *In vivo* photobleaching characteristics of SL-052 in this state has never been measured. It would be inappropriate to apply photobleaching characteristics from SL-052 in solution as a solution form might allow much greater SL-052 mobility and diffusion than an aggregated and possibly embolized state. Photobleaching in solution would produce an averaged photobleached state as drug is allowed to evenly distribute in solution. However, in a low mobility medium, photobleaching may occur locally before sufficient drug redistribution can take place. Only when sufficient time has elapsed, diffusion or some other process may carry functional drug back into the depleted region. Because we do not know the mobility of IA administered SL-052, we cannot make predictive photobleaching estimations.

Oscillations in spectra characteristics were observed in all canines that underwent IA-DMSO SL-052 administration modality. However, for IV-Liposome and IA-Liposome modes, no oscillations were observed. Figure 4.26 depicts typical plots of temporal change in observed 635 nm excitation intensity for one fiber set. Sub-figure (a) shows overall change in absolute excitation over the entire light delivery phase of iPDT. The 635 nm absorption decreases during the first 2 hours of treatment allowing higher transmission of excitation light. Approximately 2.5 hours into treatment, 635 nm absorption increases. This particular fiber set showed an overall neutral change when comparing transmission at end of treatment versus the beginning.

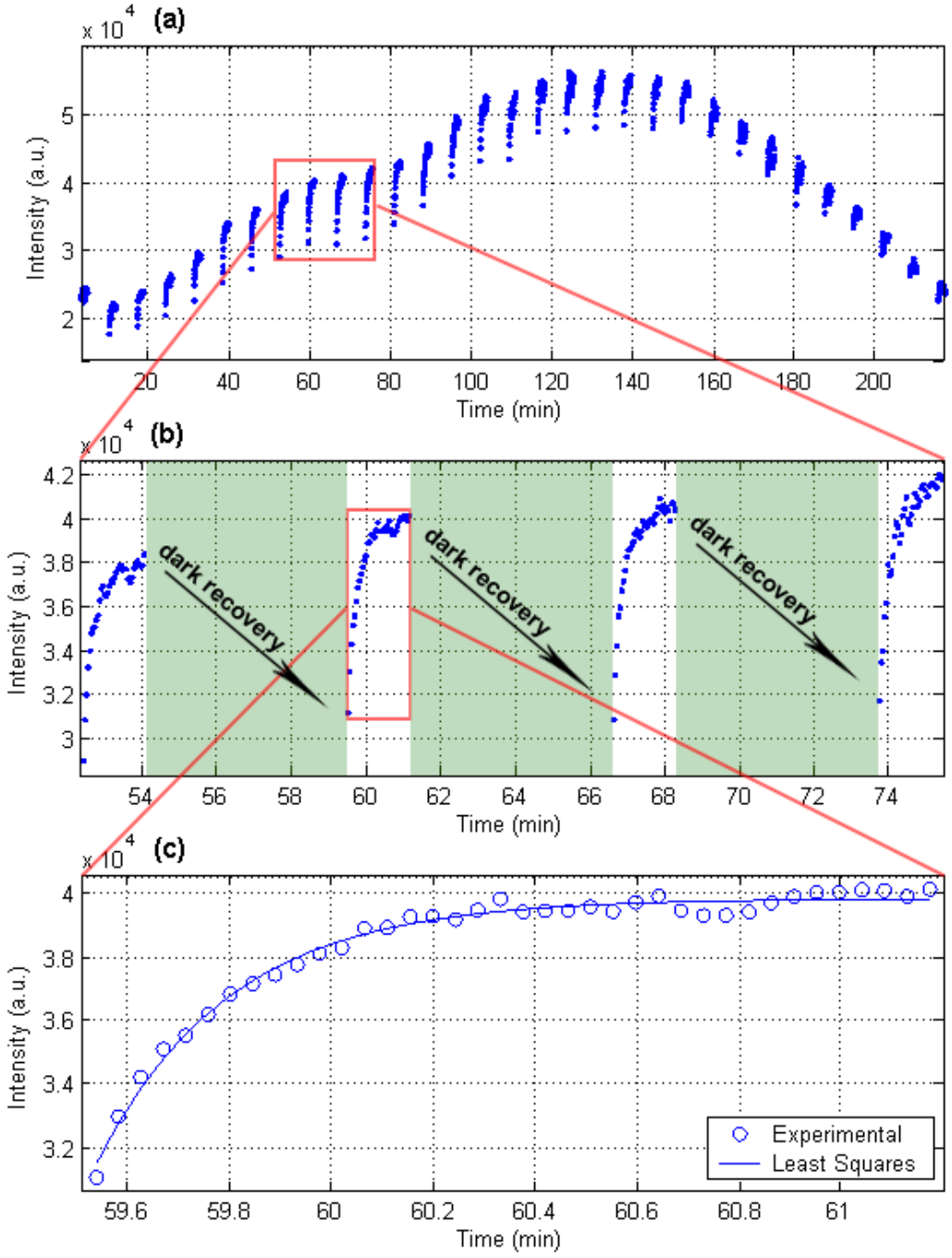

Figure 4.26: Typical detected 635 nm absolute excitation intensities over time at different magnifications.

Figure 4.26(b) shows a magnified segment of the temporal change in excitation intensity. It illustrates a typical intra-cycle and inter-cycle change in absorption of excitation light for time-fractionated iPDT with IA delivered SL-052. The figure exemplifies unique characteristic changes in absorption during light-on versus changes during light-off phases. The shaded regions indicate where this particular fiber set is switched to the off state. Data for each fiber set is only available when that set is switched to the on state. When the fiber set is first switched on, transmissivity increases rapidly but the rate of increase diminishes over the 100 second sub-cycle showing an exponential like decay. There is no data during the off phase but at the onset of the next on phase, the detected 635 nm intensity has partially recovered from exponential change in the previous on phase suggesting a light induced absorption change followed by a dark phase recovery mechanism.

Least squares data fitting is similar to that used by Ericson[76] except the detected intensity is time dependent rather than fluence dependent. Equation 4.2 is the mono-exponential decay model for the observed change in intensity over time where f is the measured intensity for either excitation or fluorescence, a_0 is a constant representing base level of detectable excitation or initial level of fluorescence, a_1 is a scaling constant representing the magnitude to which changes in photosensitizer concentration would have on detected light, t is time, and t_0 is the characteristic time constant for decay. This relationship is expected since the rate of photobleaching, or rate of change of the concentration of functional photosensitizer, should be proportional to the concentration of functional photosensitizer available to be photobleached. An exponential relationship is the solution to such a differential equation. Curve fitting is performed with MATLAB's *fminsearch* multidimensional unconstrained nonlinear minimization function.

$$f(t) = a_0 + a_1 exp(-t/t_0) \tag{4.2}$$

Figure 4.26(c) is a further magnification exemplifying the exponential relationship showing the least squares fit to an exponential function from equation 4.2 on top of raw data. The experimental data shows excellent agreement with equation 4.2.

Figure 4.27 depicts typical temporal change in 815 nm SL-052 fluorescence from the same treatment and fiber set as figure 4.26. Sub-figure (a) shows overall change in absolute fluorescence intensity over the entire light delivery phase of iPDT. The fluorescence holds relatively steady in the first 1.5 hours of treatment before declining steadily in the remaining 2 hours. This particular fiber set showed an overall decrease type change when comparing fluorescence at end of treatment versus the beginning.

The intra-cycle and inter-cycle change in SL-052 fluorescence is exhibited in figure 4.27(b). Again, the shaded regions indicate the fiber set dark phases. The oscillatory trend is the opposite to that of 635 nm transmission in figure 4.26(b). When the fiber set is illuminated, fluorescence decrease with a decaying exponential trend. During the dark phases, there is recovery from the on state decay, again suggesting a light induced change and dark phase recovery mechanism.

Figure 4.27(c) is the least squares fit of the exponential relationship in equation 4.2 showing the trend behaves exponentially.

The least squares fit of the exponential relationship in equation 4.2 was applied to all experimental data and the statistical ensemble of characteristic decay time constants t_0 show a normal distribution for both excitation and

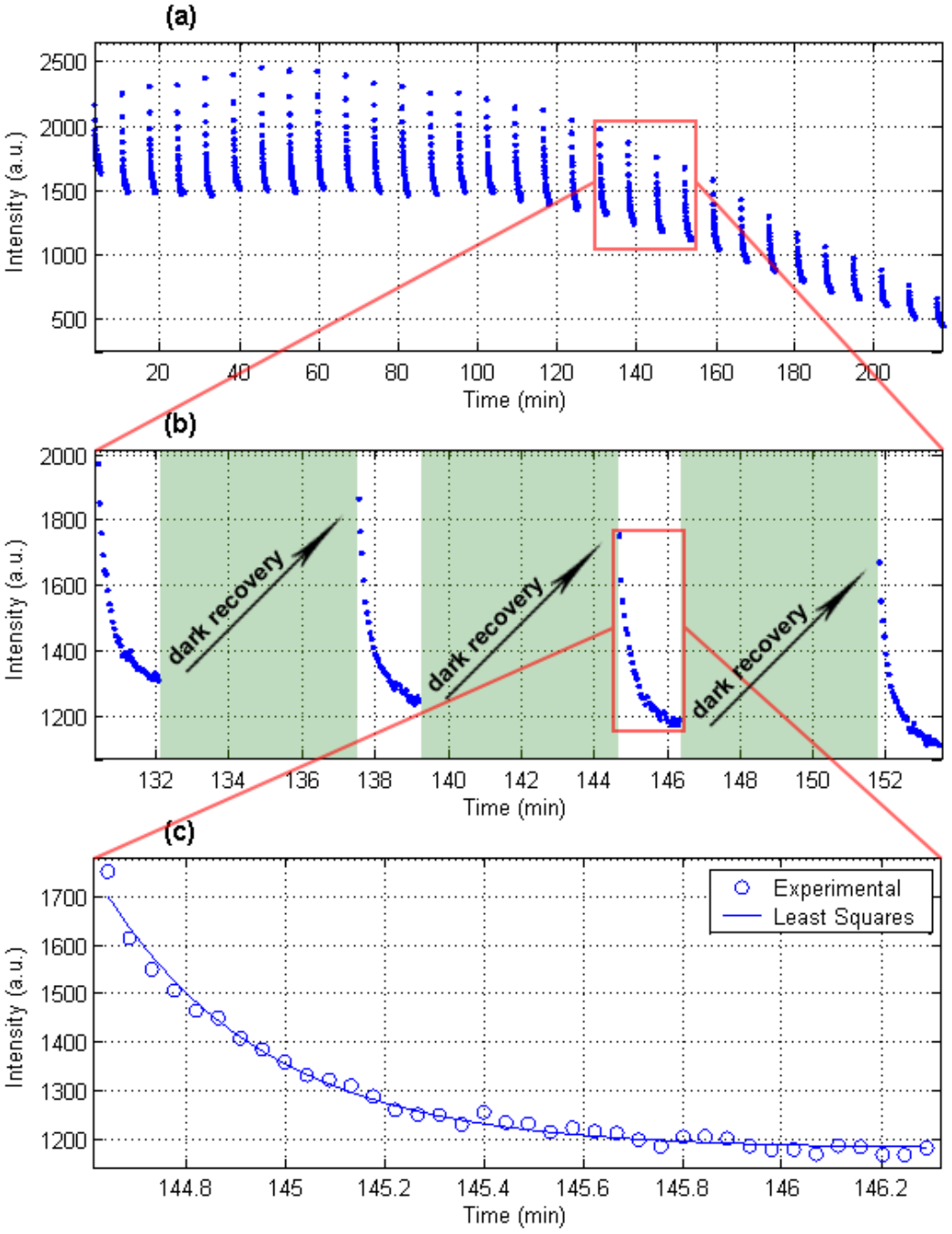

Figure 4.27: Typical detected 815 nm absolute fluorescence intensities over time at different magnifications.

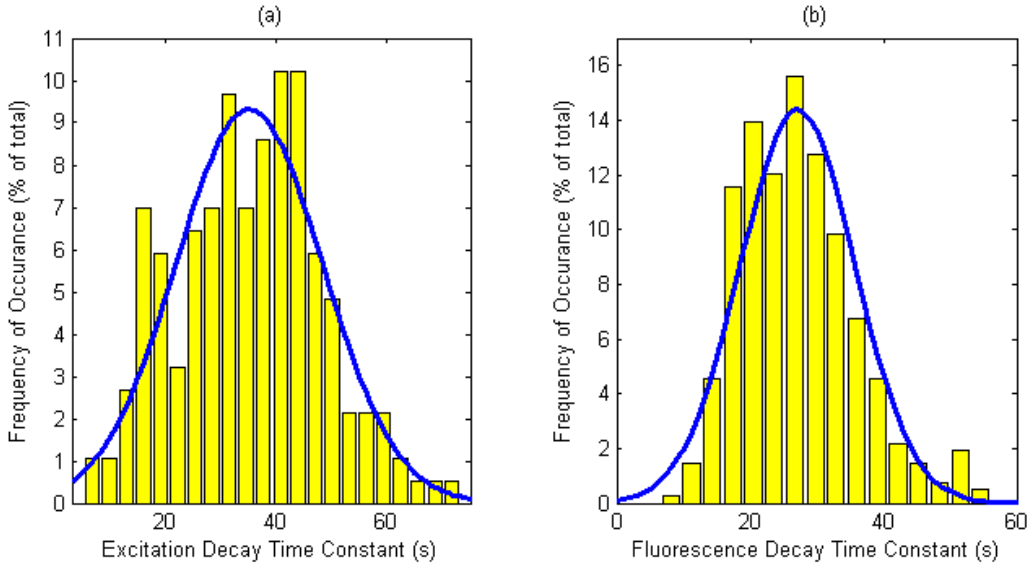

Figure 4.28: Statistical distribution of characteristic decay time constants (t_0) for the exponential change during light-on phases. (a) The distribution for 635 nm absolute excitation decay time constant has mean of 35s and standard deviation of 13s. (b) The distribution for 815 nm absolute fluorescence decay time constant has mean of 27s and standard deviation of 8.6s.

fluorescence data. The mean time constant for 635 nm excitation is 35s, with standard deviation of 13s. The mean time constant for 815 nm fluorescence is 27s, with standard deviation of 8.6s. Figure 4.28(a) and (b) show the distribution of decay times for excitation and fluorescence respectively with superimposed Gaussian profiles.

4.5.3 Time-Dependent Discussions

Overall trend over time show results with increasing excitation light transmission coupled with decreasing SL-052 fluorescence. Various factors affect overall changes in excitation light transmission and drug fluorescence, but we have argued that the factor most consistent with this behavior is an overall bleaching or clearing of SL-052 from the prostate. Upon examination of the oscillatory behavior in detected excitation and fluorescence, we may see further evidence

to support this.

Up to this point, not much discussion has involved time-fractionated light delivery. In review, light delivery occurs in cycles of $100s$ light-on and $300s$ light-off periods. The purpose of this is to allow for reaccumulation of exhausted reactants and has been discussed in section 3.1. Through time-fractionated light delivery protocol of iPDT of intra-arterially administered SL-052 photosensitizer in canine prostates, we observed unique spectral oscillations during light-on and light-off phases. For photosensitizer fluorescence, we observed that during the light-on phases, fluorescence quickly decayed. However, the decay is not permanent, and over the course of the dark phase, the fluorescence would oscillate back and partially recover in intensity. The dark phase change is inferred from the initial fluorescence intensity of the next light-on phase. The changes in detected excitation light shows the opposite oscillatory behavior. During the light-on phases, detected excitation light increases but would partially recover and decrease during the dark phases. This would mean a fast decrease in excitation light absorption during illumination and an increase during dark phases.

There seems to be two competing effects that is manipulated by the excitation light. To the best of our knowledge, this is the first time such effects has been reported for iPDT. One possible explanation is SL-052 photobleaching and recovery from non-photochemical mechanism such as redistribution. SL-052 is a strongly absorbing chromophore at 635 nm. A fast decrease in fluorescence coupled with a fast decrease in absorption of excitation light during light-on phases is a strong indicator for photobleaching since the removal of active drug would reduce fluorescence as well as 635 nm absorption. Redistribution of drug may occur through multiple mechanisms. Because the photosensitizer

is expected to be in aggregated in this IA-DMSO administered modality, it is conceivable that drug perfusion is much slower than in IV delivery protocols. If this is the case, then we may be seeing for the first time a quantifiable rate of SL-052 redistribution in vivo via IA delivery. This redistribution would bring functional drug to the irradiated region allowing for recovery of fluorescence as well as 635 nm absorption. Another possibility is a slow deaggregation of drug. Aggregated drug could result in self-shielding effects where SL-052 at the center of the aggregate no longer participates in photochemical interactions. In this case, deaggregation would reveal more functional drug to the irradiated region. A third possibility is that the photobleaching is reversible or non-destructive; that is, the drug is induced to a state where it is temporarily non-functional. The recovery from this temporary state may lead to the recovery of the excitation and fluorescence signals.

Because the photochemical reaction consumes oxygen, and Hb has higher 635 nm absorption coefficient than HbO_2, we expect an increase in excitation light absorption during light-on phases if no photobleaching is present. However, we see the opposite effect, implying that the process causing the decrease in absorption dominates over optical effects caused by Hb and HbO_2 exchange. The deoxygenation of hemoglobin would not have much effect on 815 nm fluorescence as this wavelength falls on the isosbestic point of Hb and HbO_2.

Light on decay curves closely resemble exponential form of equation 4.2 suggesting a functional relationship where the rate of change of intensity is dependent on the intensity itself. This evidence additionally suggest photobleaching is the cause for the fast light-on changes as the rate of change of photosensitizer concentration should be proportional to the concentration of available

photosensitizer. Furthermore, statistical analysis of these light-on decay curve time constants t_0 show a normal distribution centered about $35s$ for 635 nm excitation intensity and $27s$ for 815 nm fluorescence intensity. These may be the nominal decay times for our drug concentration ranges at our fluence rate for iPDT with IA SL-052 administration. The distribution for 635 nm decay time is more noisy and has a larger standard deviation compared to the 815 nm decay time. This is expected if SL-52 photobleaching is assumed to be the cause of the fast light-on exponential change. Because the photosensitizer is not the only chromophore, the change in 635 nm signal due to changes in drug concentration might be subject to noise from other changes such as variations in tissue oxygenation. The 815 nm fluorescence signal contribution is affected to a much less by deoxygenation of hemoglobin as 815 nm is at the isosbestic point of Hb and HbO_2.

4.5.3.1 Implications to Time-Fractionated Light Delivery

The observation of unique spectral characteristics of fast illumination phase change followed by dark phase recovery directly supports the use of time-fractionated light delivery. If the recovery is caused by redistribution of functional drug into the local excitation site or by deaggregation of drug aggregates, then time-fractionation allows for repopulation of photobleached regions allowing for higher instantaneous photodynamic dose. Even if the mechanism for dark phase recovery is not from redistribution or deaggregation of SL-052, but from some other unknown mechanism, the recovery still indicates a possible improved efficacy from time-fractionation. The exponential decay in the rate of change during the illumination phase suggests a decrease in instantaneous photodynamic dose because the incremental treatment is causing less and less

observable optical change in tissue. This could indicate a reduction in photodynamic effect as the illumination is altering the tissue at slower rates as time of continuous illumination increases. In both cases, the evidence suggest PDT efficacy may be improved by time-fractionation and motivates further investigation and use of this light delivery method.

Chapter 5

Conclusion

Interstitial photodynamic therapy was performed using a novel photosensitizer and a new light delivery and detection system. This thesis encompassed the entire process of instrumentation development from characterization of the photosensitizer SL-052, to design and integration of the treatment system for the unique characteristics of SL-052, to creation of an optical phantom and *in vitro* testing of the system in the phantom, and finally to *in vivo* experimentation of iPDT with real-time spectral monitoring.

5.1 Photosensitizer SL-052

A novel photosensitizer, SL-052, was optically characterized to determine feasibility for use as a photosensitizer. The drug is determined to have a wide absorption profile with a FWHM of 146 nm between 548 and 694 nm. Absorption peaks at 657 nm; however, the peak is rather flat, holding 90% of maximum value within the range between 618 and 673 nm. The absorption

profile allows excitation within a wavelength range that is commercially available with robust, high powered, solid state diode lasers suitable for clinical settings for iPDT. In addition, it can be excited at wavelengths $> 650\ nm$ allowing for greater tissue penetration depth, making this photosensitizer highly suitable for PDT of large volumes.

SL-052 also exhibits light-induced fluorescence when excited at 635 nm. This property further enhances its appeal for use in PDT and greatly reduces the instrumentation cost and complexity when fluorescence based dosimetry is applied. SL-052 fluorescence under 635 nm excitation has spectra similar to that of hypocrellin-B derivative. The region of the fluorescence profile utilized for dosimetric purposes is around 815 nm where the spectra is outside of self-shielding effects and at the isosbestic point of Hb and HbO_2. This reduces the dependency of the fluorescence emission on these factors.

There are a few areas suitable for future investigation. Because the excitation light source wavelength of 635 nm was determined by the drug supplier, testing at longer wavelengths with higher tissue penetration depths was never performed. Examination of SL-052 at longer wavelengths should be performed with special attention to tissue penetration, therapeutic effect, and fluorescence. In addition, the quantum efficiency for singlet oxygen production and for fluorescence emission could also be determined to further understand the photophysical properties and SL-052.

5.2 Light Delivery and Detection System

A switched light delivery and detection system was designed to exploit the unique photophysical properties of photosensitizer SL-052. The system uti-

lized time-fractionated light delivery with continuous real-time spectral detection for dosimetric purposes. 635 nm therapeutic light is delivered to multiple fiber coupled cylindrical diffusers through a computer controlled fiber optic switch allowing for multi-focal irradiation as well as feedback detection from the diffusers. A computer controlled spectrometer monitors 380-1050 nm continuously and LabVIEW software extracts and records excitation and fluorescence counts in real-time allowing for real-time monitoring of treatment progress. Each hardware component is characterized and tested to ensure functionality during treatment and to minimize equipment noise. Software is designed with multiple levels of safety margins to ensure successful treatment. The easy-to-use graphical user interface allow operation by non-technical personnel.

Future considerations should include utilizing dosimetric detection information to change light treatment parameters in real-time. The laser modules can be computer controlled and therefore light output at different treatment zones can be adjusted depending on detected treatment progress or local photosensitizer concentrations. For permanent clinical use of the treatment system, it would be beneficial to consider rack mounting each instrument to enhance robustness. A comprehensive enclosure should greatly reduce the need to reconnect fiber optic components and therefore reduce light losses from fiber tip degradation.

5.3 Optical Phantom

Based on diffusion theory principles, an intralipid methylene blue optical phantom was created to mimic the optical properties of canine prostate. The determined parameters for the phantom were 18.2% by volume of 10% in-

tralipid and 2.245 mg/L of methylene blue which has absorption coefficient of $\mu_a = 0.73cm^{-1}$ and $\mu_s' = 22.7 \pm 0.5cm^{-1}$. This allowed for *in vitro* testing of light delivery and detection system including generation of the calibration table for SL-052 concentrations at varying source-detector separation distances based on transmitted excitation light.

Because of the limited availability of SL-052, the drug fluorescence was never characterized in the calibration table. For future investigations, it would be worthwhile to include fluorescence information into the calibration table. In order to achieve this, the phantom's absorbing agent, methylene blue, must be changed to one with less fluorescence such that its fluorescence does not interfere with SL-052 fluorescence. A suggestion would be to use India ink.

5.4 *in vivo* Investigations

SL-052 mediated interstitial photodynamic therapy was performed on Dunning rat tumor models as well as canine prostates. The rat investigation clearly showed that the switched light delivery system was effective at delivering excitation light to induce photodynamic action in rats administered with SL-052.

The spectrometer detected canine raw spectra showed SL-052 fluorescence in IA-DMSO mode but no clear fluorescence was observed for IV-Liposome or IA-Liposome modes. Spectrometer detected 635 nm excitation light intensity could be easily extracted in real-time and proved to be more sensitive than integrating sphere detection.

Time-independent investigation showed 3 possible metrics for determining local SL-052 concentration: Absolute excitation, relative fluorescence, and wave-

length location of noise peak. The diffuser autofluorescence noise became utilized as a broadband source and characteristics from this diffuse transmitted light can be use for dosimetric purposes. The current draw back is that no direct measurement of local drug concentration is available to evaluate the metrics. Future investigation should include comparing these metrics with drug concentration determined from excised tissue to evaluate their ability to optically determine local SL-052 concentrations. Comparing with the calibration table, there was no observed correlation between delivered drug weight/dose and absolute excitation. There was significant variation between zones within the same canine prostate suggesting inhomogeneous SL-052 distribution and a highly dynamic pharmacokinetics for IA-DMSO mode. This supports the need for future investigations to study SL-052 pharmacokinetics and determine actual drug concentration in prostate tissue. This evidence also encourages the continued use of optical detection instrumentation to non-invasively measure local drug concentration at the onset of light delivery.

Time-dependent investigation showed trends in overall change of increasing absolute excitation, decreasing fluorescence and decreasing relative fluorescence. The evidence suggests that the bleaching or clearing away of SL-052 dominates the optical changes *in vivo* for IA-DMSO mode. Never before seen oscillatory behavior in detected excitation and fluorescence was observed using the fast automated spectrometer detection system during time-fractionated light delivery. For photosensitizer fluorescence, we observed that during the light-on phases, fluorescence quickly decayed. However, the decay is not permanent, and over the course of the dark phase, the fluorescence would oscillate back and partially recover in intensity. The changes in detected excitation light shows the opposite oscillatory behavior. During the light-on phases, detected excitation light increases but would partially recover and decrease during the dark

phases. The data indicates possible SL-052 photobleaching during light-on phases and some sort of recovery mechanism during light-off phases. Possible recovery mechanisms include drug redistribution, deaggregation, or reversible photobleaching. The light on decay curves also exhibit exponential behavior, further suggesting photobleaching. This oscillatory behavior in detected excitation and drug fluorescence suggest PDT efficacy may be improved by time-fractionation and motivates further investigation and use of this light delivery method.

The evidence gathered during *in vivo* interstitial photodynamic therapy using this novel switched light delivery and detection system warrants further research using this system in canine or human trials as it is capable of continuous monitoring of treatment dynamics in real-time. Further investigation should include a calibration of the optical metrics with actual drug concentration determined from excised tissue in order to better evaluate dosimetry.

Bibliography

[1] A. Jemal, R. Siegel, E. Ward, Y. Hao, J. Xu, and M. J. Thun, "Cancer statistics, 2009," *CA: A Cancer Journal for Clinicians*, vol. 59, pp. 225–249, 2009.

[2] L. Marrett, P. De, D. Dryer, L. Ellison, E. Grunfeld, H. Logan, M. MacIntyre, L. Mery, H. Morrison, H. K. Weir, L. Xie, and R. Semenciw, *Canadian Cancer Statistics 2009*. Canadian Cancer Society, 2009.

[3] H. I. Scher, S. A. Lieibel, Z. Fuks, C. Cordon-Cardo, and P. T. Scardino, *Cancer: Principles & Practice of Oncology*, 7th ed., V. T. DeVita(Jr.), S. Hellman, and S. A. Rosenberg, Eds. Philadelphia: Lippincott Williams & Wilkins, 2005, vol. 1, ch. 30, sec. 3: Cancer of the Prostate.

[4] A. G. Anastasiadis, M. C. Benson, M. P. Rosenwasser, L. Salomon, H. El-Rashidy, M. A. Ghafar, J. M. McKiernan, M. Burchardt, and R. Shabsigh, "Cavernous nerve graft reconstruction during radical prostatectomy or radical cystectomy: safe and technically feasible," *Prostate Cancer and Prostatic Diseases*, vol. 6, pp. 56–60, 2003.

[5] C. Rados, *Cancer*, C. F. Naff, Ed. The Gale Group, 2008.

[6] G. Onik, "Image-guided prostate cryosurgery: State of the art," *Cancer Control*, vol. 8, pp. 522–531, 2001.

[7] A. Blana, B. Walter, S. Rogenhofer, and W. F. Wieland, "High-intensity focused ultrasound for the treatment of localized prostate cancer: 5-year experience," *Urology*, vol. 63, pp. 297–300, 2004.

[8] M. D. Sherar, M. R. Gertner, C. K. K. Yue, M. E. O'Malley, A. Toi, A. S. Gladman, S. R. H. Davidson, and J. Trachtenberg, "Interstitial microwave thermal therapy for prostate cancer: Method of treatment and results of a phase I/II trial," *Journal of Urology*, vol. 166, pp. 1707–1714, 2001.

[9] S. E. Eggener, P. T. Scardino, P. R. Carroll, M. J. Zelefsky, O. Sartor, H. Hricak, T. M. Wheeler, S. W. Fine, J. Trachtenberg, M. A. Rubin, M. Ohori, K. Kuroiwa, M. Rossignol, and L. Abenhaim, "Focal therapy for localized prostate cancer: A critical appraisal of rationale and modalities," *Journal of Urology*, vol. 178, pp. 2260–2267, 2007.

[10] G. T. Bales, M. J. Willams, M. Sinner, R. A. Thisted, and G. W. Chodak, "Short-term outcomes after cryosurgical ablation of the prostate in men with recurrent prostate carcinoma following radiation therapy," *Urology*, vol. 46, pp. 676–680, 1995.

[11] A. Gelet, J. Y. Chapelon, R. Bouvier, C. Pangaud, and Y. Lasne, "Local control of prostate cancer by transrectal high intensity focused ultrasound therapy: Preliminary results," *Journal of Urology*, vol. 161, pp. 156–162, 1999.

[12] M. R. Cooperberg, D. P. Lubeck, M. V. Meng, S. S. Mehta, and P. R. Carroll, "The changing face of low-risk prostate cancer: Trends in clinical presentation and primary management," *Journal of Clinical Oncology*, vol. 22, pp. 2141–2149, 2004.

[13] P. R. Carroll, "Early stage prostate cancer - Do we have a problem with over-detection, overtreatment or both?" *The Journal of Urology*, vol. 173, pp. 1061–1062, 2005.

[14] A. Bill-Axelson, L. Holmberg, M. Ruutu, M. Häggman, S.-O. Andersson, S. Bratell, A. Spångberg, C. Busch, S. Nordling, H. Garmo, J. Palmgren, H.-O. Adami, B. J. Norlén, and J.-E. Johansson, "Radical prostatectomy versus watchful waiting in early prostate cancer," *New England Journal of Medicine*, vol. 352, pp. 1977–1984, 2005.

[15] F. A. Vicini, E. M. Horwitz, J. Gonzalez, and A. A. Martinez, "Treatment options for localized prostate cancer based on pretreatment serum prostate specific antigen levels," *Journal of Urology*, vol. 158, pp. 319–325, 1997.

[16] T. J. Dougherty, C. J. Gomer, B. W. Henderson, G. Jori, D. Dessel, M. Korbelik, J. Moan, and Q. Peng, "Photodynamic therapy," *Journal of the National Cancer Institute*, vol. 90, pp. 889–905, 1998.

[17] J. Moan and Q. Peng, "An outline of the hundred-year history of PDT," *Anticancer Research*, vol. 23, pp. 3591–3600, 2003.

[18] Z. Huang, Q. Chen, N. Trncic, S. M. LaRue, P.-H. Brun, B. C. Wilson, H. Shapiro, and F. W. Hetzel, "Effects of Pd-bacteriopheophorbide (TOOKAD)-mediated photodynamic therapy on canine prostate pretreated with ionizing radiation," *Radiation Research*, vol. 161, pp. 723–731, 2004.

[19] M. S. McPhee, C. W. Thorndyke, G. Thomas, J. Tulip, J. D. Chapman, and W. H. Lakey, "Interstitial applications of laser irradiation in hemato-

porphyrin derivative-photosensitized Dunning R3327 prostate cancers," *Lasers in Surgery and Medicine*, vol. 4, pp. 93–95, 1984.

[20] S. Gonzalez, M. R. Arnfield, B. E. Meeker, J. Tulip, W. H. Lakey, J. D. Chapman, and M. S. McPhee, "Treatment of Dunning R3327-AT rat prostate tumors with photodynamic therapy in combination with Misonidazole," *Cancer Research*, vol. 46, pp. 2858–2862, 1986.

[21] M. L. Pantelides, C. Whitehurst, J. V. Moore, T. A. King, and N. J. Blacklock, "Photodynamic therapy for localizsed prostatic cancer: light penetration in the human prostate gland," *Journal of Urology*, vol. 143, pp. 398–401, 1990.

[22] Q. Chen, S. D. Shetty, L. Heads, F. Bolin, B. wilson, M. Patterson, L. T. Sirls, D. Schultz, J. C. Cerny, and F. W. Hetzel, "Photodynamic therapy in prostate cancer: Optical dosimetry and response of normal tissue," *Proceedings of SPIE*, vol. 1881, pp. 231–235, 1993.

[23] T. R. Nathan, D. E. Whitelaw, S. C. Chang, W. R. Lees, P. M. Ripley, H. Payne, L. Jones, M. C. Parkinson, M. Emberton, A. R. Gillams, A. R. Mundy, and S. G. Bown, "Photodynamic therapy for prostate cancer recurrence after radiotherapy: A phase I study," *Journal of Urology*, vol. 168, pp. 1427–1432, 2002.

[24] D. Zaak, R. Sroka, M. Hoppner, W. Khoder, O. Reich, S. Tritschler, R. Muschter, R. Knuchel, and A. Hofstetter, "Photodynamic therapy by means of 5-ALA induced PPIX in human prostate cancer - Preliminary results," *Medical Laser Application*, vol. 18, pp. 91–95, 2003.

[25] D. C. H. Stripp, R. Mike, T. C. Zhu, R. Whittington, D. Smith, A. Dimofte, J. Finlay, J. Miles, theresa M. Busch, D. Shin, A. Kachur, Z. A.

Tochner, S. B. Malkowicz, E. Glatstein, and S. M. Hahn, "Phase I trial of motexafin lutetium-mediated interstitial photodynamic therapy in patients with locally recurrent prostate cancer," *Proceedings of SPIE*, vol. 5315, pp. 88–99, 2004.

[26] J. Trachtenberg, A. Bogaards, R. A. Weersink, M. A. Haider, A. Evans, S. A. McCluskey, A. Scherz, M. R. Gertner, C. Yue, S. Appu, A. Aprikian, J. Savard, B. C. Wilson, and M. Elhilali, "Vascular targetted photodynamic therapy with palladium-bacteriopheophorbide photosensitizer for recurrent prostate cancer following definitive radiation therapy: Assessment of safety and treatment response," *Journal of Urology*, vol. 178, pp. 1947–1979, 2007.

[27] D. Kessel, "Photodynamic therapy and neoplastic disease," *Oncology Research*, vol. 4, pp. 219–225, 1992.

[28] M. Wainwright, "Photodynamic therapy: The development of new photosensitizers," *Anti-Cancer Agents in Medicinal Chemistry*, vol. 8, pp. 280–291, 2008.

[29] J. M. Schmitt, "Optical measurement of blood oxygen by implantable telemetry," Ph.D. dissertation, Stanford University, Stanford, USA, 1986.

[30] M. K. Moaveni, "A multiple scattering field theory applied to whole blood," Ph.D. dissertation, University of Washington, Seattle, USA, 1970.

[31] S. Takatani and M. D. Graham, "Theoretical analysis of diffuse reflectance from a two-layer tissue model," *IEEE Transactions on Biomedical Engineering*, vol. BME-26, pp. 656–664, 1979.

[32] S. Xu, X. Zhang, S. Chen, M. Zhang, and T. Shen, "The fluorescence properties of Hypocrellin B and its amino-substituted derivative: Pho-

toinduced intramolecular proton transfer and photoinduced intramolecular electron transfer," *Photochemistry and Photobiology*, vol. 80, pp. 112–114, 2004.

[33] W. M. Star, *Optical-Thermal Response of Laser-Irradiated Tissue*. Plenum Press, 1995, ch. 6: Diffusion Theory of Light Transport, pp. 131–206.

[34] M. R. Arnfield, J. Tulip, M. Chetner, and M. McPhee, "Optical dosimetry for interstitial photodynamic therapy," *Medical Physics*, vol. 16, pp. 602–608, 1989.

[35] I. Driver, C. P. Lowdell, and D. V. Ash, "In vivo measurement of the optical coefficients of human tumors at 632 nm," *Physics in Medicine and Biology*, vol. 36, pp. 805–813, 1991.

[36] L. Lilge, M. Olivo, S. Schatz, and B. C. Wilson, "Determination of the photodynamic threshold for normal rabbit brain and for intracranially implanted VX2 tumors," *Proceedings of SPIE*, vol. 1882, pp. 60–72, 1993.

[37] L. Lilge and B. C. Wilson, "The accuracy of interstitial measurements of absolute light fluence rate in the determination of tissue optical properties," *Proceedings of SPIE*, vol. 1882, pp. 291–304, 1993.

[38] B. C. Wilson, *Optical-Thermal Response of Laser-Irradiated Tissue*. Plenum Press, 1995, ch. 8: Measurement of Tissue Optical Properties: Methods and Theories, pp. 233–304.

[39] D. J. Dickey, "Light dosimetry for interstitial photodynamic therapy: Application to the treatment of prostatic carcinoma," Ph.D. dissertation, University of Alberta, Edmonton, Canada, 2004.

[40] R. Graaff and B. J. Hoenders, "Diffusion theory for light propagation in biological tissue: limitations and adaptations," *Proceedings of SPIE*, vol. 5771, pp. 28–41, 2004.

[41] S. L. Jacques and L. Wang, *Optical-Thermal Response of Laser-Irradiated Tissue*. Plenum Press, 1995, ch. 4: Monte Carlo Modeling of Light Transport in Tissues, pp. 73–100.

[42] W. H. Nau, R. J. Roselli, and D. F. Milam, "Measurement of thermal effects on the optical properties of prostate tissue at wavelengths of 1,064 and 633 nm," *Lasers in Surgery and Medicine*, vol. 24, pp. 38–47, 1999.

[43] D. J. Dickey, R. B. Moore, D. C. Rayner, and J. Tulip, "Light dosimetry using the P3 approximation," *Physics in Medicine and Biology*, vol. 46, pp. 2359–2370, 2001.

[44] I. Driver, J. W. Feather, P. R. king, and J. B. Dawson, "The optical properties of aqueous suspensions of intralipd a fat emulsion," *Physics in Medicine and Biology*, vol. 34, pp. 1927–1930, 1989.

[45] H. J. van Staveren, C. J. M. Moes, J. van Marle, S. A. Prahl, and M. J. C. van Gemert, "Light scattering in intralipid-10% in the wavelength range of 400-1100 nm," *Applied Optics*, vol. 30, pp. 4507–4514, 1991.

[46] S. T. Flock, S. L. Jacques, B. C. Wilson, W. M. Star, and M. J. C. van Gemert, "Optical properties of intralipid: A phantom medium for light propagation studies," *Lasers in Surgery and Medicine*, vol. 12, pp. 510–519, 1992.

[47] T. Xu, C. Zhang, X. Wang, L. shun Zhang, and J. Tian, "Measurement and analysis of light distribution in intralipid-10% at 650 nm," *Applied Optics*, vol. 42, pp. 5777–5784, 2003.

[48] S. Prahl, "Optical absorption of methylene blue," Oregon Medical Laser Center, Portland, USA, Tech. Rep., 1998.

[49] D. J. Dickey, Z. Xiao, K. Partridge, R. B. Moore, and J. Tulip, "Fractionated PDT light delivery system based upon fibre optic switching technology," *Proceedings of SPIE*, vol. 5142, pp. 215–222, 2003.

[50] Z. Xiao, S. Hall, D. Dickey, J. Tulip, and R. B. Moore, "Fractionated versus standard continuous light delivery in interstitial photodynamic therapy of Dunning prostate carcinomas," *Clinical Cancer Research*, vol. 13, pp. 7496–7505, 2007.

[51] R. A. Weersink, A. Bogaards, M. Gertner, S. R. Davidson, K. Zhang, G. Netchev, J. Trachtenberg, and B. C. Wilson, "Techniques for delivery and monitoring of TOOKAD (WST09)-mediated photodynamic therapy of the prostate: Clinical experiences and practicalities," *Photochemistry and Photobiology*, vol. 79, pp. 211–222, 2005.

[52] A. Johansson, T. Johansson, M. S. Thompson, N. Bendsoe, K. Savanberg, and S. S. S. Andersson-Engels, "In vivo measurment of parameters of dosimetric importance during interstitial photodynamic therapy of thick skin tumors," *Journal of Biomedical Optics*, vol. 11, pp. 034 029–1–10, 2006.

[53] T. C. Zhu, S. M. Hahn, A. S. Kapatkin, A. Dimofte, C. E. Rodriguez, T. G. vulcan, E. Glatstein, and R. A. Hsi, "In vivo optical properties of normal canine prostate at 732 nm using motexafin lutetium-mediated photodynamic therapy," *Photochemistry and Photobiology*, vol. 77, pp. 81–88, 2003.

[54] K. Du, R. Mick, T. Busch, T. Zhu, J. Finlay, G. Yu, A. Yodh, S. Malkowicz, D. Smith, R. Whittington, D. Stripp, and S. Hahn, "Preliminary results of interstitial motexafin leutetium-mediated PDT for prostate cancer," *Lasers in Surgery and Medicine*, vol. 38, pp. 427–434, 2006.

[55] J. C. Finlay, T. C. Zhu, A. Dimofte, D. Stripp, S. B. Malkowicz, T. M. Busch, and S. M. Hahn, "Interstitial fluorescence spectroscopy in the human prostate during motexafin lutetium-mediated photodynamic therapy," *Photochemistry and Photobiology*, vol. 82, pp. 1270–1278, 2006.

[56] C. M. Moore, T. R. Nathan, W. R. Lees, C. A. Mosse, A. Freeman, M. Emberton, and S. G. Bown, "Photodynamic therapy using meso tetra hydroxy phenyl chlorin (mTHPC) in early prostate cancer," *Lasers in Surgery and Medicine*, vol. 38, pp. 356–363, 2006.

[57] Q. Chen, B. C. Wilson, S. D. Shetty, M. S. Patterson, J. C. Cerny, and F. W. Hetzel, "Changes in in vivo optical properties and light distribution in normal canine prostate during photodynamic therapy," *Radiation Research*, vol. 147, pp. 86–91, 1997.

[58] L. Lilge, N. Pomerleau-Dalcourt, A. Douplik, S. H. Selman, R. W. Keck, M. Szkudlarek, M. Pestka, and J. Jankun, "Transperineal in vivo fluence-rate dosimetry in the canine prostate during SnET2-mediated PDT," *Physics in Medicine and Biology*, vol. 49, pp. 3209–3225, 2004.

[59] L. M. Wood, D. A. Bellnier, A. R. Oseroff, and W. R. Potter, "A beam-splitting device for use with fiber-coupled laser light sources for photodynamic therapy," *Photochemistry and Photobiology*, vol. 76, pp. 683–685, 2002.

[60] Vernier Software & Technology, "Physics instructors record emission spectra of common light sources," *The Caliper*, vol. 23, p. 2, 2006.

[61] Y. Ralchenko, A. E. Kramida, J. Reader, E. B. Saloman, J. E. Sansonetti, J. J. Curry, D. E. Kelleher, J. R. Fuhr, L. Podobedova, W. L. Wiese, K. Olsen, G. R. Dalton, R. Dragoset, F. C. Jou, W. C. Martin, P. J. Mohr, A. Musgrove, C. J. Sansonetti, and G. Wiersma. (2008, April) NIST atomic spectra database (ver. 3.1.5). Web. National Institute of Standards and Technology, Gaithersburg, USA. [Online]. Available: http://physics.nist.gov/asd3

[62] T. Jüstel, "7. leuchtstoffe: Lichttechnik und leuchtstoffe," Fachhochschule Münster University of Applied Sciences, Steinfurt, Germany, Tech. Rep., 2008.

[63] T.-L. Phan, manh Huong Phan, N. Vu, T.-K. Anh, and S.-C. Yu, "Luminescent properties of Eu-doped Y2O3 nanophosphors," *Physica Status Solidi (a)*, vol. 201, pp. 2170–2174, 2004.

[64] A. M. Srivastava and C. R. Ronda, "Phosphors," *The Electrochemical Society Interface*, vol. Summer, pp. 48–51, 2003.

[65] L. M. Vesselov, W. Whittington, and L. Lilge, "Performance evaluation of cylindrical fiber optic light diffusers for biomedical applications," *Lasers in Surgery and Medicine*, vol. 34, pp. 348–351, 2004.

[66] L. Lilge, L. Vesselov, and W. Whittington, "Thin cylindrical diffusers in multimode Ge-doped silica fibers," *Lasers in Surgery and Medicine*, vol. 36, pp. 245–251, 2005.

[67] W. Liu, D. J. Dickey, Z. Xiao, R. B. Moore, and J. Tulip, "Dosimetric considerations of interstitial photodynamic therapy of the canine prostate

mediated by intra-arterially administered hypocrellin derivative," *Proceedings of SPIE*, vol. 6845, p. 684519, 2008.

[68] D. J. Dickey, W. Liu, S. Naicker, T. Woo, R. B. Moore, and J. Tulip, "Using fluorescence to augment the efficacy of photodynamic therapy," *Proceedings of SPIE*, vol. 6343, p. 634305, 2006.

[69] T. Woo, Z. Xiao, K. Brown, D. Dickey, and R. B. Moore, "Interstitial PDT for prostate cancer," Quest PharmaTech Incorporated, Edmonton, Canada, Tech. Rep., 2008.

[70] K. Brown, Z. Xiao, D. Dickey, R. B. Moore, and T. Woo, "SL-052 on Dunning R3327-AT internal report," Quest PharmaTech Incorporated, Edmonton, Canada, Tech. Rep., 2008.

[71] S. H. Selman, D. Albrecht, R. W. Keck, P. Brennan, and S. Kondo, "Studies of tin ethyl ethiopurpurin photodynamic therapy of the canine prostate," *Journal of Urology*, vol. 165, pp. 1795–1801, 2001.

[72] M. L. Pantelides, J. V. Moore, E. Forbes, T. G. Truscott, and N. J. Blacklock, "The uptake of porphyrin and zinc-metalloporphyrin by the primate prostate," *Photochemistry and Photobiology*, vol. 57, pp. 838–841, 1993.

[73] T. Momma, M. R. hamblin, H. C. Wu, and T. Hasan, "Photodynamic therapy of orthotopic prostate cancer with benzoporphyrin derivative: Local control and distant metastasis," *Cancer Research*, vol. 58, pp. 5425–5431, 1998.

[74] M. L. Pantelides, J. V. Moore, and N. J. Blacklock, "A comparison of serum kinetics and tissue distribution of photofrin II following intravenous

and intraperitoneal injection in the mouse," *Photochemistry and Photobiology*, vol. 49, pp. 67–70, 1989.

[75] R. B. Moore, Z. Xiao, R. J. Owen, R. Ashforth, D. Dickey, C. Helps, and J. Tulip, "Photodynamic therapy of the canine prostate: Intra-arterial drug delivery," *Cardiovascular and Interventional Radiology*, vol. 31, pp. 164–176, 2008.

[76] M. B. Ericson, C. Sandberg, B. Stenquist, F. Gudmundson, M. Karlsson, A.-M. Ros, A. Rosén, O. Larkö, A.-M. Wennberg, and I. Rosdahl, "Photodynamic therapy of actinic keratosis at varying fluence rates: assessment of photobleaching, pain and primary clinical outcome," *British Journal of Dermatology*, vol. 151, pp. 1204–1212, 2004.